INTERACTIONS BETWEEN TROPICAL CONVECTION AND THE ENVIRONMENT: A VIEW ACROSS SCALES

A Dissertation

by

FIAZ AHMED RAFI AHMED

Submitted to the Office of Graduate and Professional Studies of
Texas A&M University
in partial fulfillment of the requirement for the degree of

DOCTOR OF PHILOSOPHY

Chair of Committee,	Courtney Schumacher
Committee Members,	R. Saravanan
	John Nielsen-Gammon
	Anne Raymond
Head of Department,	Ping Yang

December 2016

Major Subject: Atmospheric Sciences

ABSTRACT

The interaction between moist convection and the environment that engenders it is a problem that spans multiple scales. In this study, the problem is approached using a suite of observational and modeling tools. The first approach was the development of an algorithm to estimate latent heating profiles from radar observations using a high-resolution version of the Weather Research and Forecasting Model (WRF). A lookup table was constructed from WRF output to statistically quantify the relationship between latent heating and three characteristics of radar-observed storms: size, mean height and mean intensity. A tight link between organization (characterized by the size of the system) and the intensity (as measured by latent heat release) was found. The algorithm was validated against field campaign observations and shows skill in replicating the short-term (less than daily) variability associated with tropical synoptic systems. The second approach was to analyze the relationship between convection and the environment via moisture modulation using the Tropical Rain Measuring Mission satellite and reanalysis data, with focus on the tropical precipitation-water vapor relationship (P-*r* curve) which is a power-law relationship, which at the convective time and space scales is characterized by a sharp increase in precipitation beyond a critical value of moisture (the pickup threshold). The convective and stratiform components of the P-*r* relationship were studied separately and it was found that the pickup in tropical precipitation mainly originates from a rapid pickup in the areal extent of stratiform precipitation. A survey of the P-*r* curve across the tropical world–both land and ocean–shows that the pickup threshold is much lower over tropical land than over

the ocean and that convective precipitation picks up prior to stratiform precipitation. Finally the implications of a precipitation-moisture relationship were explored for prominent forms of organized convection in the tropics, i.e, tropical waves and the Madden-Julian Oscillation. It was found that the different sources of column moisture (horizontal transport and convection) were influential in environments with different moisture levels. These relationships are also dependent on the time and space scale of analysis.

ACKNOWLEDGMENTS

I would like to thank my advisor and committee chair Dr. Courtney Schumacher for her guidance that has greatly impacted this work. Her unwavering optimism and infectious passion has also positively influenced my desire to pursue science for a living. I would like to thank my other committee members: Dr. Saravanan for his wisdom and counsel at crucial junctures during the course of my dissertation work, Dr.Nielsen-Gammon for his insights and comments on this work and Dr. Anne Raymond for her support and appreciation. I would also like to thank past and present overlapping members of the A-Team for providing a fun and resourceful work environment. I would also like thank my friends outside the department for helping me create cherished memories at Texas A&M. Special thanks to members of my family and Arti Munshi for steady support and understanding that has helped me see through these years. I would also like to thank Dr. Samson Hagos and Dr. Zhe Feng for inviting me to spend a fruitful summer working at the Pacific Northwest National Laboratory. I would finally like to thank all the other members of the faculty and students for many insightful conversations that have shaped my understanding of the multifarious phenomena that abound in nature and the extensive toolkit that exists to view them.

This research was supported by NSF grant AGS-1062217, JAMSTEC and the NASA grant NNX13AG90G. The data from the DYNAMO field campaign used in this study is available online at the EOL data catalog: http://data.eol.ucar.edu/master_list/?project=DYNAMO and also at the ARM archive:

http://www.archive.arm.gov/discovery/. MERRA data were generated by the NASA Global Modeling and Assimilation Office (GMAO) and disseminated by the Goddard Earth Sciences (GES) Data and Information Services Center (DISC). ERA-Interim data used in this was provided courtesy European Center for Medium-range Weather Forecasts (ECMWF) The TRMM PR data used in this study were processed by the TRMM Science Data and Information System (TSDIS) and the TRMM Office; they are distributed by the Goddard Earth Sciences Data and Information Services Center (GES DISC). The filtered TRMM 3B42 data used in this study was obtain from Carl Schreck at NOAA's National Centers for Environmental Information.

TABLE OF CONTENTS

LIST OF FIGURES

LIST OF TABLES

CHAPTER I

INTRODUCTION

The tropical regions on earth experience a weak Coriolis force because the planetary axis of rotation is nearly perpendicular to the local vertical in these regions. A consequence of this reduced effect of rotation is that horizontal gradients of pressure and temperature in the atmosphere are weak in areas not experiencing condensation (Charney, 1963). Condensational heating is balanced by cooling in intense areas of vertical motion, which then influence the non-precipitating regions via slow subsidence which is spread by gravity waves that act to maintain the weak temperature gradient. Therefore, in this tropical world, prediction and understanding of weather and climate chiefly arises from an understanding of the interactions between the regions of condensation—moist convection—and the surrounding non precipitating environment that engenders convection and interacts with it.

Our progress in understanding convection-environment interactions, however, has been limited, because of the multiplicity of scales involved. Another stumbling block is the fact that convection at the smallest scales is essentially a turbulent process that is hard to understand and model mathematically. The added effect of phase change—which drives most of the tropical dynamics—renders the problem even more intractable by changing the stability properties and mass and energy budgets of the atmosphere in myriad, intricate ways (Emanuel et al., 1994; Emanuel, 1997) The end point of all this seemingly insurmountable difficulty is that atmospheric scientists always deal with the statistical proper-

ties of convection—or an ensemble (Arakawa and Schubert, 1974)—on different time and space scales.

The problem of convection-environmental interactions in this statistical framework therefore reduces to the following two questions:

1. How does the non-convecting environment modulate (i.e.,initiate, sustain and kill) an ensemble of convecting elements of varying size and vigor?
2. How does the ensemble of convection in turn affect the average properties of the environment?

This statistical view of convection has driven our advances in the understanding of cloud-environment interactions and is best exemplified by its use in convective parameterization schemes. Even though these schemes have made helped to make enormous strides in the numerical simulation of weather and climate, they still remain the Achilles heel of modern day GCMs (Randall et al., 2003; Hung et al., 2013), particularly in simulating intraseasonal tropical variability (Hung et al., 2013; Jiang et al., 2015) and could possibly lie at the root of several persistent biases in GCMs (Richter et al., 2015). We can tackle the problem of imperfections in cumulus parameterization by resolving our way out of it, i.e., by increasing model spatial resolution to ensure that the cloud-scale processes are explicitly captured by equations. Moving to high resolution, however, is computationally expensive and can introduce a host of unanticipated problems (Bryan and Morrison, 2012). The statistical view of the cumulus ensemble therefore still has relevance, particularly for long running climate simulations, even in the age of higher resolution models.

One the many fascinating aspects of moist convection is its propensity to organize or aggregate across spatial scales. This property of tropical convection is being increasingly appreciated, particularly in the light of recent results from cloud-resolving studies that display the spatial aggregation of convective elements when run under idealized radiative-convective equilibrium conditions (Muller and Held, 2012), though long recognized in the world of observations (Mapes, 1993; Chen et al., 1996).One focus of this study will be on convective organization and particularly, its relationship to the environment.

The most obvious impact of the cumulus ensemble on the environment is through effects on the heat budget. Convection releases latent heat, which has circulation affects(Gill, 1980; Hartmann et al., 1984; Schumacher et al., 2004), impacts the atmospheric radiative budget through longwave and shortwave interactions (Ramanathan et al., 1989; Rossow and Lacis, 1990) and allows vertical turbulent transport of heat (Schlesinger, 1994). Since the ensemble area is larger than the individual cumulus cloud, the effects of eddy transport and radiation pale in comparison to the magnitude of latent heat release, which is the most important term in the cumulus ensemble heat budget. Quantifying latent heat release, however, is not possible by means of straightforward measurement, because the heat release is balanced by vertical motion accompanied by adiabatic cooling and does not manifest itself through temperature changes. Other means of retrieving latent heat are therefore adopted and various algorithms—usually tuned for specific observing instruments—exist for this purpose. The first part of this dissertation, as described in Chapter II, is the construction of an algorithm to infer latent heating from radar reflectivity measurements. The novel

feature of this algorithm is the utilization of the organization of convection in the retrieval process.

The second part of this dissertation, outlined in Chapter III, describes the modulation of the convective ensemble by the ambient moisture field. This part of the study deals with how changes in moisture can co-occur with changes in intensity and the occurrence frequency of convecting elements within the ensemble. These simple relationships are gleaned by disassembling the tropical precipitation-water vapor curve or the P-*r* curve (Bretherton et al., 2004) with respect to the different sub-systems of tropical precipitation—convective, stratiform and shallow clouds—a mode of classification that distinguishes the broadly different types of cloud microphysical and dynamical processes using information from observations (Houghton, 1968; Houze, 1997). This chapter also presents a survey of the geographical distribution of the environmental control on convection, particularly distinguishing between land and oceans in tropics and highlighting prominent outlier regions.

Using insights gained from how the environmental moisture controls characteristics of tropical convection, Chapter IV analyzes the Madden Julian Oscillation (MJO) (Madden and Julian, 1971), particularly in the light of theories that hypothesize the MJO to be an unstable mode in the column moisture content. In this chapter, the different influences on the column moisture content that can support the different stages of the MJO are studied using reanalysis data as well as from a field campaign in the central Indian Ocean. These results are summarized in Chapter IV of this dissertation. Finally, Chapter V contains a summary of all the presented results as well as possible avenues for future work.

CHAPTER II

A RETRIEVAL OF TROPICAL LATENT HEATING USING THE 3D STRUCTURE OF PRECIPITATION FEATURES*

II.1 Background

Latent heat released during moist convective processes can trigger a slew of local and large-scale phenomena. Local changes such as buoyancy perturbations manifest themselves as gravity waves that can engender further convection leading to mesoscale organization (Mapes, 1993; Lac et al., 2002). The condensational heating from organized convective systems can determine the seasonal and intraseasonal sources of tropical variability, as demonstrated by idealized modeling studies (Gill, 1980; Hartmann et al., 1984). Major weather systems across the tropics and the extratropics are driven by latent heat: the East Asian summer monsoon (Jin et al., 2013), the African monsoon, mid-latitude cyclones (Hagos and Zhang, 2010; Stoelinga, 1996), and tropical waves and the Madden-Julian oscillation (Chen and Yen, 1991; Li et al., 2009; Lappen and Schumacher, 2012).

The vertical profile of latent heating is a representation of the convecting atmosphere and a useful proxy for large-scale vertical velocities in the tropics, with the magnitude of heating being dominated by condensational processes (Houze, 1982, 1989). The influences of large-scale synoptic and planetary wave features and local forcing such as the diurnal

*Reprinted with permission from "A Retrieval of Tropical Latent Heating Using the 3D Structure of Precipitation Features" by Ahmed, Fiaz, C. Schumacher, S. Hagos and Z. Feng, 2016 in *Journal of Applied Meteorology and Climatology*, **55**, 1965–1982. Copyright [2016] by American Meteorological Society.

cycle can also manifest themselves in the local heating profiles (Schumacher et al., 2007). Accurate retrieval of latent heating is therefore useful to study convection and its associated circulations. Latent heating associated with convection manifests itself as dynamical perturbations rather than temperature changes (Mapes and Houze, 1995), making a direct measurement of latent heating difficult. Reanalysis data, while extensive in coverage, rely heavily on the parent model when observations are scarce and are mainly derived from parameterized cumulus and radiative processes. As a result, the vertical profiles of heating from reanalyses do not always agree with sounding budgets (Hagos, 2010; Ling and Zhang, 2011) or Tropical Rainfall Measuring Mission (TRMM) satellite retrievals (Chan and Nigam, 2009; Jiang et al., 2011). Therefore, reliable estimates of latent heating must be inferred from other measurable quantities like radar reflectivity or rainfall. Most existing latent heating retrieval methods utilize certain unique properties of tropical convection.

Broadly speaking, tropical precipitation can be reduced into two mutually exclusive categories: convective and stratiform, with each category possessing a canonical heating profile (Houze, 1997). Stratiform rain processes warm the troposphere at upper levels and cool at lower levels. Deep convective rain processes warm the entire troposphere with a heating peak at midlevels, while shallower convection has a heating peak in the lower troposphere (Schumacher et al., 2004). The bulk of the variance in the vertical structure of tropical latent heating can be explained by a composite of bottom- and middle-heavy convective-like profiles and top-heavy stratiform-like profiles (Zhang and Hagos, 2009; Hagos, 2010). Thus, several latent heating retrieval algorithms utilize the knowledge of

convective and stratiform rain separation and the output of heating from cloud models (Tao and Simpson, 1989; Tao et al., 1993b). Multiple latent heating retrieval algorithms exist for products from the TRMM satellite (see review in Tao et al. (2006)). For example, Precipitation Radar (PR) observations are used by the convective-stratiform heating (CSH) algorithm (Tao et al., 1993a, 2010), which uses information about surface precipitation rates, the amount of stratiform versus convective rain, and whether the cloud systems are over ocean or land. A lookup table (LUT) generated by a cloud-resolving model (CRM) then provides the convective and stratiform heating profiles. TRMM Microwave Imager (TMI) observations are utilized by the hydrometeor heating (HH; Yang and Smith (1999)) and trained radiometer (Olson et al., 1999, 2006; Grecu and Olson, 2006) algorithms, which also use CRM-derived LUTs to retrieve vertical heating profiles based on microwave radiative characteristics. The TRMM approach that is most similar to the technique described in this study is the spectral latent heating (SLH) algorithm (Shige et al., 2004), in which information about surface rain, the convective-stratiform separation, the melting layer, and precipitation-top height from a CRM are used to generate a LUT of latent heating profiles and applied to the PR observations. Schumacher et al. (2004) created a simpler LUT meant to be applied to satellite or ground-based radar. Their method uses convective-stratiform rain information (including from shallow convection) and assumes an idealized heating profile for each rain type. These three idealized profiles were composited from long-term observational studies of vertical motion and diabatic heating in the tropics and are not based on CRM output. Convective and stratiform rain can almost completely determine

the large-scale dynamical character of the tropical atmosphere (Mapes and Houze, 1995). Therefore, this method works well in estimating the mean latent heating profile averaged over space and time scales representative of mesoscale storm processes (Schumacher et al., 2007).

Because all of the above radar-based latent heating retrievals are dependent on surface rainfall, estimates of which suffer from a number of potential errors (Austin, 1987; Houze et al., 2004), and latent heating associated with convective systems is "felt" by the atmosphere much more broadly than in a precipitating column, a latent heating algorithm that circumvents pixel-based radar rainfall retrievals is introduced. Rather, the approach described here is to estimate latent heating from radar echo area coverage rather than rainfall, where contiguous pixels are grouped into clusters. This procedure increases the representativeness and reduces the error in the sample by reducing the variations in individual pixels. The area paradigm captures the spectrum of convective organization from individual cumulus clouds to mesoscale convective systems and has the potential to be applied across a wide range of regions and platforms.

II.2 Observations and model configuration

The data for this study come from observations and a 20-day-long regional model simulation from the Dynamics of the Madden-Julian Oscillation (DYNAMO), the Cooperative Indian Ocean Experiment on Intraseasonal Variability in the Year 2011 (CINDY2011), and the Atmospheric Radiation Measurement (ARM) MJO Investiga-

tion Experiment (AMIE) field campaigns (DYNAMO/CINDY2011/AMIE; hereinafter referred to as DYNAMO), which took place over the equatorial Indian Ocean from October 2011 to March 2012 to better understand and forecast the initiation of the MJO (Yoneyama et al., 2013). The field deployment consisted of numerous observational platforms, although the focus of this study will be on measurements made with the National Center for Atmospheric Research S-PolKa radar, a dual-frequency (S and Ka band), dual-polarimetric Doppler radar that was located at Addu Atoll, Maldives (Figure 2.1). Profiles of the apparent heat source Q1 retrieved from the DYNAMO sounding and surface rainfall data on Addu Atoll, supplemented by reanalysis information surrounding the atoll are also utilized. This retrieval is based on the variational analysis approach of Zhang and Lin (1997). Variational analysis minimizes the sampling errors in the sounding data (Mapes et al., 2003) by constraining the sounding observations to conserve column-integrated mass, momentum, energy, and moisture (Zhang et al., 2001). The Q1 used in this study was calculated as an average over a 300-km domain (see the circle in Fig. 1) centered on the DOE ARM mobile facility on Addu Atoll and was constrained by the S-PolKa near-surface rainfall estimates.

The equation for Q1 at any vertical level in the troposphere is from (Yanai et al., 1973):

$$Q_1 \equiv \frac{\partial \bar{s}}{\partial t} + \nabla . \bar{s}\mathbf{V} + \frac{\partial \bar{s}\bar{\omega}}{\partial p} = Q_R + L(c-e) - \frac{\partial \overline{s'\omega'}}{\partial p} \tag{II.1}$$

where s is the dry static energy of the atmosphere, $\mathbf{V}$ is the horizontal wind velocity, Q_R is the net column radiative heating of the atmosphere, $L(c-e)$ is the net column latent heating associated with condensational and evaporative processes, and $\frac{\partial \overline{s'\omega'}}{\partial p}$ is the verti-

cal eddy transport of s. The overbar stands for horizontal area averaging, and the primes indicate fluctuations about the mean. Equation (2) can be rearranged as:

$$Q_1 - Q_R = L(c-e) - \frac{\partial \overline{s'\omega'}}{\partial p} \tag{II.2}$$

where $Q_1 - Q_R$ equals the sum of the latent heat released and the vertical eddy transport of sensible heat. In the tropics, the net effect of radiation is to cool the troposphere by 1-2 K/day. (see Fig. 1 in Mapes (2000)). The vertical eddy transport of sensible heat is largely positive in mesoscale convective systems (Houze, 1982), though it can be negligible in mesoscale convective systems with widespread anvil (Johnson and Young, 1983; Yanai and Johnson, 1993). The Q_R and $\frac{\partial \overline{s'\omega'}}{\partial p}$ terms will therefore offset each other and the latent heating, $L(c-e)$, is thus likely to be closer to Q_1 than $Q_1 - Q_R$.

The Advanced Research Weather Research and Forecasting (WRF) Model, version 3.4.1, was used to generate the latent heating LUT. The utility of this model has been described and demonstrated in Hagos and Leung (2011) for high-resolution regional modeling of the MJO. This version of the model has a forward radar simulator that can simulate S-band (10-cm wave-length) reflectivity based on input hydrometeor size distribution following (Smith, 1984), which is generated by the model microphysics scheme. The radar simulator used in this model only utilizes precipitating hydrometeors (rain, graupel, and snow) in estimating the reflectivity, thus neglecting the non-precipitating cloud ice and cloud liquid water (Hagos et al., 2014a). The microphysics parameterization is the Thompson scheme (Thompson et al., 2008) but with modified raindrop breakup parame-

ters to improve model-simulated radar reflectivity from precipitating clouds and cold pool statistics. The results pertaining to the use of different microphysics schemes and their effect on the WRF precipitating cloud statistics are detailed in Hagos et al. (2014a). Though the model has biases in estimating the rain amount, the biases do not necessarily hinder the construction of the algorithm because the relationship between the model-simulated reflectivity and latent heating profiles is being exploited. The model was run with 500-m horizontal resolution and 40 vertical levels over a 4.5° X 9° domain covering a large area of the near-equatorial central Indian Ocean (Figure 2.1). Sensitivity tests were also performed with a 2-km horizontal resolution run. The simulation period was from 2 to 20 November 2011, and the model has been shown to adequately capture cloud statistics and cold pools associated with precipitation and to allow comparison with the observations obtained from DYNAMO (Hagos et al., 2014a; Feng et al., 2015). The boundaries of the model domain and the sea surface temperature are forced with the ERA-Interim 6-hourly reanalysis (Dee et al., 2011) produced by the European Center for Medium-Range Weather Forecasts (ECMWF). The other parameterization schemes are listed in Table 2.1.

II.3 Algorithm description

Reflectivity data from the WRF radar simulator were used to partition every raining pixel (i.e., reflectivity > 5 dBZ at 2.5 km) in the model into convective and stratiform categories using the method of Steiner et al. (1995). The Steiner et al. algorithm differentiates individual convective and stratiform pixels based on the absolute magnitude and peaked-

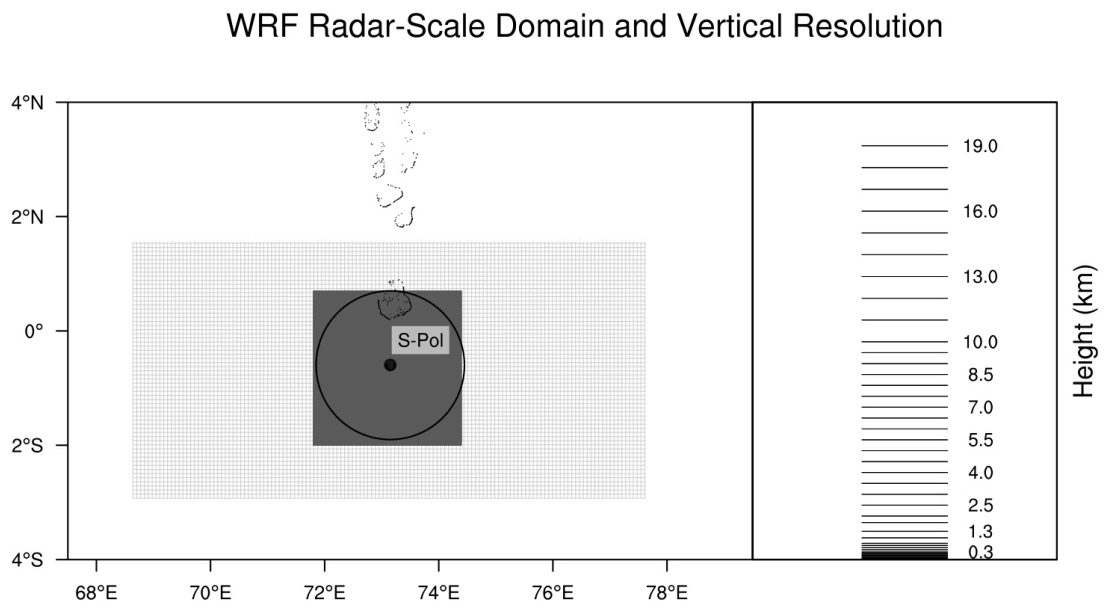

Figure 2.1: (left) The Maldives in the Indian Ocean with the WRF domain (outer gray box) and the S-PolKa radar-scale domain (inner gray box), and (right) the WRF vertical resolution. S-PolKa was located on Addu Atoll, the farthest south of the Maldives. The black circle represents the 150-km radius from S-PolKa.

ness of the horizontal reflectivity field at a single height (2.5 km in this case). The raining pixels in the model were then grouped into clusters, where a cluster is defined as an area of contiguous reflectivity of the same category (convective or stratiform; Figure 2.2).

It is acknowledged that the model runs and the grouping of the model reflectivity pixels into clusters were obtained from Samson Hagos and Zhe Feng at the Pacific Northwest National Laboratory (PNNL). All the following analysis, including the algorithm construction, is a product of the author's effort. However, prior to the description of the algorithm LUTs, the sensitivity of the model output to horizontal resolution is first explored.

Bryan and Morrison (2012) pointed out the impact of higher resolution on the

Table 2.1: Model setup

Simulation period	1–20 Nov 2011
Horizontal resolution	500 m
Microphysics schemes	Modified Thompson (increased raindrop breakup efficiency; Hagos et al. (2014a)
Lateral and surface forcing	ERA-Interim 6-hourly analysis
PBL scheme	Mellor—Yamada—Janjić (Janjić, 2002)
Surface scheme	Monin—Obukhov—Janjić (Janjić, 2002)
Longwave radiation scheme	Rapid Radiative Transfer Model for GCMs (RRTMG;Iacono et al. (2000))
Shortwave radiation scheme	Dudhia (1989)

strength of the convective cells in their WRF squall-line simulation. They showed that for an increase in horizontal resolution, the convective updrafts and cell area decreased in size accompanied by greater occurrence of cloud water evaporation in the downdrafts and cloud edges. The same phenomenon was observed in this study's model runs, which is illustrated in Figure 2.3. The convective cluster in the 500-m run has a smaller areal coverage of strong convection than the 2-km convective cluster. This means that 500-m convective cluster possesses weaker area-averaged latent heating than the 2-km cluster. This mismatch influenced the area-based latent heating retrieval when the algorithm was applied to a radar grid that had a 2-km horizontal resolution by producing weaker convective heating. To rectify this issue in the 500-m run, only convective pixels in the cluster whose 2.5-km reflectivity value was greater than 50% of the maximum reflectivity were included in the cluster. This modification would depend on the resolution of the radar grid

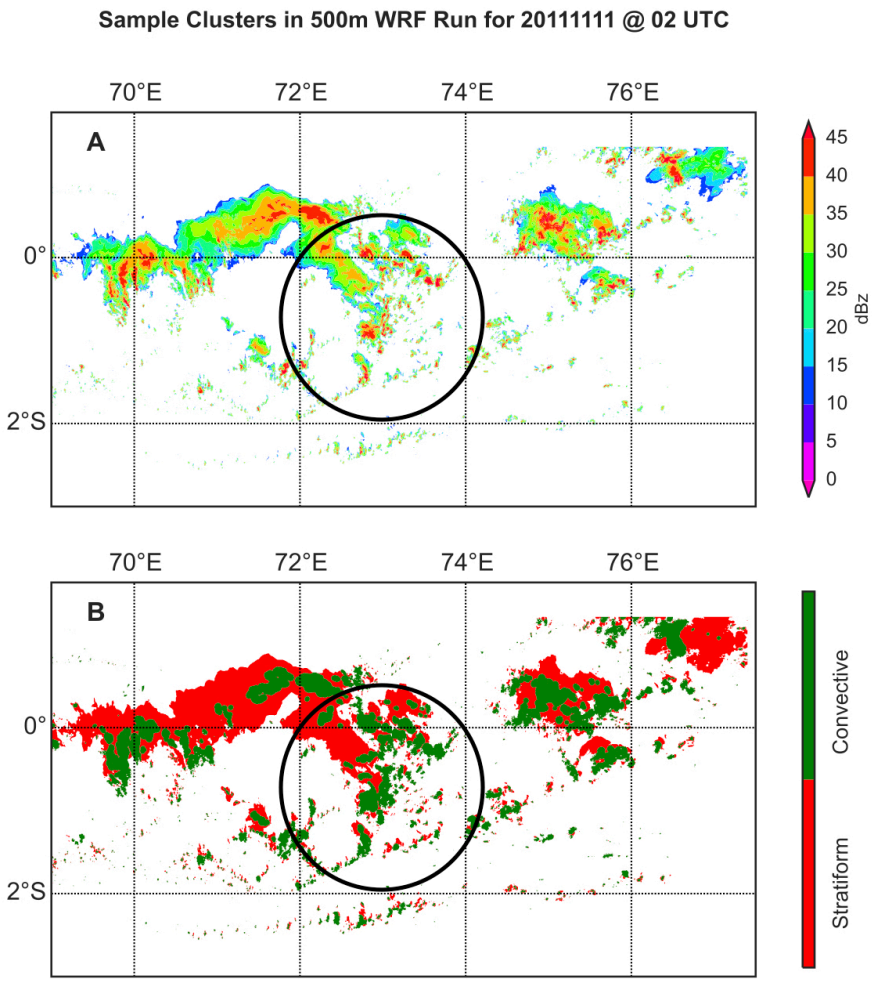

Figure 2.2: Example grouping of convective and stratiform reflectivity regions and clusters in the WRF domain for 0200 UTC 11 Nov 2011. The approximate range of the S-Pol surveillance scan is indicated by the circle to show the scale of the clusters.

to which the retrieval algorithm is being applied. Since radar data are commonly produced on a 2-km Cartesian grid, this particular version of the algorithm has been modified as described above, for use on a 2-km radar grid.

Figure 2.4 shows a 5-day time series of the area- averaged heating profile derived directly from the model physics for the convective and stratiform rain clusters in the 500-m

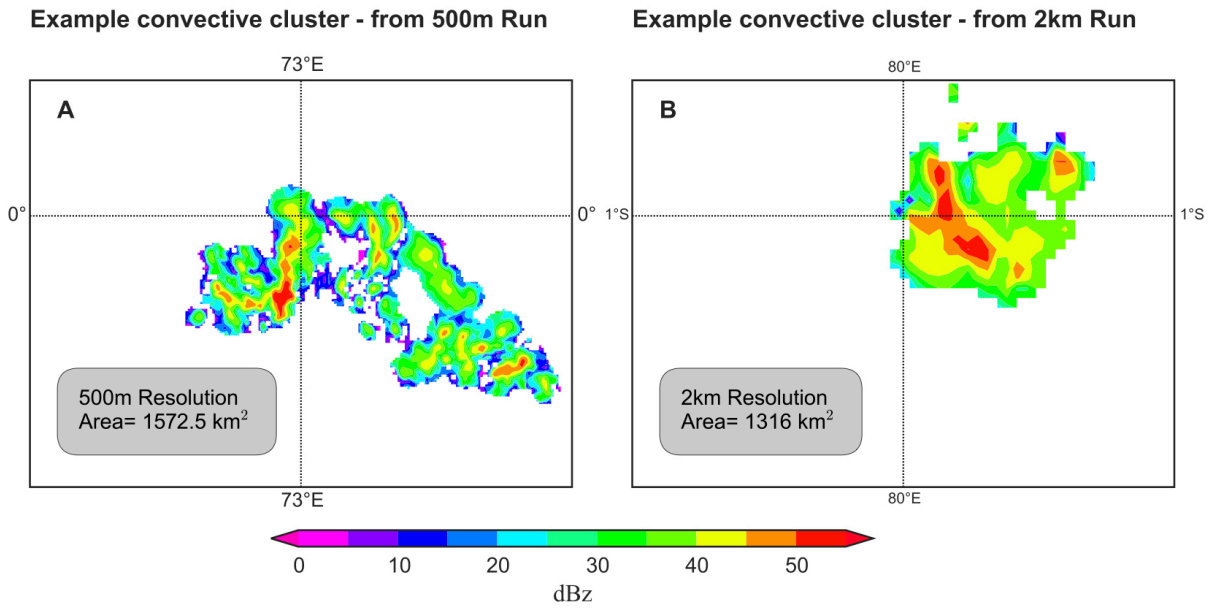

Figure 2.3: Reflectivity (dBZ) at 2.5 km for two sample convective clusters of similar size from the (a) 500-m and (b) 2-km runs. Note that the most intense part of the convective cluster is larger in the 2-km run.

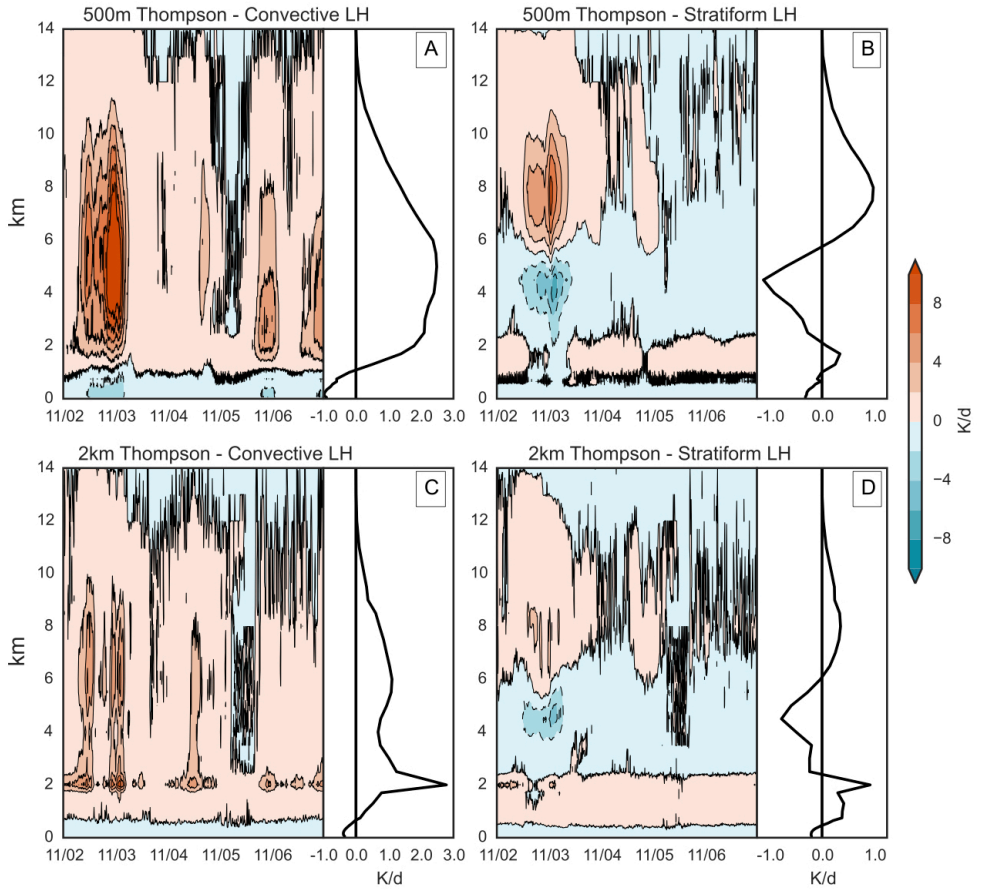

Figure 2.4: Example 5-day time series and time-averaged latent heating profiles ($Kday^{-1}$) for the (a) 500-m convective, (b) 500-m stratiform, (c) 2-km convective, and (d) 2-km stratiform clusters. All of the heating profiles are averaged over the same domain, which is indicated by the dark gray shading in Figure 2.1

and 2-km runs over the dark gray area in Figure 2.1. The time-averaged heating profile is attached to each time series. The 5-day period occurred during the suppressed phase of the MJO when large MCSs were largely absent. While the two time series have similar timing in peaks of heating, the vertical structure is quite different. For example, the 500-m convective heating is stronger and more vertically extensive while the 2-km run has a persistent low-level convective heating peak at 2 km that is much less evident in the 500-m

run (Figure 2.4a,c). The low-level heating is present in both models in weak stratiform clusters, but decreases in the 500-m run relative to the 2-km run (Figure 2.4b,d). About 31% of the model pixels that were classified as stratiform by the Steiner algorithm possessed heating at low levels. While shallow convection can sometimes be embedded in a stratiform rain region, this is not common in the tropics because of the evaporatively driven mesoscale descent (Brown, 1979) below the mid-level cloud base and the depressed mixed layer (e.g., Zipser (1977); Houze and Betts (1981); Johnson and Young (1983)). Thus it seems improbable that the subsiding and unsaturated downdrafts of the stratiform cloud cluster could consistently support low-level convection. There are two possibilities to explain the low-level stratiform heating peak. One is that the Steiner algorithm is incorrectly classifying convective pixels as stratiform, which—as shown below— is likely the case for clusters of small areal extent. However, some clusters with low-level heating remain in the stratiform category after areal extent is considered, which suggests that this heating peak may be an artifact of subgrid processes that are dependent on model processes such as the microphysics or PBL parameterization. The low-level peak was also present when the Morrison microphysics scheme was used for the 2-km run. To further explore the cause of this feature, a heat budget analysis for the boundary layer (not shown) and it was found that the low-level heating is primarily balanced by the vertical eddy fluxes. This suggests that excessive surface fluxes are found in the model, possibly associated with the PBL and surface schemes. The model SSTs are also fixed and do not respond to changing winds. A combination of all these factors could be the cause of this egregious feature.

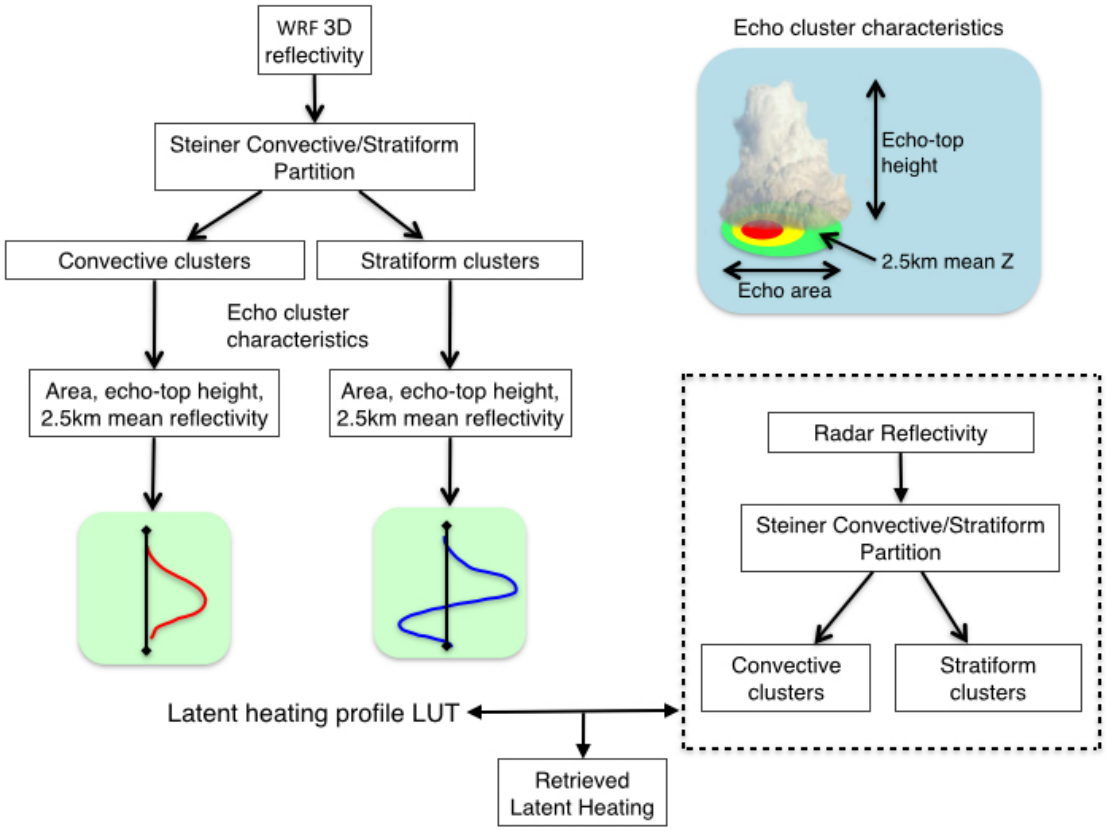

Figure 2.5: A schematic describing the flow of the CSA algorithm along with the radar echo cluster characteristics.

The construction of the heating retrieval algorithm is now described, which is also illustrated in Figure 2.5. The WRF reflectivity data from the 0.5 km grid is first smoothed for use on a 2 km grid as described above. This data is separated into convective and stratiform pixels and grouped into clusters. Three echo characteristics are calculated for each cluster; namely, the echo area at the 2.5-km level, mean reflectivity at the 2.5-km level, and mean 10-dBZ echo-top height. Each cluster was then binned by these three parameters. The echotop-height bins were spaced 1 km apart, extending from 0 to 14 km. The 2.5-km reflectivity bins ranged from 4 to 52 dBZ with a 4-dB interval. The bin sizes for the cluster areas were logarithmically spaced from 4 to 65, 536 km^2 to accommodate a range of values spanning several orders of magnitude. The bin sizes were chosen to ensure that all the bins in the LUTs were statistically representative with at least 10 samples in each bin. If a particular bin did not contain at least 10 samples, it was merged with a neighbor in such a way that their combined number of samples summed up to at least 10. The merging process first happens across the intensity dimension and then the echo-top-height dimension. The cluster area and echo-top heights can uniquely identify the cluster mean latent heating in most cases; the 2.5-km reflectivity is a proxy for the cluster rainfall intensity, distinguishing between dynamically active and decaying clusters of similar size and height. The latent heating profiles associated with all clusters in a given bin were averaged to have one representative heating profile per bin. The LUTs can then be applied to convective and stratiform clusters grouped from radar reflectivity data.

Upon examining the resultant LUTs, however, some unrealistic characteristics were

found:

1. *Low-level stratiform heating*—As already discussed, the model generally indicates low-level heating in regions of weak stratiform clusters (Figures 2.4 b,d) that is also evident in the stratiform LUT in Figure 2.6a, especially at small cluster areas. However, these clusters almost certainly represent warm rain convective processes in the tropics (Schumacher and Houze, 2003) so a rain type misclassification seems to be occurring. In addition, tropical stratiform precipitation is primarily found in MCSs (Rickenbach and Rutledge, 1998; Xu and Rutledge, 2015) and the MCS can be defined as having one horizontal dimension of at least 100 km in length (Houze, 1997). Therefore, the pixel-based Steiner classification algorithm is expanded using an area constraint; a conservative estimate of 200 km^2 is chosen as a threshold below which all stratiform clusters will be grouped under the convective category. The impact of the cutoff is shown in Figure 2.6b, where most of the low-level heating is now absent. In addition, clusters that are sized close to the model's horizontal resolution could include numerical artifacts. Therefore, all clusters that are less than 4 km^2 in size in the convective LUT are neglected.
2. *Elevated profiles*—Many of the stratiform rain clusters had latent heating profiles that transitioned from heating to cooling from 6 to 8 km, which is higher than expected based on the climatological height of the 0°C level of about 5 km over warm tropical oceans (Johnson et al., 1996). Stratiform cloud base is closely connected to the 0°C level (e.g., Leary and Houze (1979a)) such that cooling from sublimation

above this level is unrealistic in a region of stratiform rain. The WRF stratiform clusters with an elevated transition point also produced more cooling than warming in the column, with peak cooling greater than peak warming (e.g., Figure 2.7). This is also unphysical in a raining cloud system since rain at the surface implies positive column-integrated latent heating [see Fig. 11 of Cifelli and Rutledge (1998) for multiple examples of stratiform heating profiles from tropical field campaigns, all of which show greater warming in the column than cooling]. These profiles are termed anvil because the higher transition heights and net column cooling are more characteristic of non-precipitating anvil clouds. In the construction of the stratiform LUTs, the clusters with a larger mean cooling peak than a warming peak but with a mean 2.5-km reflectivity less than 36 dBZ were classified as anvil (2.6c). This removed most of the unphysical heating profiles from the modified stratiform LUT (2.6b), but still retained the largest and most heavily raining clusters. When partitioned in this manner, the anvil category comprised 27% of all stratiform pixels in the model. Figure 2.6 shows that the latent heating contributed by the anvil clusters is weaker than the heating from equally sized stratiform clusters, particularly for the very largest clusters, where they are about 3 to 4 times weaker in magnitude. Another difference between the modified stratiform and anvil LUTs is the height of the transition from heating to cooling. The stratiform clusters have a consistent transition height near 6 km. In the case of the anvil clusters, the transition starts around 8 km for smaller clusters and approaches 6 km as the size of the clusters increase. This is indicative of

the evolution of non-precipitating anvil clouds, where the anvil cloud base descends and areal coverage increases with time (see Figure 16 in Frederick and Schumacher (2008)).

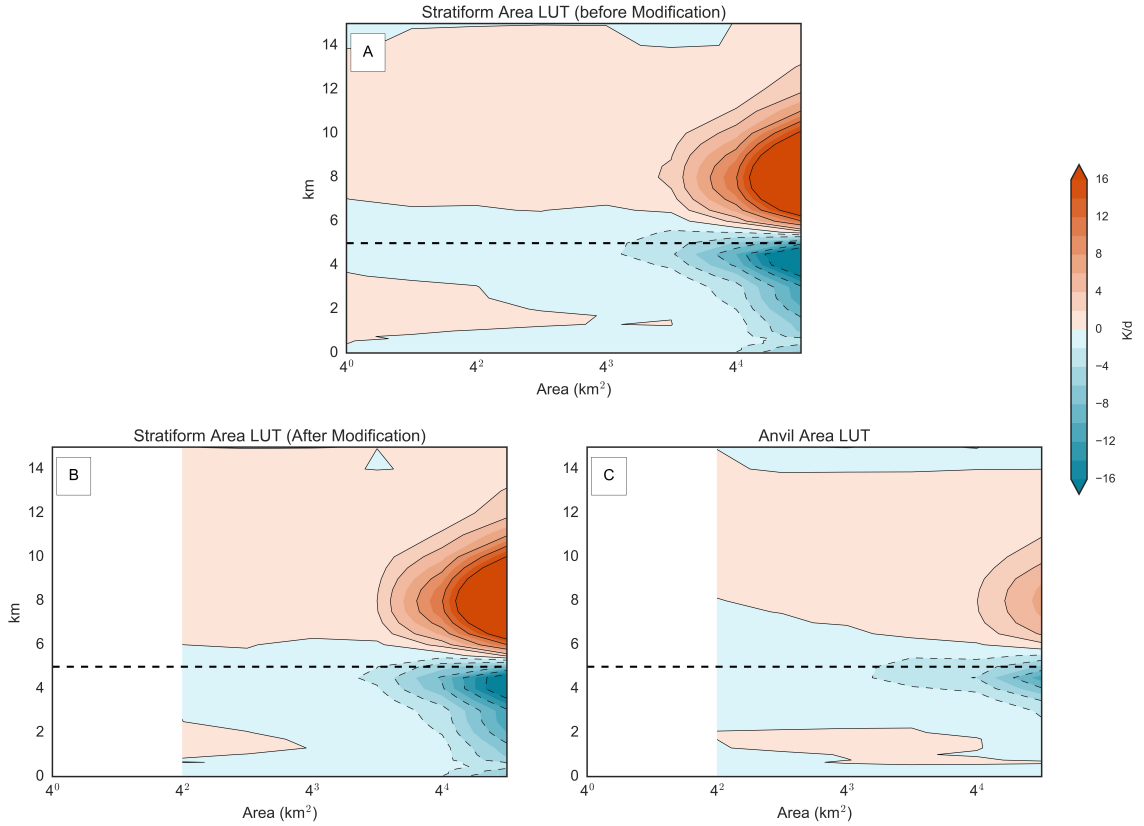

Figure 2.6: (a) Stratiform LUT before modification, separated into (b) final stratiform LUT and (c) anvil LUT. The cluster area bins, which were chosen to adequately represent the cell population of all sizes, are logarithmically binned. Note that the latent heating values in each bin are averaged over the number of clusters and over the area of the model domain. The broken horizontal line indicates the climatological melting level at 5 km.

It is known that WRF (Hopper and Schumacher, 2012) and other cloud-resolving models (May and Lane, 2009) have issues with overestimating non-precipitating anvil but it is unclear why the model creates these latent heating structures in rainy regions. Fig-

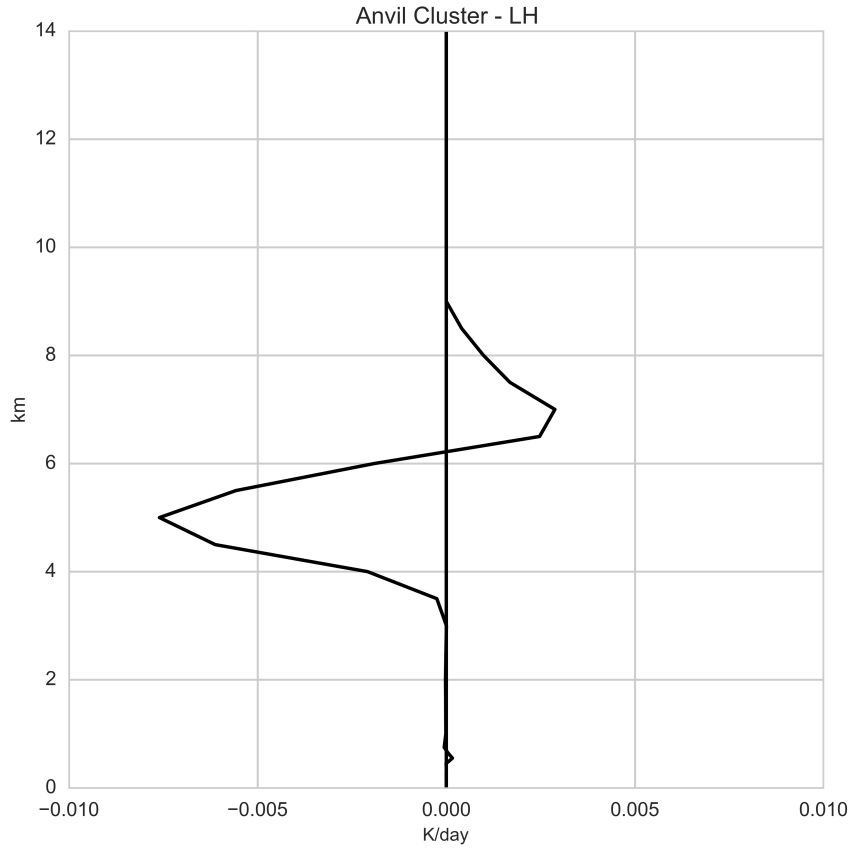

Figure 2.7: Example anvil latent heating profile.

ure 2.8 shows the rainfall and number distribution for convective, stratiform, and anvil clusters. Anvil produces less rain than the stratiform rain clusters when separated by area, mean echo-top height, and mean 2.5-km reflectivity. However, the number of anvil clusters in the model is generally greater than the number of stratiform clusters, especially for smaller areas ($10^3 km^2$) and small (5 km) mean echo-top heights. This is consistent with the fact that anvil can form from both convective and stratiform rain regions and is not constrained by mesoscale processes and thus mesoscale spatial scales. The rain fractions for the stratiform and anvil components were 22.1% and 4.6%, respectively, giving a com-

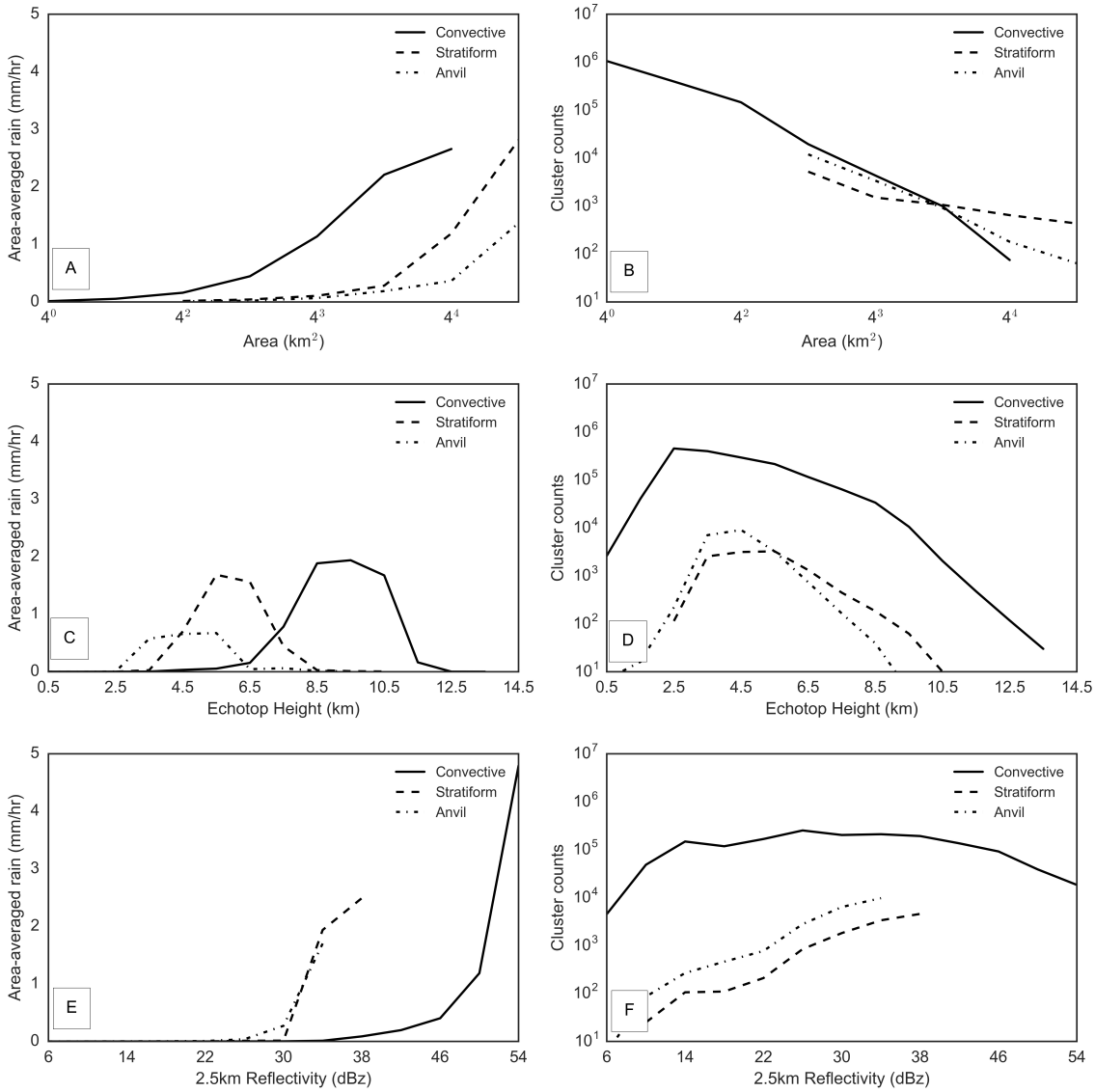

Figure 2.8: The bin-averaged rain rate (mmh^{-1}) in convective, stratiform, and anvil LUTs vs (a) area, (c) 10-dBZ echo-top height, and (e) 2.5-km reflectivity. (b),(d),(f) As in (a), (c), and (e), but for the cluster distribution in each of the LUTs.

bined rain fraction of 26.7%. This is less than the observed tropics-wide average of 40% from TRMM observations (Schumacher and Houze, 2003). However, the underestimation of stratiform precipitation is a common bias in CRM and WRF simulations that is attributed to treatments in the microphysics parameterizations (Varble et al., 2011, 2014).

The modified stratiform and convective LUTs binned by average cluster reflectivity, cluster area, and mean cluster echo-top height are shown in Figure. 2.9 (the stratiform cluster area plot is repeated from 2.6b. Figures 2.9a and b show that latent heating in the stratiform and convective LUTs is predominantly restricted to a small range of mean reflectivity values, with stratiform cluster maximum heating and cooling centered around 34 dBZ and convective cell maximum heating centered around 50 dBZ. Convective clusters with a mean 2.5-km reflectivity less than 32 dBZ have a distinctive region of cooling at midlevels and near the surface. The midlevel cooling is likely the result of detrainment driven evaporation and melting at cloud top in shallow convective and congestus clouds, while the near-surface cooling is likely a result of raindrop evaporation that creates cold pools (Feng et al., 2015). Figures 2.9c and d show that a larger area translates to a greater magnitude of heating for both stratiform and convective clusters, although the convective cluster area does not exceed the 16,384 km^2 bin. Figures 2.9e and 2.9f show how the latent heating is partitioned by the mean cluster 10-dBZ echo-top height. For stratiform rain, the greater part of the latent heating is contained in clusters with mean 10-dBZ echo-top heights between 5 and 7 km. The radar simulator built into WRF accounts for precipitating hydrometeors, but neglects cloud water and cloud ice (see section 3.2 in Hagos et al.

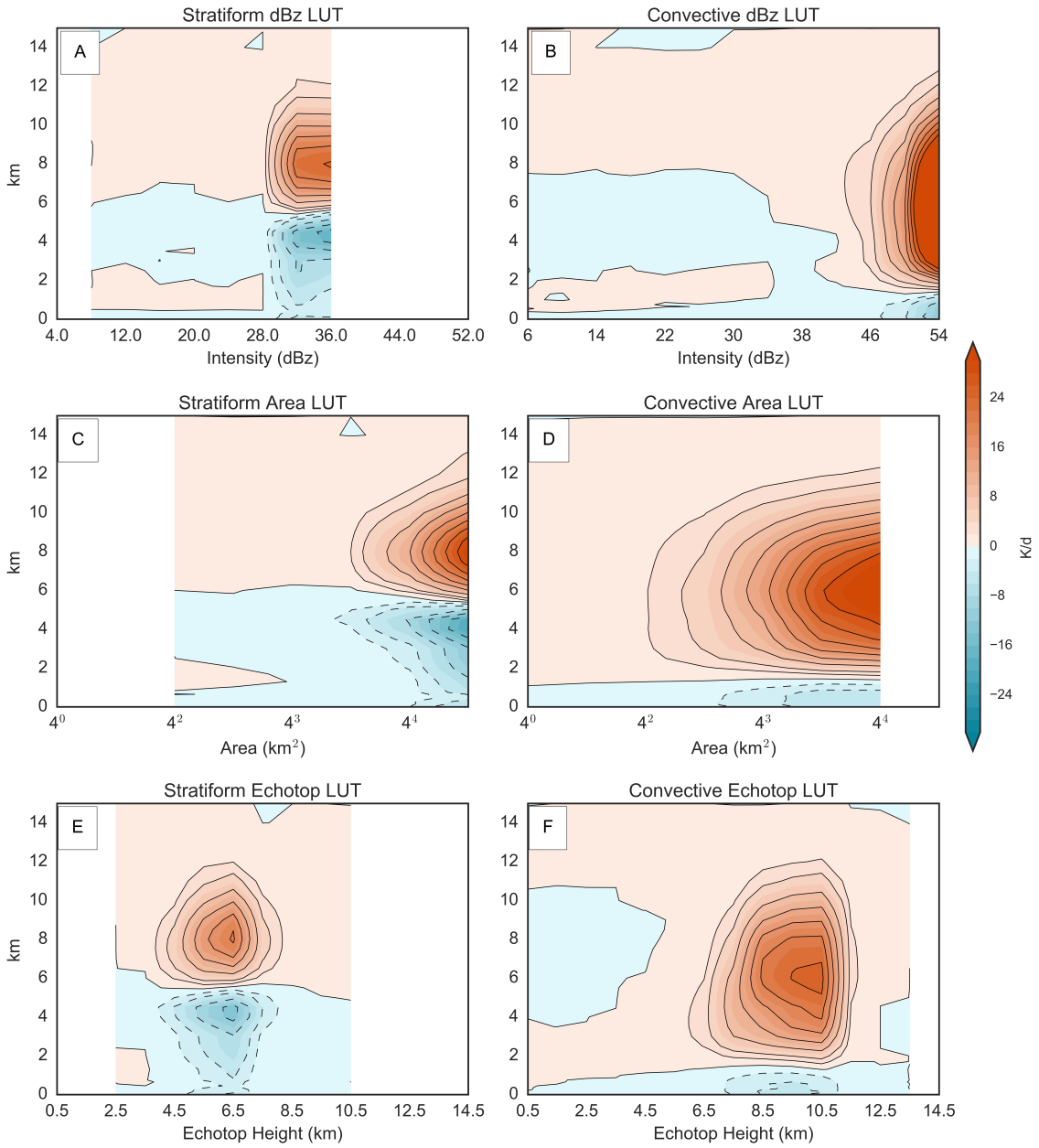

Figure 2.9: The (left) stratiform and (right) convective modified LUTs with the heating (K day21) distributed by (a),(b) cluster reflectivity; (c),(d) cluster area; and (e),(f) mean cluster 10-dBZ echo-top height. The heating is normalized by the number of clusters in each category.

(2014a)). The occurrence of heating above the 10-dBZ echo-top height is therefore possibly attributed to the presence of small hydrometeors that are invisible at S band (10-cm wavelength). Nevertheless, 10 dBZ was retained as the threshold for cell height because most scanning centimeter-wavelength radars are not fully sensitive below this threshold at distance (e.g., 150km) from the radar. The convective clusters show a deepening heating mode with increasing mean echo-top height. There is a heating maximum at 4 km for clusters with mean echo tops around 6 km, and a deeper maximum centered at 6km for mean echo tops greater than 8 km. This latter result is consistent with the fact that deep convective tropical heating is usually assumed to peak in the midtroposphere (6km; (Houze, 1982, 1989)). Figure 2.9f shows that the detrainment cooling at cloud top is restricted to shallow clusters having mean 10-dBZ echo-top heights less than 5 km. This result is consistent with the Q1 profiles for congestus clouds observed during the Kwajalein Experiment (Schumacher et al., 2008).

Figure 2.10 compares the latent heating that is produced directly from the model microphysics scheme with the reconstructed heating from the LUTs in Figures 2.10 for 20 days in November 2011 during DYNAMO for convective and stratiform rain regions. Hereinafter this LUT method is referred to as the convective-stratiform area (CSA) algorithm. CSA is able to accurately reconstruct the latent heating time series, capturing all the variations including the inactive period early in the month, the buildup in shallow convection in the middle of the month, and the burst of deep convective and stratiform heating in the latter half of the time series. The mean convective and stratiform latent heating profiles

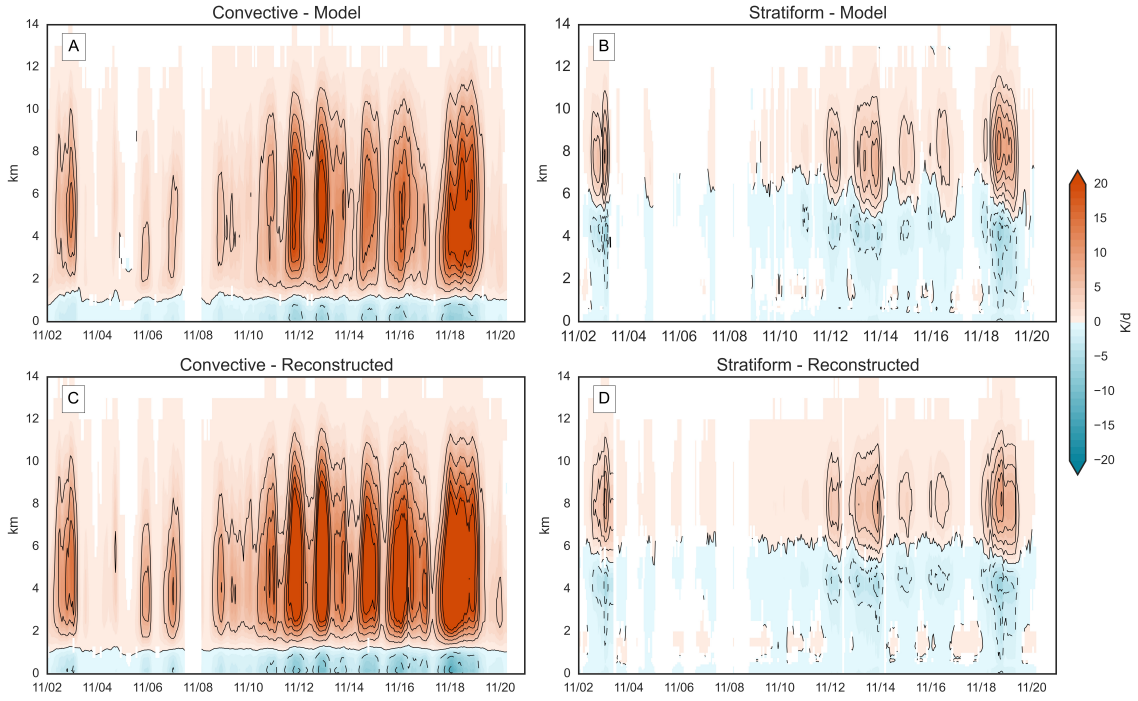

Figure 2.10: For November 2011, (a) convective and (b) stratiform model latent heating, along with (c) convective and (d) stratiform latent heating reconstructed using the CSA algorithm. The latent heating values ($Kday^{-1}$) are hourly values averaged over the entire model domain.

for the model and CSA reconstruction are also consistent (not shown). A stronger test for robustness of the algorithm was also performed by reconstructing the first half of the time series using a LUT constructed from the second half and as seen in Figure 2.11, the LUT was able to satisfactorily reproduce the model heating.

II.4 Application to S-PolKa observations

It is important to preface this section with a note on the convergence problem of model physics, as identified in Arakawa (2004) and Jung and Arakawa (2004). In these studies, the authors pointed out that no amount of time and space averaging can make the heating profiles from high-resolution models converge with those of the low-resolution models because the transport resolved by the high resolution models is subgrid-scale in low resolution models. A characteristic of CRM-derived stratiform heating profiles is sharp heating and cooling peaks, along with a sharp transition from heating to cooling [see Figs. 5b and 10 in Shige et al. (2004) and Fig. 9 in Skyllingstad and de Szoeke (2015)]. This is in contrast to the smooth heating profiles from "low resolution" heating budgets (Stachnik et al., 2013). Therefore, an exact match between the CRM profiles and observed large-scale budget studies is not to be expected. The CSA algorithm was applied to the observed radar reflectivity from the range-height indicator (RHI) sector scans from S-PolKa for 2 October to 30 December 2011. The RHI scans were executed from an elevation angle of 0.5°to 40°at an azimuthal increment of 0.5°. The RHI sector is shown in Figure 2.1 of Hagos et al. (2014a) and was chosen over the surveillance scans (with 11°maximum ele-

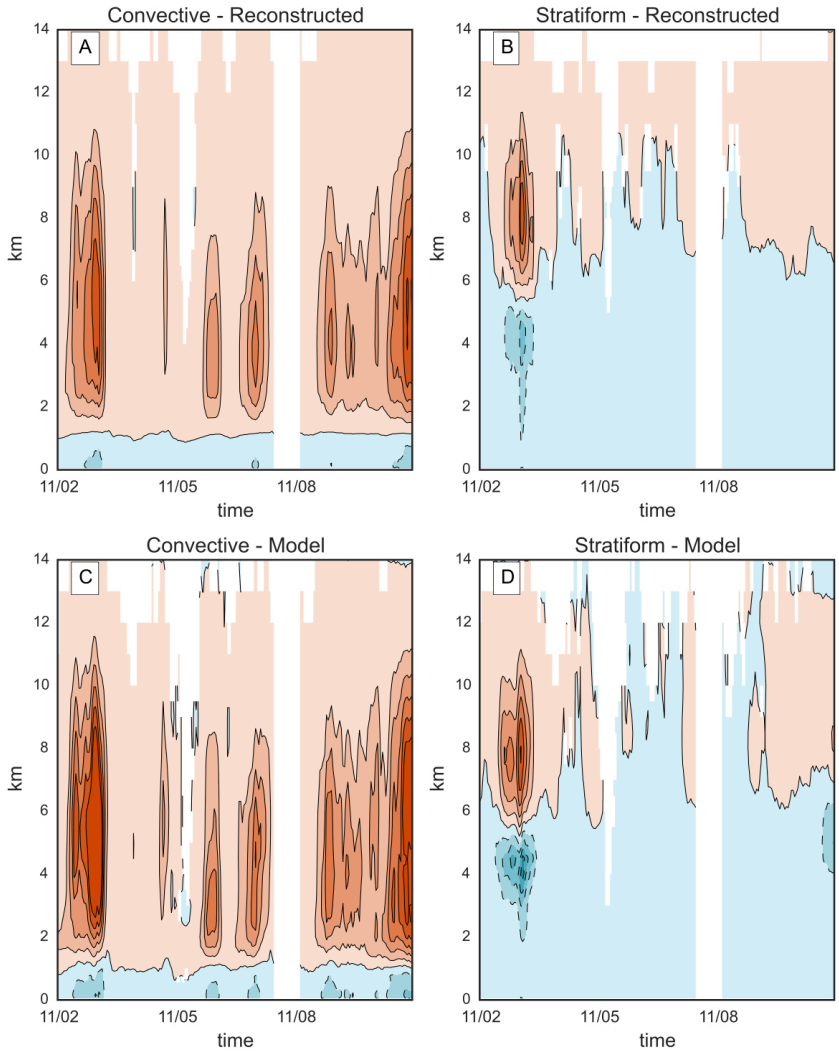

Figure 2.11: For November $2^{nd} - 10^{th}$ 2011, (a) convective and (b) stratiform reconstructed latent heating, along with (c) convective and (d) stratiform model latent heating.The LUT used in the reconstruction was obtained from the second half of the model run (November $11^{th} - 20^{th}$). The latent heating values ($Kday^{-1}$) are hourly values averaged over the entire model domain.

vation) because of greater vertical coverage close to the radar. The heating from the CSA algorithm was then compared with two other latent heating retrievals, one based on the idealized profiles from Schumacher et al. (2004) described in the introduction (hereinafter, SHK04) and the other, the Q1 sounding budget method described in section II.2. Figure 2.12 shows the average latent heating profile for the 3-month period for each method and includes CSA profiles with (CSA unmodified) and without (CSA modified) anvil included in the stratiform LUT. The SHK04 and Q1 profiles are consistent, in part because the overall magnitude of heating is expected to agree between these two methods given that both techniques are constrained using the same S-PolKa estimated surface rainfall. However, the distribution of heating in the vertical is determined independently. The CSA latent heating profiles have a double heating peak at 3.5 and 8 km in contrast to a single heating peak found in the Q1 profile at 5.5 km. The magnitude of the CSA- unmodified peak is $3\ K\ day^{-1}$, as compared with the variational analysis peak of $4\ K\ day^{-1}$. Excluding the anvil-like stratiform clusters (CSA modified) increases the heating magnitude at mid- and upper levels, but the mean latent heating profile still retains a distinct minimum at midlevels, which is indicative of strong stratiform cooling in the model. The modified CSA heating profile shows a stronger upper-level heating peak of comparable magnitude ($3.5\ K\ day^{-1}$) to the variational analysis, albeit at a higher elevation (7 km) potentially indicative of a larger stratiform component. A low-level heating peak of $3\ K\ day^{-1}$ is observed near the 3-km level, which is a signature of the bottom-heavy convective heating. The SHK04 profile does not show a sharp cooling at midlevels because it uses smooth,

idealized input profiles.

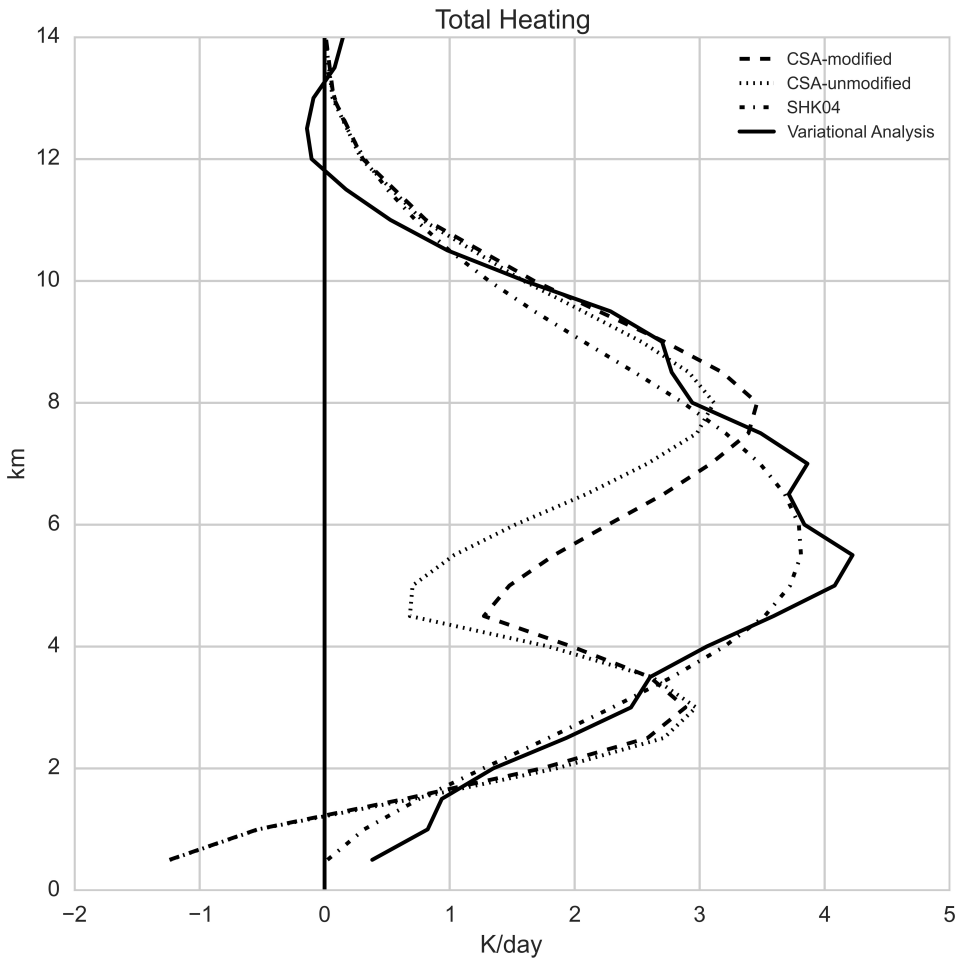

Figure 2.12: S-PolKa-derived latent heating ($Kday^{-1}$) profiles from 2 Oct to 30 Dec 2011. The variational analysis heating profile represents Q1 from the reanalysis and sounding budget over the S-PolKa area.

Figure 2.13 separates the convective and stratiform components of the SHK04 and CSA latent heating profiles from Figure 2.12. There is good correspondence between the magnitudes of the convective heating profiles (Figure. 2.13a), even though the CRM-based convective heating is more bottom heavy than the idealized heating profile from SHK04.

Clear differences exist in the stratiform profiles (Figure 2.13b). The transition from lower-level cooling to upper-level heating occurs at 5 km in SHK04 as compared with 6.5 km in the uncorrected CSA. The magnitudes of the uncorrected heating and cooling peaks are larger when compared with SHK04 (22.2 vs 20.5 $Kday^{-1}$), giving net cooling in the column despite the presence of surface rain. This feature, as discussed in section 3, is unphysical, and the exclusion of the anvil heating from the LUT results in an average heating profile with a lower transition level (6 km). The heating peak in the corrected stratiform profile is also larger than the idealized heating of SHK04 (1.7 K vs 0.5 $Kday^{-1}$). This increase in the stratiform heating makes the overall heating profile more top heavy. However, the altitude of the cooling peak in the corrected stratiform heating remains near 4 km, suggesting that cooling from melting near the 0°C level is a dominant process in the model.

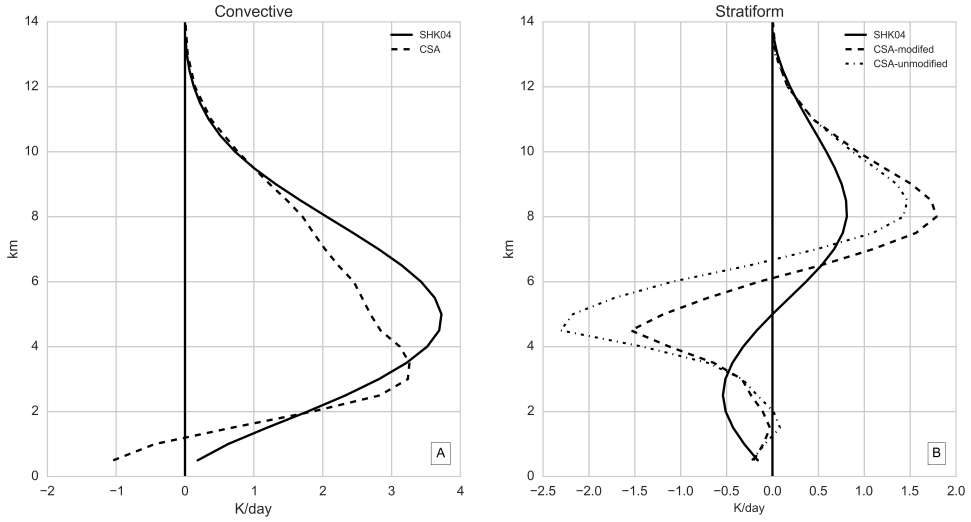

Figure 2.13: S-PolKa-derived latent heating ($Kday^{-1}$) profiles from 2 Oct to 30 Dec 2011 for (a) convective and (b) stratiform rain regions.

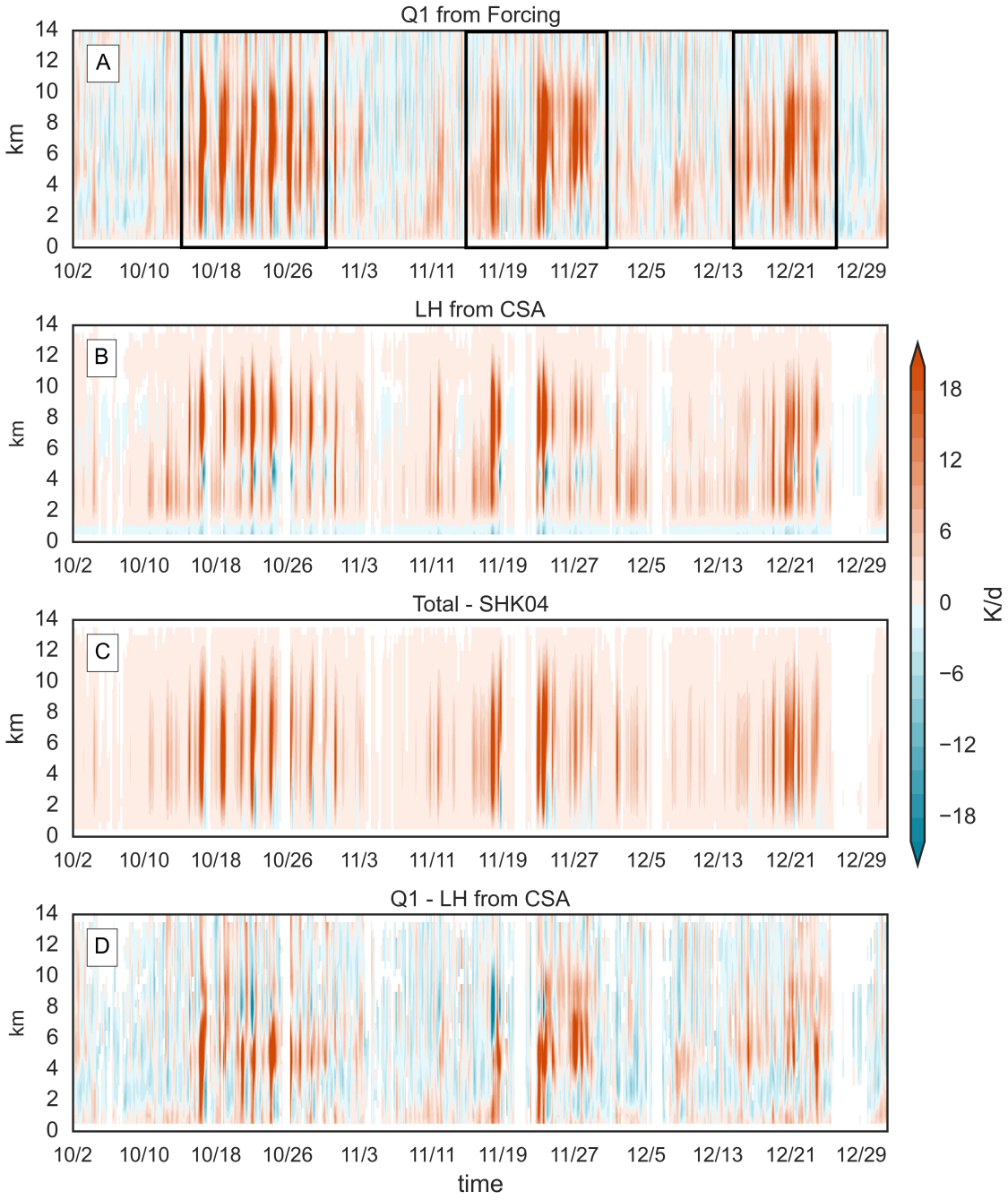

Figure 2.14: Time series from 2 Oct to 30 Dec 2011 for (a) Q1 from the forcing dataset, (b) S-PolKa latent heating from CSA, (c) S-PolKa latent heating from the SHK04 algorithm, and (d) the difference between Q1 and CSA-derived latent heating. White areas indicate times when the heating was between ,$\pm 10^{-3} K day^{-1}$ which includes days when S-Pol was not in operation. Black rectangles in (a) indicate active phases of the MJO.

Figure 2.14 depicts the S-PolKa latent heating time series from 2 October to 30 December 2011 for the variational analysis Q1, CSA, and SHK04 methods. The three MJO active phases are seen in the heating sig- natures for October (15–27), November (16–29), and December (16–26) and are indicated by black boxes. Each event shows a rise in the heating peak, typifying the westward tilt in heating associated with the MJO (Kiladis et al., 2005; Benedict and Randall, 2007), followed by a quiescent period. Each method captures the temporal variations in convective activity during this time period. The transition from shallow to deep heating is clearly captured by the CSA method in the altitude of peak heating (Figure 2.14b); however, the SHK04 heating profiles do not vary as much in height in the buildup to the active MJO because it only assumes two possible convective heating profiles (Figure 2.14c). SHK04 also shows much less variation in low-level cooling than does the CSA method because of its single stratiform profile that has no sensitivity to variations in the mesoscale downdraft and evaporation below cloud base. Another advantage of using the CSA over the SHK04 is that the former can capture the transition in time of the convective and stratiform peak heating. The accurate representation of this temporal variability of the shape of the heating could be fundamental to MJO simulations (Lin et al., 2004) and its theoretical description (Mapes, 2000). The CSA method also captures the top-heaviness of the heating profiles better than the SHK04 technique during the periods of active MJO (indicated by black boxes in Fig. 13a). However, an examination of the mean heating profiles in Figure 2.12 suggests that the CSA might be exaggerating the magnitude of midlevel cooling. The difference between the Q1 and the CSA-derived latent heating

(Figure 2.14d) shows the temporal variation of differences seen in Figure 2.12. The cooling due to evaporation near the boundary layer is captured in the CSA method, but is not visible in Q1. The quantity Q1 also produces greater values of heating at midlevels during the active MJO, which can be traced to the strong cooling seen in CSA's stratiform profiles. During the convectively quiescent times, Q1 is likely to be dominated by longwave cooling that is not included in the CSA retrieval. The CSA algorithm is able to reproduce a realistic time series of latent heating without any rain rate information. Since radar-derived surface rain was used to constrain the forcing dataset, the CSA heating profiles represent a less-derived product that is directly obtained from the radar reflectivity data and information about the organization of the convective system.

Since the CSA LUT was created using a region that was much larger than the S-PolKa domain (Figure 2.1), it could have a cluster distribution much different from what is seen by the radar. Figure 2.15 compares the histogram of S-PolKa stratiform cluster area distribution from 2 October to 30 December with that of the model for 1-20 November. All of the clusters are on the order of $10^3 km^2$, whereas the model stratiform LUT in Figure 2.9 extends to $10^4 km^2$. To assess whether the scale mismatch between the model and radar domains would affect the CSA performance, another LUT was created that only considered precipitating echoes within a model region similar to the size of the S-PolKa 150-km radius domain (the dark gray area in Figure 2.1). This radar domain-sized LUT was also made statistically representative by imposing the condition of including at least 10 samples per bin. Figure 2.16 compares the convective and stratiform heating profiles from the full and

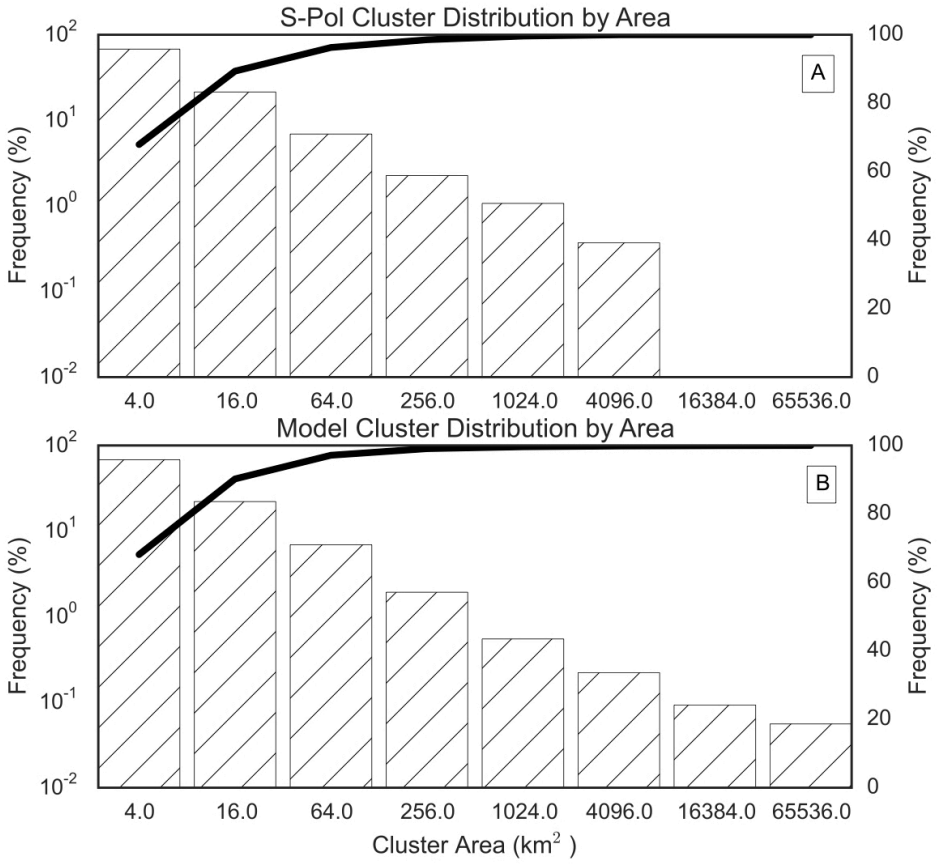

Figure 2.15: (a) S-PolKa and (b) model stratiform clusters distributed by area from 2 Oct to 30 Dec 2011. The left y axis is logarithmic and shows the stratiform cluster distribution. The dark line is the cumulative distribution function and is shown using the linear y axis, on the right.

truncated model domain LUTs. There is little change in the convective heating profiles, but the stratiform cooling and heating peaks diminish in magnitude by about 0.3 and 0.5 $K\ day^{-1}$, respectively. This decrease in magnitude is most likely due to the fact that the largest stratiform clusters (which produce the largest heating and cooling, as seen in Figure 2.9c) are too large for a typical ground-radar domain to capture. The time series of latent heating from the radar-sized domain also corresponds well with that from the full model

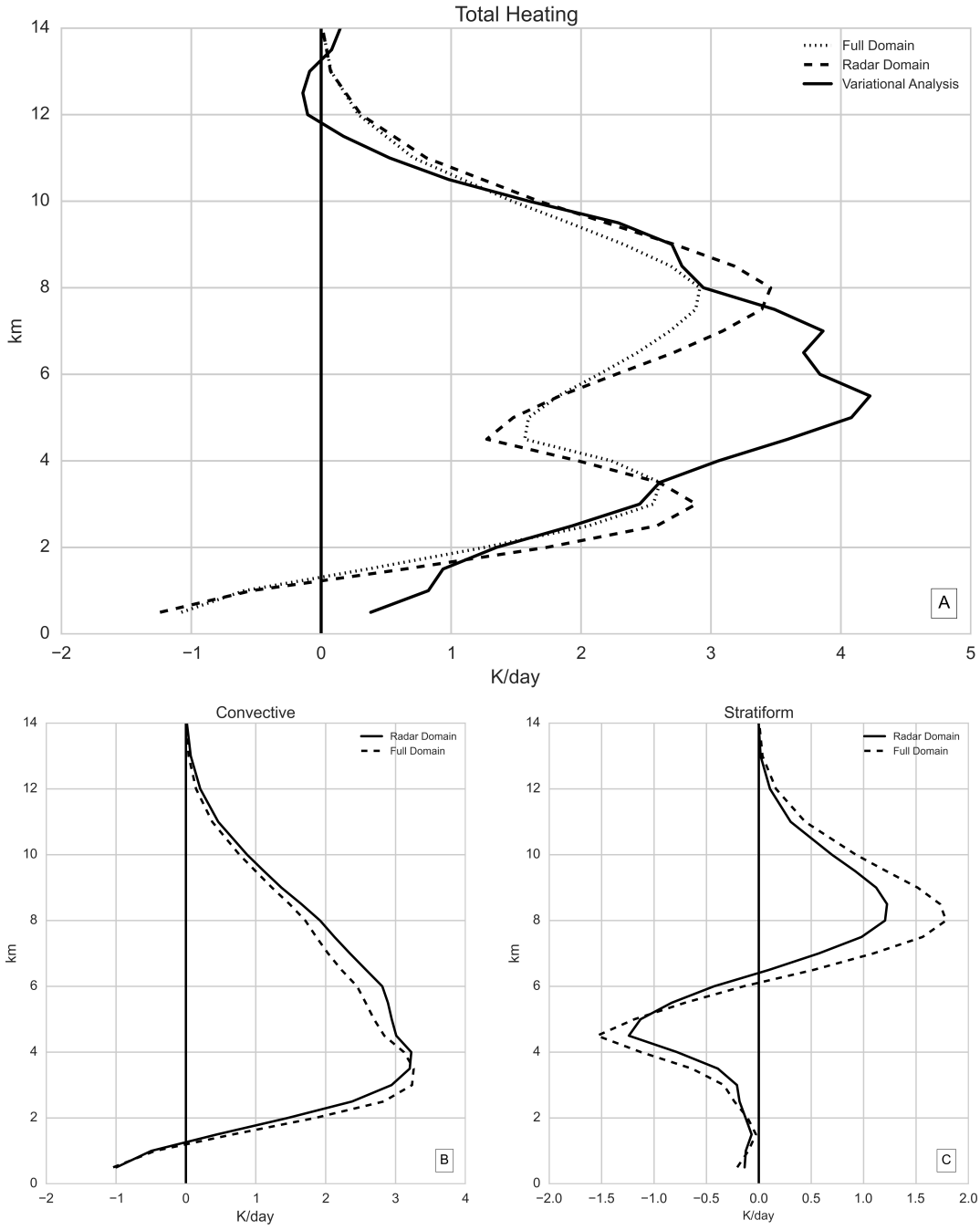

Figure 2.16: S-PolKa latent heating profiles ($Kday^{-1}$) from the radar-scale domain and the full model domain for (a) total, (b) convective, and (c) stratiform rain regions using the CSA algorithm. The Q1 profile from the variational analysis is included in (a).

domain (not shown).

II.5 Summary

A new technique is presented to retrieve latent heating profiles from ground-based or spaceborne radar-observed precipitating echo characteristics (i.e., size, mean echo-top height, and mean low-level reflectivity) rather than derived rainfall information. Contiguous regions of convective and stratiform rain are grouped to form clusters, which are then assigned heating profiles based on output from a 500-m regional WRF simulation during the DYNAMO/CINDY2011/AMIE field campaign. The 500-m run was chosen over the 2-km run after it was found that it improved upon the pervasive low-level heating peak in the convective and stratiform heating profiles. Reclassifying regions smaller than 200 km^2 as convective also reduced the incidence of the low-level heating peak in stratiform profiles.

The model clusters were sorted according to area at 2.5km, mean 10-dBZ echo-top height, and the average reflectivity at 2.5 km to create a set of lookup tables. The original stratiform LUT included heating profiles that showed transition from heating to cooling well above the 0°C level that led to net column cooling (unphysical when rain is present). The anvil-like heating profiles with weak rain near the surface were removed from the stratiform LUT to mitigate some of these issues. The first issue is most likely due to an error in the convective-stratiform separation technique, but both issues potentially highlight problems in the model resolution as well as PBL and microphysics parameterizations.

The CSA LUTs were applied to S-PolKa reflectivity observations and the resulting latent heating profiles were generally consistent with the Q1 from variational analysis and the latent heating retrieval from S-PolKa using the simpler SHK04 method, including capturing realistic temporal variations associated with the evolution of the MJO. However, the CSA stratiform LUT produced much larger cooling near the melting level, as would be expected based on arguments made in Arakawa (2004) . A sensitivity test showed that the CSA technique can be applied across scales ranging from a relatively small radar domain to a larger model domain in the near-equatorial Indian Ocean to produce quantitatively similar results. Future algorithm development will include further investigation into the cause of the anomalous low-level heating spike in the WRF stratiform profiles and the anvil-like net cooling in regions of stratiform rain. The robustness of the technique can also be assessed using LUTs from other tropical oceanic and land field campaigns. Since the heating properties of the clusters themselves are expected to be unchanging over different seasons with only their frequency varying, the LUTs generated for one season can be expected to be valid in another, at least over tropical oceans. In other regimes, such as land or monsoonal regions, a model that can satisfactorily capture the convective variation in those regimes will have to be run again, to generate the LUT. Any biases in those models will be addressed on a case- by-case basis. There is optimism regarding the application of the CSA in higher latitudes [e.g., for NASA's Global Precipitation Measurement (GPM) program] where a heating retrieval based on the size and organization of a system may be more robust and physically realistic than pixel, rain-based estimates. This is because midlatitude con-

vection, though forced by different large-scale dynamics than tropical convection, is still often organized into mesoscale convective systems (Maddox, 1983; Parker and Johnson, 2000), with distinct heating structures for convective and stratiform components.

After having analyzed the latent heat release from convection, which is form of the influence of the convection on the environment, the focus of the remainder of the study will be on how the environment modulates the occurrence and organization of convection, particularly via changes to the moisture field. This subject is addressed in the following chapters.

CHAPTER III

CONVECTIVE AND STRATIFORM COMPONENTS OF THE PRECIPITATION WATER VAPOR RELATIONSHIP*

III.1 Background

This chapter deals with the examination of the precipitation-moisture relationship in the tropics. As hypothesized by Raymond (2000), moisture exerts control on tropical precipitation. Bretherton et al. (2004) first showed that there exists an empirical relationship between column moisture (*r*) and precipitation (P) using satellite data. They demonstrated that the average precipitation in a satellite grid (2.5 x 2.5 °grid) is only weakly sensitive to the column moisture up until a threshold, beyond which the precipitation rapidly increases and approximately follows a power-law distribution (also noted by Peters and Neelin (2006) and Neelin et al. (2009)). Column water vapor or column saturation fraction, *r*, is generally used as a measure of the column moisture content in these studies. This relationship was also confirmed for radiosonde observations in the West Pacific (Holloway and Neelin, 2009, 2010) and East Pacific and Atlantic (Raymond et al., 2007). More recent studies have shown that organized deep convective systems dominate the rapid pickup in precipitation beyond the critical column saturation point compared to isolated convective systems (Masunaga, 2012; Tan et al., 2013). The P-*r* relationship as an observed statisti-

*Reprinted with permission from "Convective and stratiform components of the precipitation-moisture relationship" by Ahmed, Fiaz and C. Schumacher, 2015 in *Geophysical Research Letters*, 42, **10**,453-462. Copyright [2015] by American Geophysical Union.

cal relationship between the large-scale moisture and precipitation is a test of fidelity for modeling studies and central to stochastic modeling of tropical convection (Neelin et al., 2008; Hottovy and Stechmann, 2015).

In this study, ground radar data from the Dynamics of the Madden-Julian Oscillation (DYNAMO) field campaign and satellite data from the Tropical Rainfall Measuring Mission (TRMM) is used to expound on the P-*r* relationship, by separating its convective and stratiform components. It is found that stratiform and convective rain systems have markedly different empirical relationships with column moisture. The area-averaged rainfall is also separated into conditional rain rates–which represents intensity–and the area of rainfall. It is found that the increase in rainfall intensity is nearly linear with r, while the increase in rain area is nonlinear and explains much of the nonlinearity in the canonical P-*r* curve. A physical interpretation for the differences and a discussion of the implications of these findings for cumulus parameterization schemes is provided towards the end of the chapter.

III.2 Datasets and methodology

III.2.1 DYNAMO

Hourly rainfall observations for a 4 month period (2 October 2011-9 February 2012) were obtained from the Shared Mobile Atmospheric and Research Teaching Radar (SMART-R), deployed in the equatorial Indian Ocean on Addu Atoll during the DYNAMO field campaign (Yoneyama et al., 2013). The radar reflectivity was classified into convec-

tive and stratiform categories using the Steiner et al. (1995) partitioning algorithm. Convective rain refers to rain produced by systems that have strong updrafts throughout the depth of the troposphere and the primary form of hydrometeor production is collision-coalescence for water and riming for ice. Stratiform rain, on the other hand, has weaker updrafts aloft and a mesoscale downdraft below the 0°C level, form hydrometeors primarily by vapor deposition aloft and has weaker precipitation intensities than convective rain. It is noted that only the eastern part of the SMART-R radar domain was included in the analysis, which encompassed about 27000 km^2 of area.

Hourly averaged temperature and vapor pressure data were obtained from the merged sounding product that utilizes information from soundings, surface instruments, and ECMWF model output (https://www.arm.gov/ data/vaps/mergesonde). The mergesonde product includes observations from radiosondes that were launched eight times daily and values from the European Centre for Medium-Range Weather Forecasts (ECMWF) model output. r is used as the measure of water vapor in the column, given by W/W*, where W and W* are the water vapor path and the saturation water vapor path, respectively. In this study, saturation is assumed with respect to liquid water at all heights. It was found that the results of this study do not change when saturation is assumed with respect to ice below the freezing level. Hereon, precipitation refers to the domain-averaged precipitation, whereas conditional precipitation refers to the mean rain intensity only over raining regions. Conditional precipitation for a given category, convective or stratiform, is computed by dividing the rain amount by the number of raining pixels, in that category.

III.2.2 Global data

Satellite observations of precipitation from the Tropical Rain Measuring Mission's (TRMM) Precipitation Radar (PR) were obtained, for eleven years from 1998 to 2008. TRMM PR pixels were classified into convective, stratiform, and shallow using the 2A23 algorithm (Awaka et al., 1997, 2007) , which utilizes vertical variations in reflectivity in addition to the horizontal-only method of Steiner et al. (1995). Shallow pixels refer to those pixels with no detectable echo (i.e., < 18 dBz for the TRMM PR) at a height of 1.5 km below the melting level. The 2A25 algorithm (Iguchi et al., 2009) then corrects for attenuation and retrieves rainfall from the 2A23 output. The TRMM rainfall products from 35°N to 35°S were gridded onto a 2.5°X 2.5°grid at daily and monthly time scales. Since TRMM overpasses do not typically sample the same region more than once a day, the daily TRMM rainfall values are effectively instantaneous measurements of P. The number and rain rates for convective, stratiform, and shallow raining pixels in each 2.5°X 2.5°grid are kept track of. This information was then used to compute the domain-averaged precipitation and conditional rain rates for each rain category in every grid. Moisture and temperature variables used to compute column moisture content were obtained from NASA's Modern Era Retrospective-Analysis for Research and Applications (MERRA) data set (Rienecker et al., 2011), which was also produced on the same 2.5°X 2.5°grid as the TRMM precipitation products. It is noted that the TRMM PR grid box is about three times as large as the SMART-R domain.

III.3 Results

III.3.1 P-*r* relationships in ground radar data

As outlined in Houze (1997), convective and stratiform precipitation differ in microphysical makeup (Leary and Houze, 1979b,a) and their interactions with the large-scale environment (Mapes, 1993; Schumacher et al., 2004) . Categorization into convective or stratiform can fully determine the dynamical characteristics of tropical convective systems (Mapes and Houze, 1995). It is therefore natural to question the nature of the relationship between these building blocks of tropical rainfall and environmental humidity. Figure 3.1 shows scatterplots between the domain-averaged hourly SMART-R rainfall and *r* derived from radiosonde observations at Gan Island. Figure 3.1a shows that the long tail of the total rainfall distribution increases rapidly beyond a critical r value (r_c) of ~0.7. Convective precipitation, however, shows an increase in amount above r_c. (Figure 3.1b). Stratiform precipitation, which is negligible below r_c and appears to rapidly pick up above it (Figure 3.1c). Thus, the hourly precipitation data set from the DYNAMO field campaign suggests that the rapid pickup in the P-*r* relationship is more representative of stratiform than convective rainfall.

The points representing hourly surface rainfall data from Figure 3.1 were then distributed among bins of *r* spaced at intervals of 2.5%. The mean precipitation in each histogram bin was fit by a power law of the form $P_h(r) = ar^b$ using a log transformation and a linear least squares fit, where P_h is the mean rainfall in each bin, *r* is the column saturation fraction, and *a* and *b* are data set-dependent constants. The exponent of the curve, *b*, is a

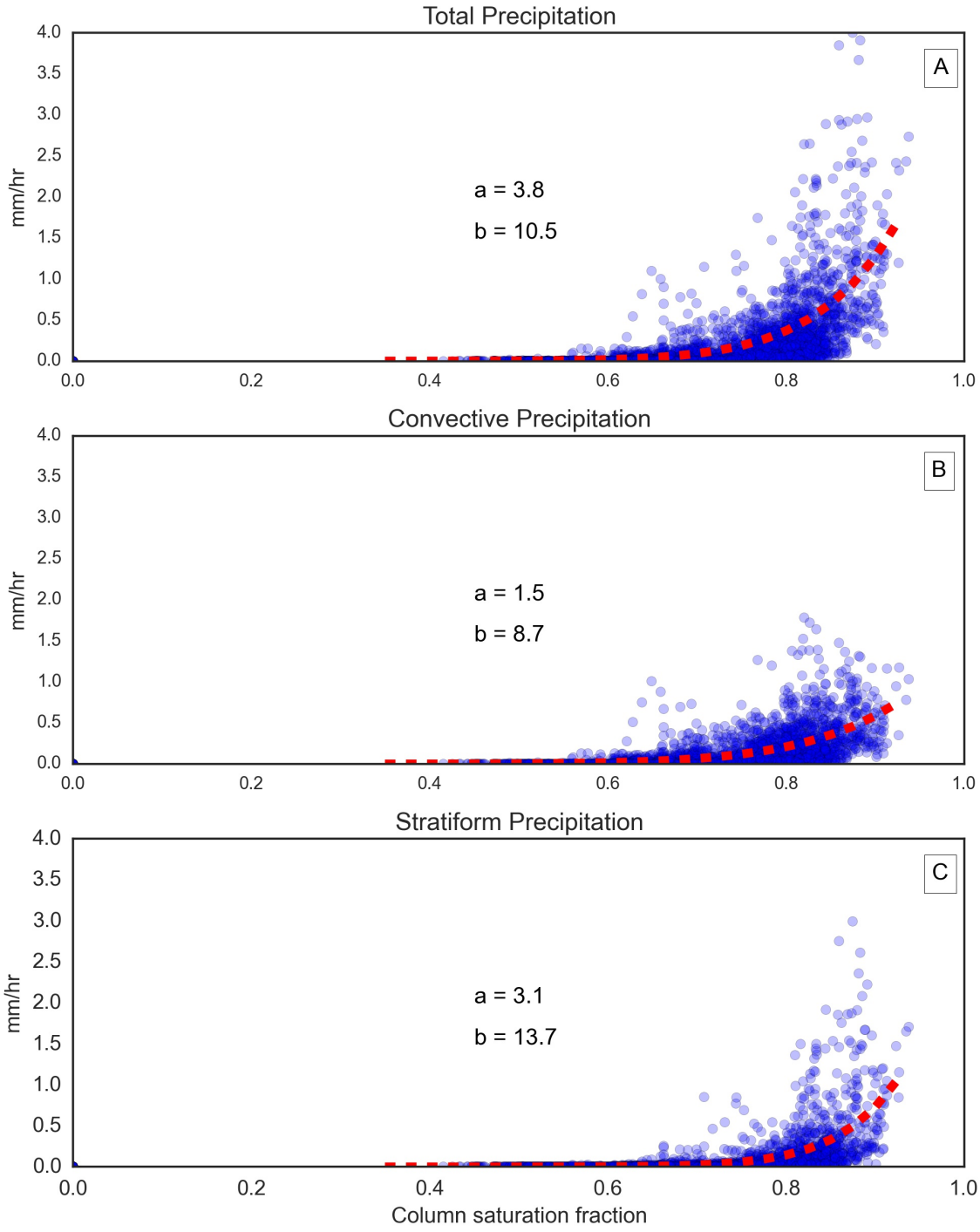

Figure 3.1: Scatterplot between column saturation fraction and hourly (a) total, (b) convective, and (c) stratiform area- averaged rainfall from SMART-R. The red line corresponds to the rainfall from a power-law fit with parameters “a” and “b”. “b” characterizes the abruptness of the pickup.

measure of the nonlinearity of the curve and can be assumed to measure the–abruptness–or the strength of the pickup in the P-r curve. Curves with larger b values therefore have a stronger pickup than curves with a smaller b. The parameter a also assumes a physical interpretation in this case: it represents the domain-averaged rainfall or rain area in a completely saturated column (i.e., when $r = 1$). The red dashed lines in Figure 3.1 show the power-law fit for total, convective, and stratiform precipitation, with the fits generally well representing the individual data points. Convective rainfall has a less rapid pickup than stratiform and total rainfall, as evidenced by their respective b values (8.7 versus 13.7). The a value, which represents the area-averaged rainfall for r = 1, is greater in stratiform rain compared to convective rain (3.1 versus 1.5). However, it is b that characterizes the nature of the pickup as smooth or abrupt.

Figure 3.2 shows the relationships of conditional rainfall and the average percentage of the radar grid covered by raining area. Figures 3.2a, 3.2c, and 3.2e show that the increase in conditional rain rates with r is weakly nonlinear with small b values, especially the total and convective rain categories. The fact that there are very few values of zero conditional convective rain (Figure 3.2c) indicates the ubiquity of convective rain in the tropics. Figures 3.2b, 3.2d, and 3.2f show that the nonlinearity in Figure 3.1 arises largely from the nonlinear increase in rain area. These curves have higher b values than their counterparts in conditional rain. It is interesting to note that even here, there are significant differences between the convective ($b = 7.5$) and stratiform ($b = 10.2$) raining pixels.

In addition, there are clear differences in the fraction of the radar area that is covered

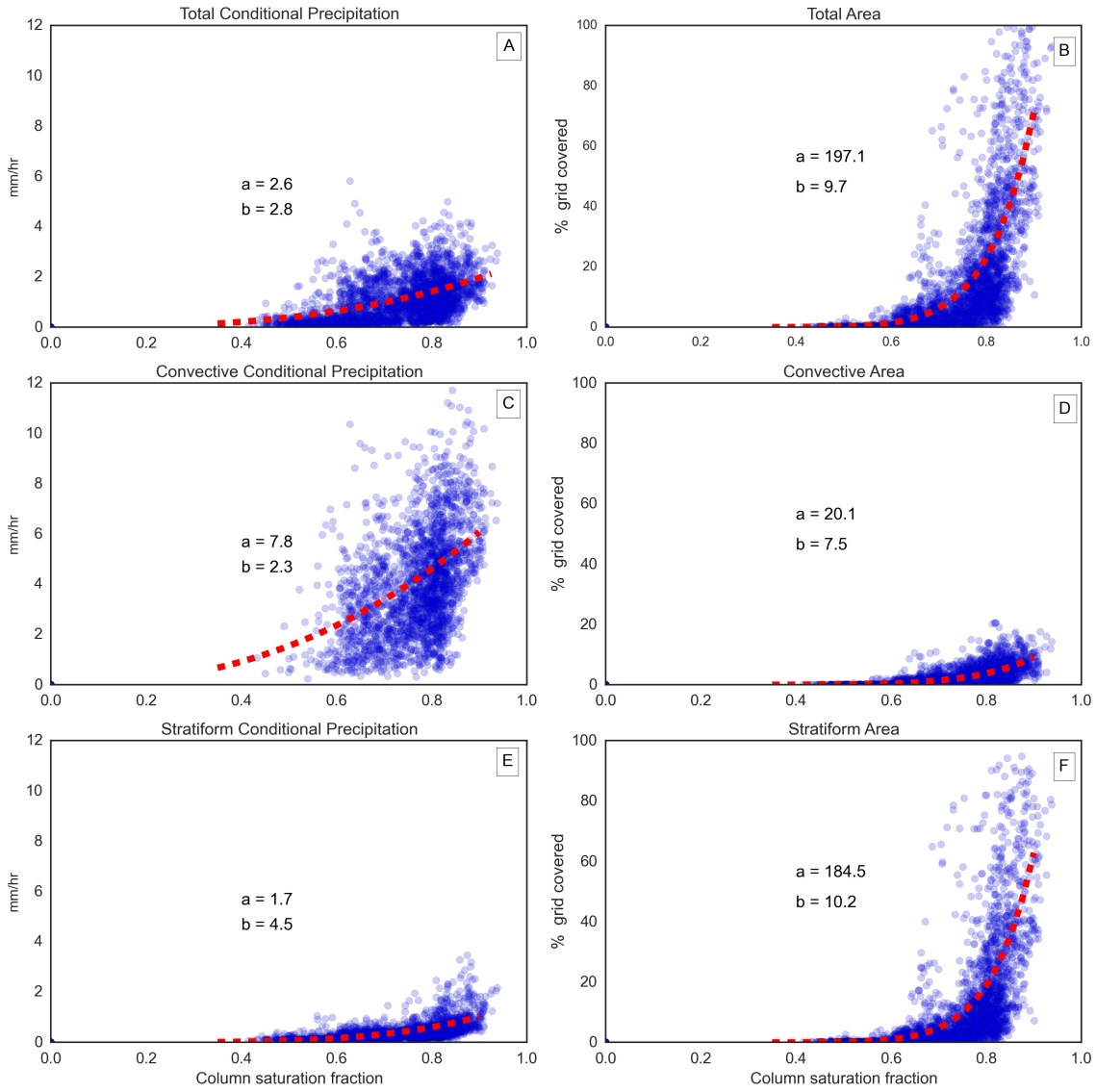

Figure 3.2: As in Figure 3.1 but for SMART-R hourly conditional rain rates and area coverage for (a, b) total, (c, d) convective, and (e, f) stratiform categories.

by stratiform and convective systems as shown by the difference in values between convective (20.1) and stratiform (184.5) rain. Since the area fraction is bounded at 100%, the interpretation of a is unphysical for stratiform and total radar area fraction. While the area fraction for stratiform rain can reach a high of around 60% in a radar domain of around 70,000 km2 (see Frederick and Schumacher (2008) Figure 6), the radar domain used in this case only includes the eastern half of the domain (see Figure 1 in DePasquale et al. (2014)). This truncated area explains why the entire domain can be almost completely covered with stratiform rain at high values of r (Figure 3.2f).

III.3.2 P-*r* relationships in satellite data

Figures 3.1 and 3.2, while instructive, only include observations for a radar-sized domain in the equatorial Indian Ocean for a 4 month period. To confirm if the aforementioned differences in convective and stratiform P-*r* relationships exist in a global, long-term data set, TRMM PR daily rainfall and MERRA daily moisture and temperature data were used for the four tropical ocean basins: the West Pacific (150°E-170°W), East Pacific (170°W-90°W), Indian (50°E-95°E), and Atlantic (50°W-20°W) Oceans. The latitudinal extent for this analysis was between 20°S and 20°N. The relationship between *r* and area-averaged rainfall for deep convective, stratiform, shallow, and total classifications was analyzed. These relationships are illustrated in Figure 3.3, where the TRMM domain-averaged precipitation values are binned by 1% *r* values, and the markers indicate the average precipitation in each bin, with the exception of the data in the last bin, which is the average of

all values above the grid label. The data for all the tropical ocean basins are also binned together and the corresponding power-law fit is obtained, which is indicated by dashed pale-green lines. The range of the bins is from 0 to 0.86, which was chosen to accommodate at least 2000 samples in each bin. It was crucial to retain an acceptable number of samples in the right tail of the histogram since the differences between convective and stratiform systems are particularly evident for extreme values of r. Figure 3.3a shows that the increase in total rainfall with r conforms to the previously known empirical relationship (Bretherton et al., 2004; Peters and Neelin, 2006) with a pickup in precipitation above r_c (0.7). Convective precipitation in every tropical oceanic basin shows a smooth but relatively shallow increase in the average precipitation beyond r_c (Figure 3.3b). Stratiform precipitation shows a rapid pickup in precipitation beyond r_c, with a b value of 11.3 (Figure 3.3c); this is higher than the b values for convective (7.6) or total (8.4) rainfall curves. Shallow precipitation is only weakly sensitive to an increase in environmental moisture and shows a more linear increase (b = 2.9). The a values indicate that the magnitude of stratiform area-averaged precipitation tends to be higher than convective precipitation for very moist columns.

Figures 3.4a, 3.4c, 3.4e, and 3.4g show the variation of the conditional rainfall with r. There are some differences between the oceanic basins on how the rainfall intensity is tied to r, but it is clear that the conditional rain rate in every category increases quasi-linearly with r, with b values between 1.1 and 3.4. These rain intensity curves are the subject of the subsequent chapter. Figures 3.4b, 3.4d, and 3.4f, however, show that rain area is highly

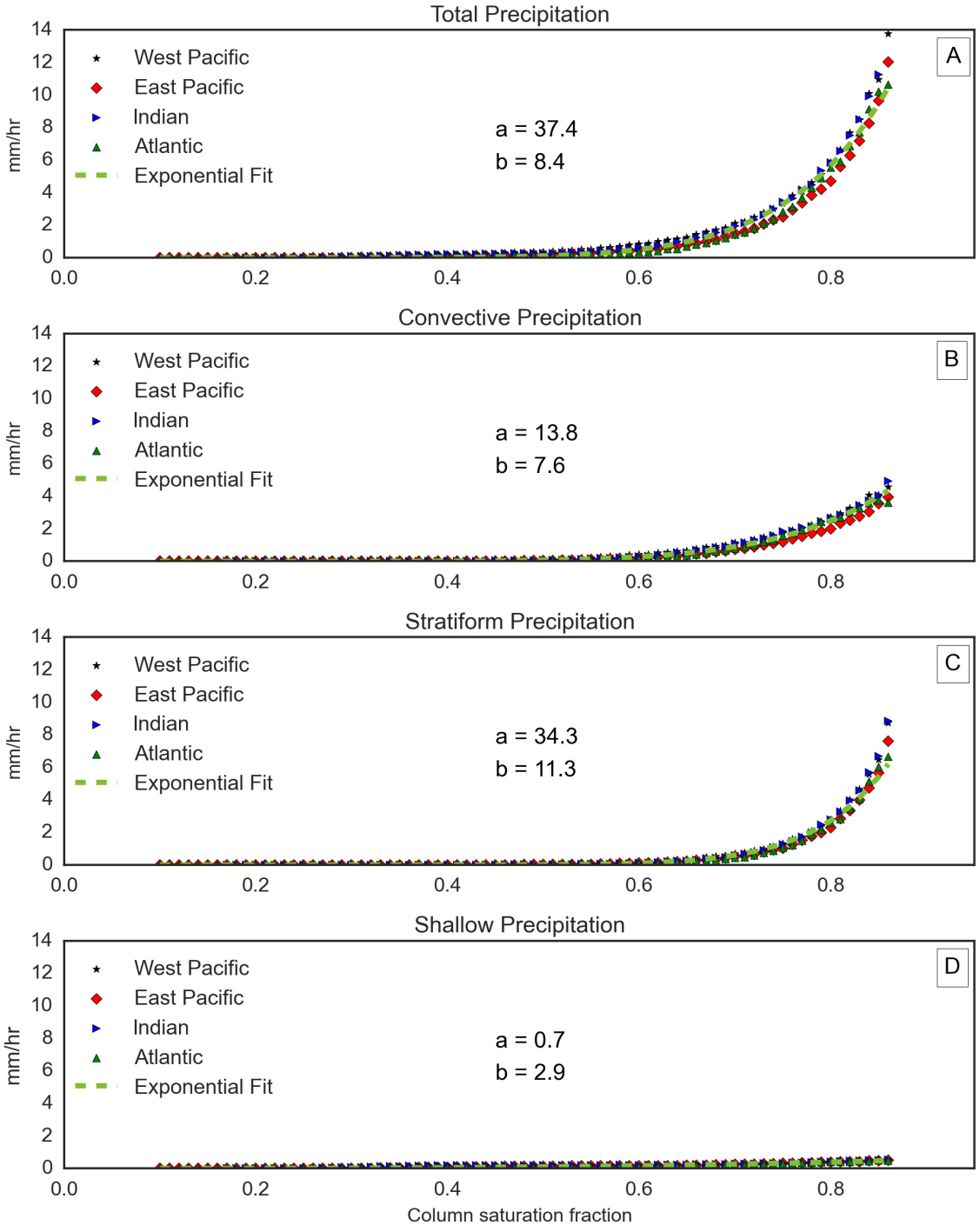

Figure 3.3: TRMM daily area-averaged rainfall for (a) total, (b) convective, (c) stratiform, and (d) shallow categories binned by 1% column saturation fraction for the four tropical oceanic basins.

nonlinear with increasing *r* (except for shallow rain) and describes the nonlinearity in the P-*r* curves in Figure 3.3. The differences between convective and stratiform categories are apparent in the rapidity of the pickup (*b* value of 6.37 versus 10.7). It is noted that the amount of the TRMM PR swath inside each 2.5°grid is highly variable on a daily time scale. Therefore, the extent of grid covered is obtained by dividing the number of pixels in each rain category by the total number of pixels observed by the PR (raining or non- raining) in the grid. The much larger area of the swath (about 3 times the size of SMART-R's eastern domain), along with the bin-averaged points shown in Figure 3.3, means that the extent of stratiform and convective rain areas are limited to about 25% and 5%, respectively.

Figure 3.5 shows the P-*r* curves for the monthly averaged values of precipitation (3.5a), conditional precipitation (3.5b) and rain area (3.5c) for total, convective, stratiform and shallow rain categories.The dashed lines in panels a and c are the fit lines to the power-law relationship. The parameters of the power-law fit–*a* and *b*–are given within parentheses in the legend. The overall trends for the monthly averaged values are the same as that for higher-resolution data: i.e. that stratiform rain picks up more sharply than convective and that the pickup is mostly due to an increase in rain area rather than rain intensity which does not show the canonical P-*r* curve. The sharpness of the pickup for all categories, however, is reduced–as seen from the smaller *b* values– when compared to daily and hourly averaged data and the differences between convective and stratiform are also smaller. These trends are not unexpected, given that intense precipitation events–which are represented in the long tail of the P-*r* curve–are more frequently sampled in a monthly average than on shorter

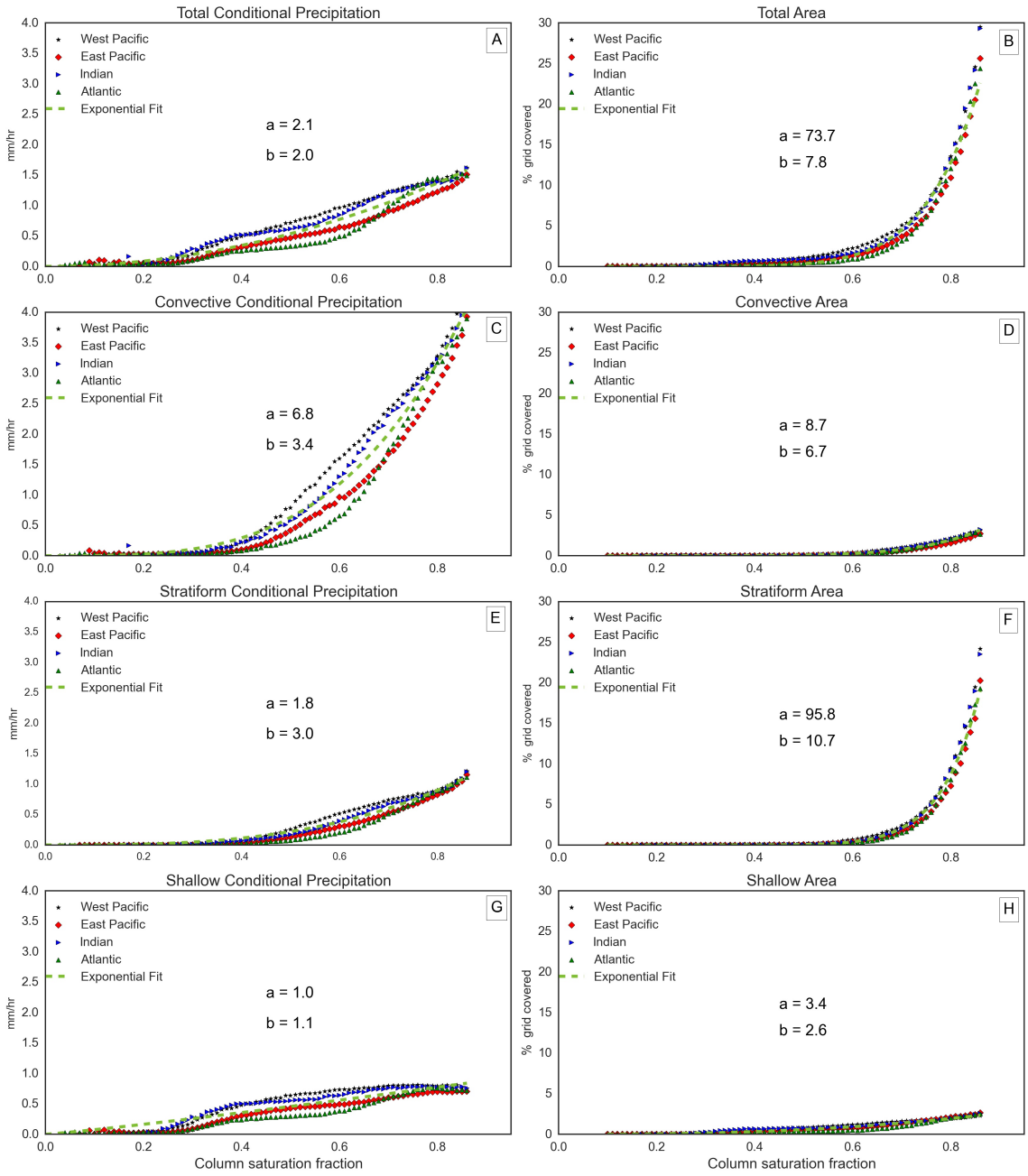

Figure 3.4: TRMM daily conditional rain rates and area coverage for (a, b) total, (c, d) convective, and (e, f) stratiform categories.

time-scales (Masunaga, 2012).

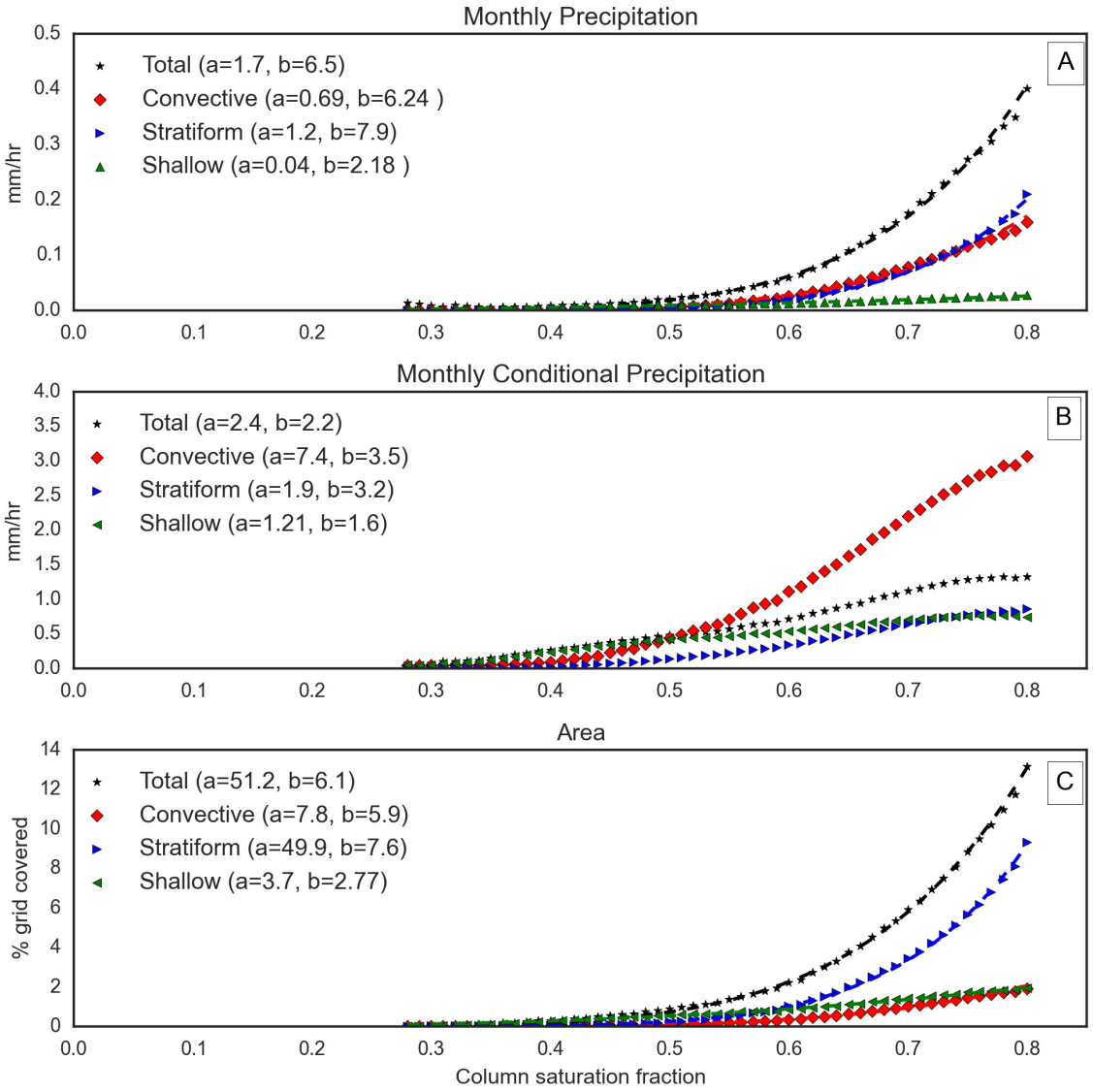

Figure 3.5: Monthly averaged values of a) domain-averaged precipitation b) conditional precipitation and c) % of rain cover in a grid from TRMM PR data, for different rain categories and all tropical ocean basins.

It would be valid to question whether the above trends in the P-*r* curve arise simply because of the differences in the magnitudes of convective and stratiform rain amounts

and area coverage. To address this concern, the analysis was repeated for all values of rain and area normalized by the mean value for each category and it was found that the exponent *b* of the power-law fit, does not change (not shown). However, there are changes in the parameter *a*, which is simply indicative of the fact that the normalized magnitudes of the curves are different from the non-normalized version. Thus, the differences in the pickup of the P-*r* curves are a property of the convecting systems, not merely an artifact of differences in the rain and area magnitudes.

Figure 3.6 shows the distribution of samples by the daily averaged *r* for each of the four tropical oceans in an 11 year period from 1998 to 2008 and for the TRMM classifications of total, convective, stratiform, and shallow rain. The sample distribution has interbasin differences that can be reconciled by considering the effects of sea surface temperature. As reported in Neelin et al. (2009) (see their Figure 8), warmer oceans have a single peak in the distribution closer to r_c, while cooler oceans possess a plateau owing to greater frequency of pixels occurring in the low *r* range in addition to the peak near the critical *r*. This is reflected in Figure 3.6a, where the warm Indian and West Pacific Oceans display a single peak, and the Eastern Pacific and Atlantic Oceans display a plateau and a peak. Figures 3.6b and 3.6c confirm that the incidence of convective and stratiform raining pixels increases with increasing column moisture for all tropical oceans, this number however drops precipitously beyond a certain value of *r*. Figure 3.6d reveals that the plateau from Figure 3.6a consists entirely of shallow pixels.

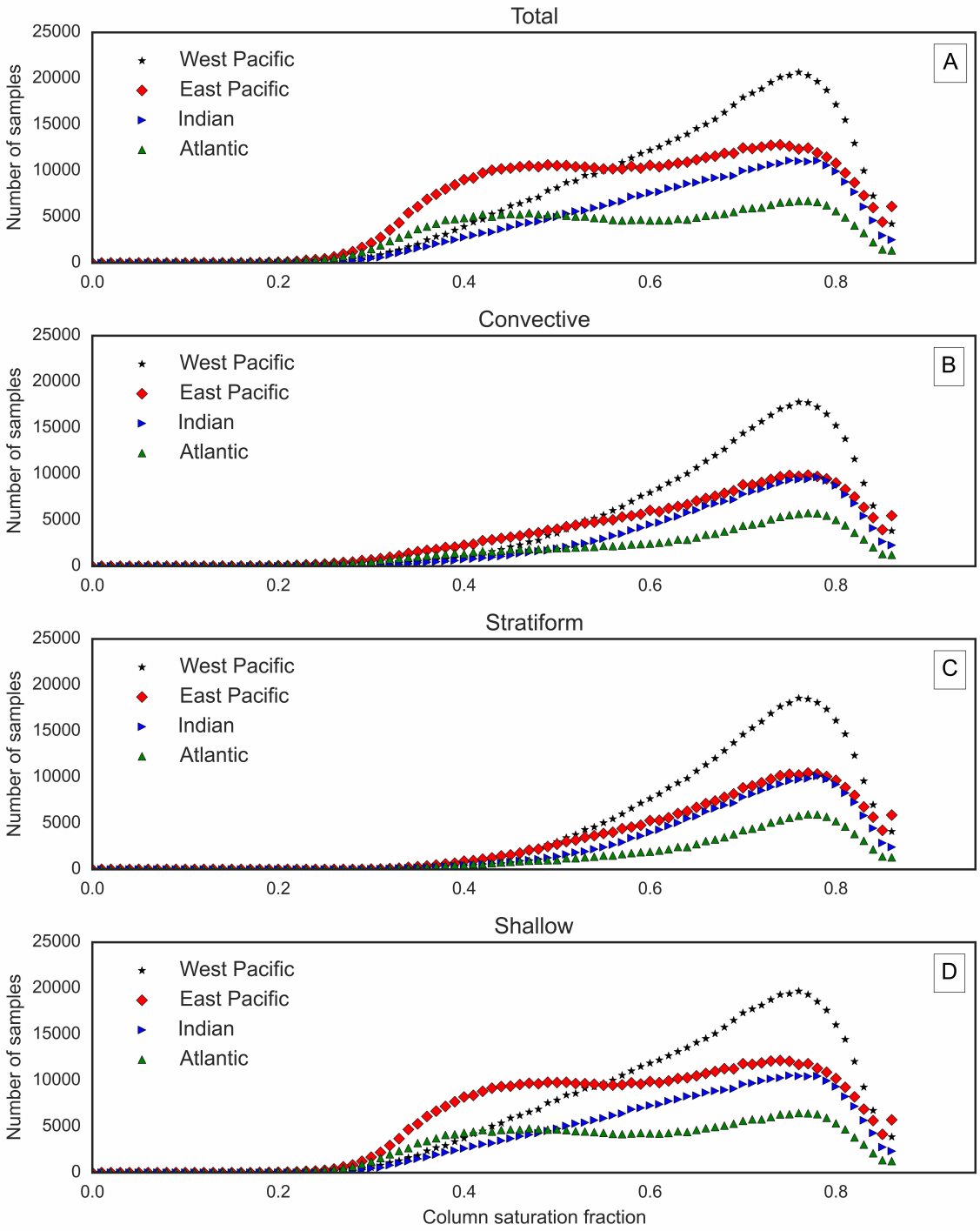

Figure 3.6: Distribution of daily averaged rain pixels, when binned by 1% column saturation values for (a) total, (b) convective, (c) stratiform, and (d) shallow rain types.

III.4 Discussion

III.4.1 Possible physical interpretation

The aggregation of cloud systems in the tropics up to and beyond the mesoscale has been extensively documented (Nakazawa, 1988; Mapes and Houze, 1992; Chen et al., 1996). Organization of convective systems is hypothesized to occur via gravity waves (Bretherton and Smolarkiewicz, 1989; Mapes, 1993; Liu and Moncrieff, 2004) and cold pool dynamics Khairoutdinov and Randall (2006); Tompkins (2001a). As reasoned from Figures 3.1 to 3.4, the nonlinearity in the P-*r* curve exists because of the nonlinear increase in the size of the precipitating systems. There are differences in the pickup between convective and stratiform raining areas, which can be attributed to the fact that while deep convective systems can exist as smaller isolated systems under conditions of relatively low r, significant stratiform rain over tropical oceans is more likely to be found in larger mesoscale convective systems (MCSs) (Rickenbach and Rutledge, 1998; Xu and Rutledge, 2015), which occur in more moist environments (Lucas et al., 2000; Tompkins, 2001b; Grabowski, 2003) .Therefore, the explosive increase for stratiform rain and the weaker increase for convective rain in the areal extent of convection are both indicative of the fact that MCSs are likely to form above the critical value of column moisture. The threshold for rapid increase in precipitation therefore appears to be a threshold for organization of precipitating systems over the tropical oceans. Previous studies have also reported the increased propensity for tropical convection to organize above the threshold *r* (Peters et al., 2009; Masunaga, 2012; Tan et al., 2013). However, the fact that larger precipitation systems can

act to moisten the surrounding atmosphere must also be borne in mind.

The observed near-linear increase in convective conditional rain rate with r, in both the ground radar and the satellite data (Figures 3.2b and 3.4b) can be explained by invoking the entraining plume model with linear mixing (Raymond and Blyth, 1986, 1992).As demonstrated in Holloway and Neelin (2009), an increase in environmental humidity increases the frequency of positively buoyant entraining plumes that translates into a greater frequency of convective clouds. The stratiform rain cloud then springs from a deep cumulonimbus cloud that ascends to the tropopause and laterally spreads its hydrometeors (see review in Houze (2004) for formation mechanisms) and completes the archetypal mesoscale convective system. It therefore stands to reason that intense convective rain will lead to intense stratiform rain. However, the MCS is also sustained by its own mesoscale dynamics:layer lifting and gravity wave dynamics triggered by convective heating (Moncrieff, 1992; Pandya and Durran, 1996), which under steady state conditions leads to the development of a midlevel inflow. The stratiform cloud ultimately also tends to dry the lower troposphere and moisten the upper troposphere (Zipser, 1977; Raymond et al., 2009) through mesoscale downdrafts and updrafts, respectively. The relationship between stratiform rain intensity and r is therefore also governed by the intensity the mesoscale dynamics–the midlevel inflow, the mesoscale updraft, and the mesoscale downdraft. Therefore, the linearity in the conditional P-r curves in Figures 3.2e and 3.4e is likely a consequence of a linear increase in both the intensity of the parent convective system and mesoscale dynamics.

III.4.2 Implications for parameterization schemes

Several studies have exploited the P-*r* curve in the construction and testing of cumulus parameterization schemes or diagnostic models (e.g., Sahany et al. (2012), Sahany et al. (2014)) ; Stechmann and Neelin (2011), Stechmann and Neelin (2014); Suhas and Zhang (2014)). The differences in convective and stratiform P-*r* relationships, however, suggests that different treatments for convective and stratiform regimes in cumulus parameterization implementation might be more realistic, examples of which include the multicloud parameterization(Khouider and Majda, 2006; Khouider et al., 2010) and the stochastic three-state model described in Stechmann and Neelin (2014) . The results of this paper also emphasize the requirement to parameterize the MCS to fully capture the effects of subgrid-scale convection (Del Genio, 2012), particularly the property of MCS organization.

III.4.3 Impact of measurement uncertainty

The main differences in the convective and stratiform precipitation-water vapor relationship emerge in the region of extreme *r* and precipitation rates, where instrument uncertainty is high. Compared to ground validation sites, TRMM PR retrievals perform better than TRMM Microwave Imager retrievals even if they underestimate extreme rainfall rates over the ocean (Wolff and Fisher, 2008). In comparing the MERRA and the Atmospheric Infrared Sounder (AIRS) data set, temperature values correspond well, but biases exist in the specific humidity values (Tian et al., 2013; Hearty et al., 2014). Specifically, the MERRA data set has a drier boundary layer and a wetter free troposphere in the tropics

when compared to the AIRS products. These uncertainties are not expected to change the qualitative nature of our studies since column integrated water vapor values are not made use of in this analysis. The metric of column moisture content is the column saturation fraction in this study.Gilmore (2015) showed that precipitation variance is highly sensitive to measurement uncertainties in precipitation and column water vapor retrievals; variance statistics, therefore, are not presented in this study.

III.5 Summary

The tropical oceanic precipitation-column moisture relationship, reported in previous studies, was separated into its convective and stratiform components using radar observations from the DYNAMO field campaign and TRMM satellite, and corresponding moisture information obtained from the DYNAMO radiosondes and MERRA. It was found that the strong increase in area-averaged precipitation beyond the critical column moisture value is characteristic of stratiform rain much more so than convective rain, which displays a weaker nonlinear relationship. It was also shown that the nonlinearity in both convective and stratiform systems derives mostly from the nonlinear increase in the area of precipitation. This trend is observed over all tropical oceanic basins and at instantaneous, hourly, and monthly time scales. Differences in the degree of nonlinearity can then be in part attributed to the fact that tropical stratiform rain regions are found almost exclusively in MCSs, whereas convective cells can be found both within and outside of MCSs. This finding offers an additional constraint in parameterization validation and comparison stud-

ies. It also stresses the need for a synergistic treatment of both convective and stratiform components of tropical rainfall in convective parameterization schemes in the form of a parameterization of MCS dynamics to realistically model subgrid-scale convection.

CHAPTER IV

GEOGRAPHICAL VARIATIONS IN THE TROPICAL PRECIPITATION COLUMN MOISTURE RELATIONSHIP

IV.1 Background

The previous chapter introduced the tropical P-*r* curve and then explored the different components of tropical precipitation and its relationship to moisture. In this chapter other features of the P-*r* curve will be investigated, particularly quantifying the threshold as well as extending the analysis to tropical land. As stated previously, the tropical precipitation - column water vapor curve (the P-*r* curve) relates the grid-averaged precipitation to the amount of column moisture atop the grid (Bretherton et al., 2004) and is characterized by a sharp pickup in precipitation above a threshold value of column moisture. Environmental instability and entrainment can be argued to be the principal mechanism that shapes the existence of the pickup threshold; at the smallest time and space scales, entraining plumes rising out of the boundary layer remain buoyant throughout the depth of the atmosphere beyond a critical value of column moisture (Holloway and Neelin, 2009). As the depth and the number of the buoyant plumes increases, convective clouds beget stratiform clouds (Houze, 2004) by detraining hydrometeors and via other mechanisms of convective organization (Mapes, 1993; Pandya and Durran, 1996). Stratiform rain is therefore close to non-existent for moisture values below the threshold and is abundant above it, exhibiting a sharper pickup than convective rain (Ahmed and Schumacher, 2015). The P-*r* curve is

also dependent on the time and space scales of analysis with sharper (smoother) curves for higher (lower) space and time resolutions (Schiro et al., 2016).

The P-*r* curve has been used to demonstrate the stochastic nature of tropical convection. Analytically reproducing the P-*r* curve involves the assumption of a moisture trigger–representing the threshold—for the precipitation onset and a stochastic source of column moisture (Muller and Held, 2012; Stechmann and Neelin, 2011; Hottovy and Stechmann, 2015). The statistics of the system near onset have also been explored analogously with other stochastic systems (Stechmann and Neelin, 2014) including dynamical systems exhibiting self-organized criticality (Peters and Neelin, 2006; Peters et al., 2009). Several works have utilized the observed pickup in the P-*r* curve as means to estimate the convective moisture-adjustment time scale (Bretherton et al., 2004), to constrain entrainment (Sahany et al., 2012), and to trigger convection–stochastically or deterministically–in cumulus parameterization schemes (Stechmann and Neelin, 2011; Suhas and Zhang, 2014). There is also potential utility in using the convective and stratiform section of the P-*r* curve as a way to parameterize organized convection in the tropics.

Given the various uses of the canonical tropical P-*r* curve, it is noteworthy that the pickup is not universal: (Neelin et al., 2008, 2009) identified the tropospheric temperature dependence for the pickup threshold over the Western and Eastern Pacific Oceans, while Bergemann and Jakob (2016) showed that tropical coastal precipitation, in contrast to oceanic precipitation, does not pickup rapidly with *r*. It is important, therefore, to get a complete picture of the geographical range of variations in the P-*r* curve. To this end, a

survey of the P-*r* relationship across tropical land and ocean is presented. The nature of the relationship between rain intensity and large-scale moisture that was mentioned in the previous chapter is also expanded upon, thus providing a new statistical relationship that could be used to discern the links between convection and the environment in the tropics.

IV.2 Data and methodology

In this study, 17 years (1998-2014) of precipitation information from the Tropical Rainfall Measuring Mission (TRMM) Precipitation Radar (PR) observations were used, building on the 11 years used in the previous chapter. As before, individual pixels representing footprints on the order of 5 km were separated into convective, stratiform and shallow rain categories using the 2A23 algorithm (Awaka et al., 1997, 2007; Funk et al., 2013); this algorithm uses the vertical information of the reflectivity structure alongside the horizontal texture-based algorithm of Steiner et al. (1995). All pixels with an 18 dBz (i.e., the sensitivity of the TRMM PR) echo-top height less than 1.5 km below the melting level are classified as shallow. Daily files of TRMM PR precipitation are gridded onto a 2.5 x 2.5 degree resolution as before. Conditional rain–used interchangeably with rain intensity–is defined as the rain amount normalized by the number of raining pixels. This measure is produced for the convective, stratiform and shallow categories. The rain area is computed as a fraction of the grid covered by rain, defined as the number of raining pixels in a grid divided by the size of the satellite swath inside the grid.

In contrast to the previous chapter, where MERRA data was used, here specific hu-

midity and temperature were obtained for the concurrent period (i.e., 1998-2014) from ERA-I. Column saturation fraction, r is defined as before:

$$r = \frac{< q >}{< q* >} \tag{IV.1}$$

where q and q* are the specific humidity and the saturation specific humidity with respect to liquid water respectively; < > refers to the mass weighted vertical integration in the troposphere from 1000 mb to 100 mb. The 6-hourly ERAI values are averaged daily and produced for the same 2.5 x 2.5 degree grid as the TRMM PR rainfall data. The results of this study are presented using *r* as a measure of the column moisture content and they qualitatively hold true even if column integrated water vapor–<q>– is used instead.

In the previous chapter, it was shown that the exponential pickup in the tropical oceanic P-*r* curve is primarily due to a pickup in the size of the raining system rather than its intensity. Here, a more quantitative approach is adopted to look at the geographical variations in the shape of the P-*r* curve and the relationship between the intensity of rainfall and *r*. The pickup threshold (r_t), or the value of *r* at which the P-*r* curve displays a rapid increase in precipitation with *r*, is defined as the value of *r* for which the area bounded by the corresponding bin is closest to 10% of the area bounded by the last bin. This 10% threshold identifies points that are visually the points beyond which the precipitation takes off. The robustness of this measure has been tested on all the P-*r* curves shown in this chapter. Other thresholds (for e.g. 50%) can be used but they do not identity points that are intuitively the pickup thresholds.

Consider a variable *v* that exhibits a non-linear relationship with *r*. A function F(r)

can be defined where:

$$\left| \int_{r}^{r+\Delta r} v dr - 0.1 \int_{r_l}^{r_l+\Delta r} v dr \right| \tag{IV.2}$$

Then r_t is computed by minimizing $F(r)$:

$$F(r_t) = min(F(r)) \tag{IV.3}$$

Δr is the bin interval–2.5% in this case–and $r_l + \Delta r$ is the lower bound of the last bin in the given $v - r$ curve. As will be shown in the next section, this definition of r_t can identify the pickup threshold for any P-r curve. When the variable in question follows the power law curve $P = ar^b$, it can be shown that the pickup threshold r_t is non-linearly related to the parameter b. The area under the curve between points r and $r + \Delta r$ is obtained after integrating the power law curve as $ar^{b+1}\Big|_{r}^{r+\Delta r}$ .The ratio of the areas confined between points r and $r + \Delta r$ and that between r_l and $r_l + \Delta r$–where $r_l + \Delta r$ is the last bin–is then given by:

$$F(r) = \frac{ar^{b+1}\Big|_{r}^{r+\Delta r}}{ar^{b+1}\Big|_{r_l}^{r_l+\Delta r_l}} \tag{IV.4}$$

After expanding using the binomial series and neglecting the higher powers $\frac{\Delta r}{r}$, IV.4 can reduced to:

$$F(r) = \left(\frac{r}{r_l}\right)^b \left(\frac{1 + \frac{\Delta r}{r}(b+1)}{1 + \frac{\Delta r}{r_l}(b+1)}\right) \tag{IV.5}$$

For a given bin resolution Δr and r_l, r_t is the value of r for which $F(r)$ is closest to the assumed threshold (0.01 in this case). Even though r_t and b are mathematically related in this case, they refer to different physical characteristics: the former is the minimum amount of moisture required to trigger convection and the latter is the shape of the precipitation increase once triggered. These parameters have potential utility in representing different types of convection over land or ocean–either analytically or in cumulus parameterizations. The exponent b (when greater than one) is a measure of the strength of the pickup of the P-r curve, as demonstrated in chapter III. One advantage of using an area-based threshold is that an r_t value can be identified even for curves with different power law forms (e.g., Figure 4.1).

IV.3 Results

The tropical P-r curves over land are now presented and compared with the curves over the ocean (Figure 4.2).The five land regions are: India (61.25°E–91.25°E; 10°N–25°N), the Maritime Continent (MC) (91.25°E–153.75°E; 11.25°S–11.25°N), Australia (91.25°E–153.75°E; 33.75°S–11.25°S), the Americas (106.25°W–33.75°W; 25°N–25°S) and Africa (18.75°W–61.25°E; 25°N–25°S). Only the land regions within these bounds were utilized for analysis. These broad regions may mute some of the strong seasonal variations and different dynamical regimes that can characterize continental convection (Petersen and Rutledge, 2001; Xu and Zipser, 2012), but they are retained to highlight some basic differences between land and ocean P-r curves. The four ocean regions are

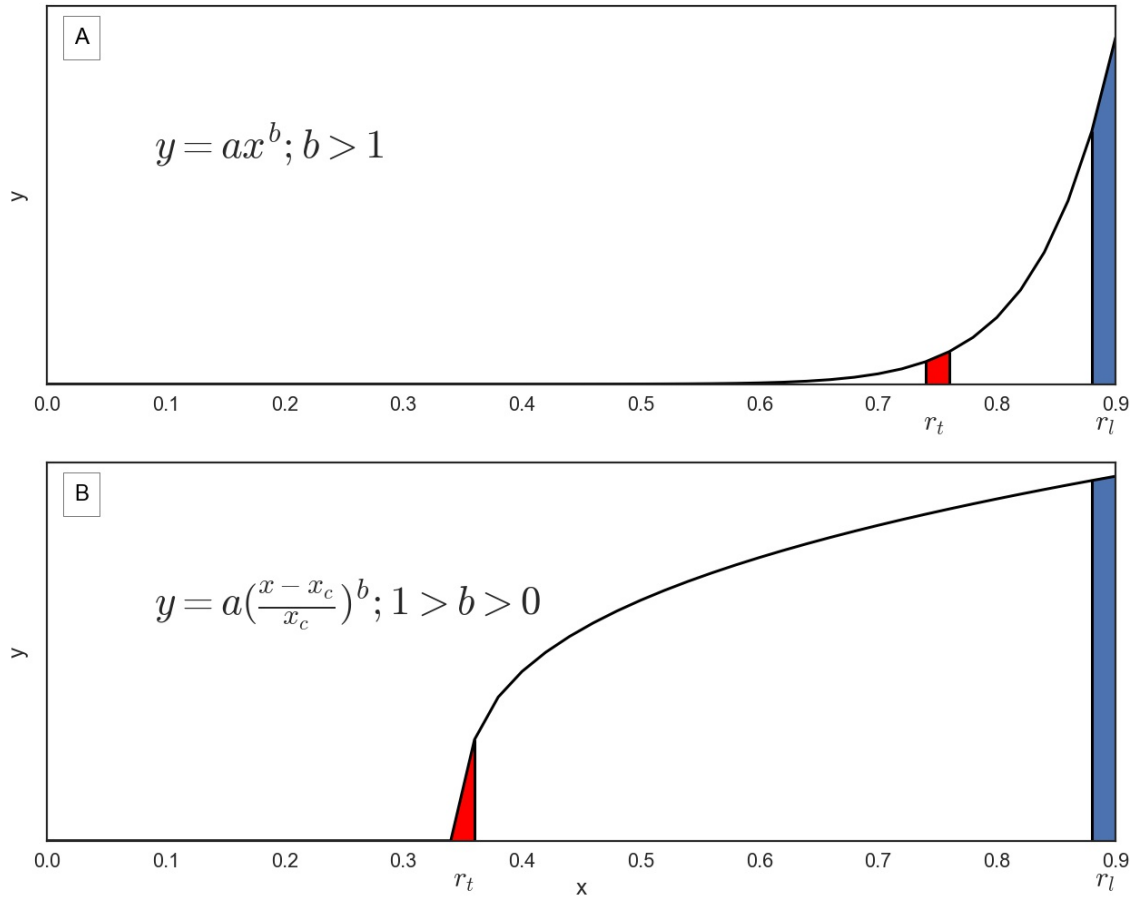

Figure 4.1: Determining the pickup threshold for two example P-*r* curves. a) A concave upward P-*r* curve typical of the curves presented in this study, b) a concave downward precipitation-moisture curve typical of oceanic shallow convection. The region which is shaded blue, is the area under the last bin of the P-*r* curve; the red-shaded region is the area which is closes to an assumed threshold value of the blue area (10 % in this case).

the same as in Chapter III and have latitudinal bounds between 22.5°N–22.5°S and longitudinal bounds as follows: Indian Ocean (33.75°E–108.75°E), Western Pacific Ocean (111.25°E–166.25°W), Eastern Pacific Ocean (163.75°W–71.25°W) and Atlantic Ocean (68.75°W–16.25°E).The ocean panels on the right side of Figure 4.2 are similar to Figure 3.3, but are zoomed in and include the r_t values for each curve. The r_t values for each

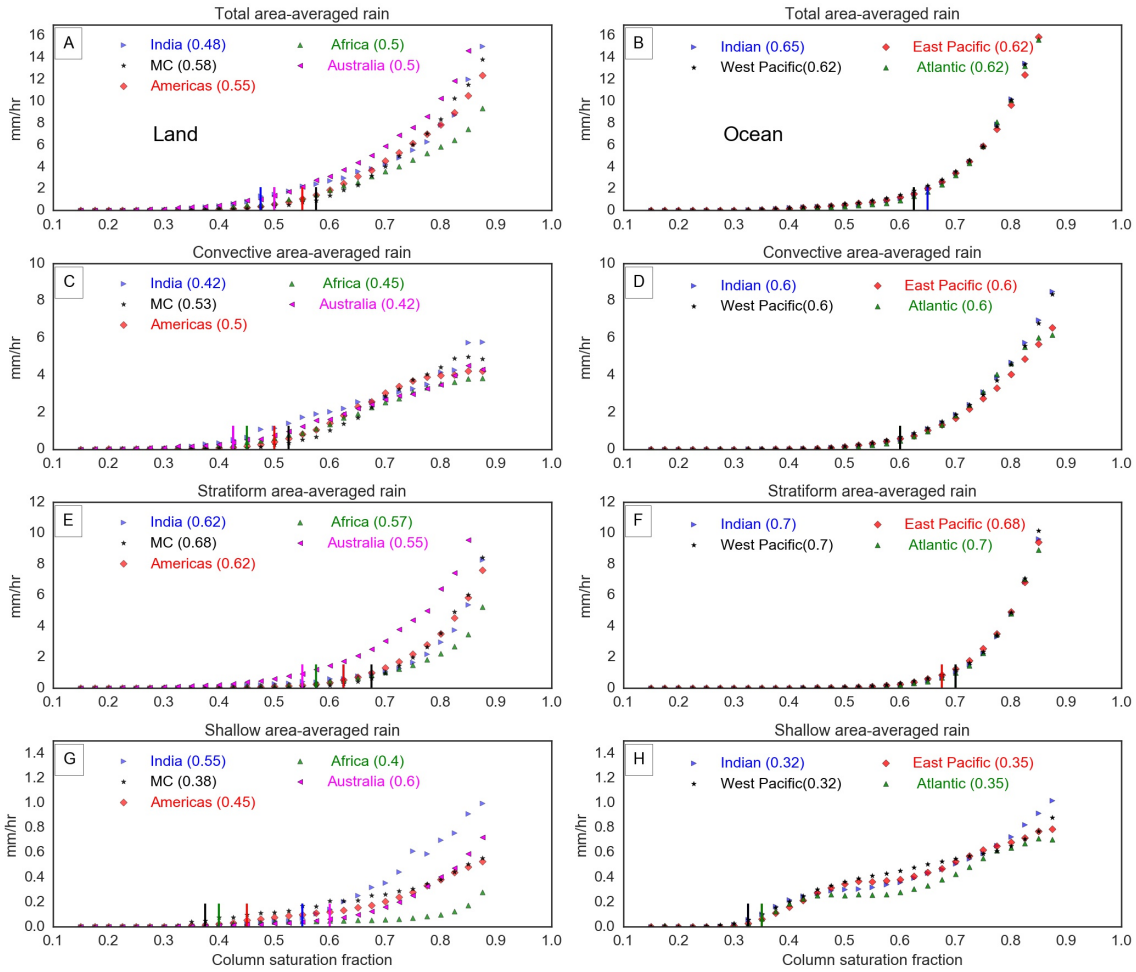

Figure 4.2: TRMM PR area-averaged rain versus column saturation fraction for a,b) total, c,d) convective, e,f) stratiform and g,h) shallow categories over a,c,e,g) land and b,d,f,h) ocean. The curves are computed from daily data and rainfall values were binned by r values in increments of 2.5%.The numbers in the parentheses indicate the r threshold at which the curves pickup (r_t).

region are also marked by small vertical lines.

Figures 4.2a and b show that the total grid-averaged rain picks up for lower r over land (~0.5) than ocean (> 0.6). Similar to the P-r curves over ocean, convective rain (Figure 4.2c) picks up before stratiform rain (4.2e) over land, but at lower r_t values for each rain type compared to ocean (cf. Figures 4.2c and d for convective rain and Figures 4.2e and f for stratiform rain). While the shallow rain pickup over land (Figure 4.2g) is similar to the convective rain pickup, the shallow rain over ocean picks up before convective rain (Figure 4.2h), flattens and increases again with the convective rain pickup. The pickup at low values of r in the oceanic shallow rain curves is explained by the prevalence of shallow isolated rainfall over ocean (Schumacher and Houze, 2003; Chen and Liu, 2016).The shallow convection over land is dominated by the shallow non-isolated category, which is attached to deep convection (Funk et al., 2013). This difference is discussed in a figure later on. The pickup threshold identification method outlined above yields r_t values for curves that clearly follow a power law curve with b > 1 (e.g., Figures 4.2e and f) as well as curves that are not well approximated by the power law (e.g., Figures 4.2g and h).

The land P-r curves in Figure 4.2 also exhibit greater geographical variation than their oceanic counterparts. In order to elucidate the geographical dependence of the P-r curve, a map of the pickup threshold (r_t) for the different components of tropical precipitation is constructed and shown in Figure 4.3. To ensure that adequate samples were present for each region, the tropics were divided into three latitudinal and 18 longitudinal zones; only grids with a daily mean rainfall of 10 mm/day or larger were analyzed. The resolution of

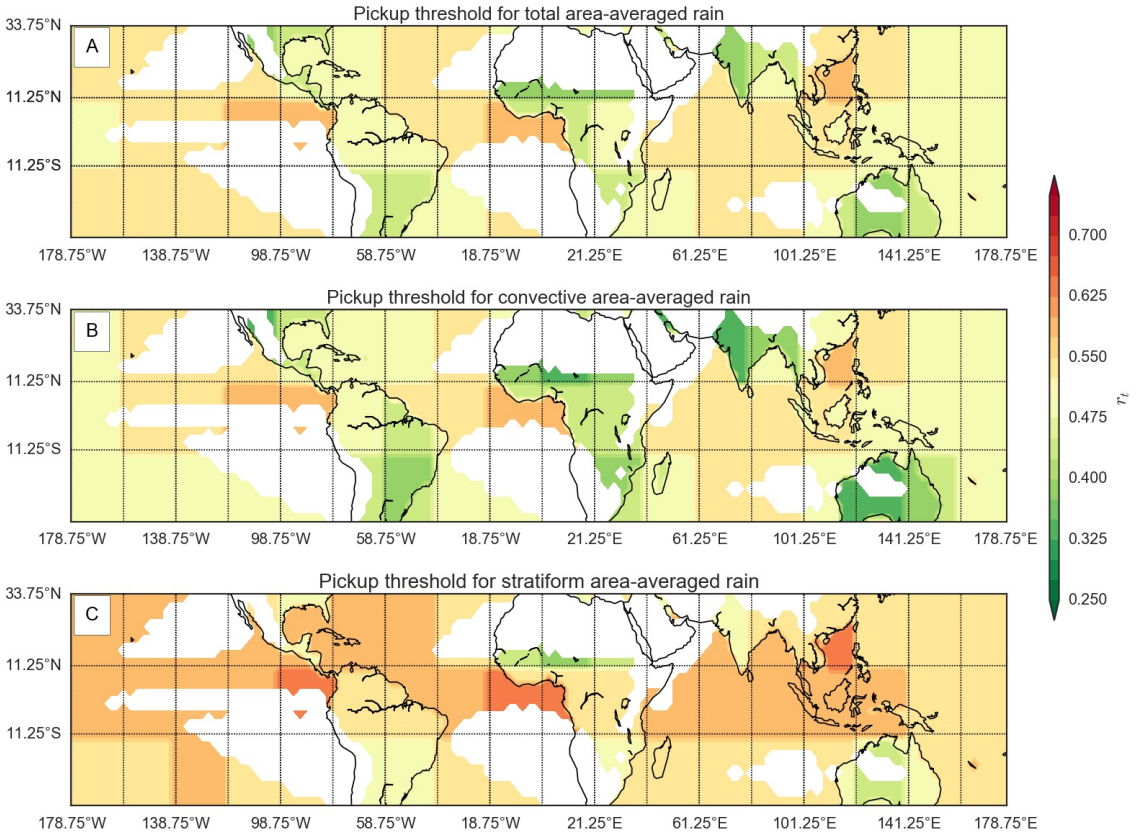

Figure 4.3: The pickup threshold (r_t) for P-r curves across the tropics for a) total, b) convective, c) stratiform rain types. Regions with daily average rainfall less than 10 mm/day were excluded from analysis.

the binning was also coarsened to 5% to ensure the presence of adequate samples in each bin. Land and ocean points inside each zone were separated because they have different characteristics. Figure 4.3a confirms that the total area-averaged rain picks up for lower values of r over land than over the oceans. It also shows that r_t is higher over the Amazon and Maritime Continent than other land locations, consistent with observations that the convection in these regions is more oceanic in nature (Cifelli et al., 2002; Romatschke and Houze, 2010; Williams et al., 2002). The eastern edge of the Atlantic Ocean and the northern part of the South China Sea have prominently high r_t values, indicating that the large-scale saturation has to be high (beyond 0.65) in these regions before precipitation can pick up.When separated into convective and stratiform components (Figures 4.3b and 4.3c), the convective rain pickup occurs before the stratiform rain pickup over both land and ocean, consistent with the P-r curves in Figure 4.2. Stratiform rain, however, generally shows less variation in r_t over the ocean suggesting that there might exist a near-universal r_t for the pickup in organized convection over tropical oceans. The total and convective maps (Figures 4.3a and 4.3b) look similar because the earlier convective pickup dictates the timing of the total rain pickup; however, there are other aspects of the P-r curve to consider.

Even though the rapidity b can uniquely determine r_t if the curves are approximated by the power-law fit, these two mathematically related quantities have different physical meanings, which could be of special importance when designing a parameterization scheme for instance. Physically, r_t represents the minimum amount of moisture in the at-

mosphere that facilitates the transition between a non-precipitating and a strongly precipitating atmosphere, whereas *b* is the shape of the precipitation increase once precipitation picks up. To therefore get a more comprehensive picture of the global variations in the P-*r* relationships, the global variations in the sharpness of the pickup are shown in Figure 4.4. The pickup is less rapid over land than over ocean (Figure 4.3a) with the most rapid pickup occurring over the eastern side of the Atlantic and Pacific oceans and the northern part of the South China Sea–places recognized as possessing high r_t values from Figure 4.3. Pickups are much weaker over southern South America, Africa, the Indian subcontinent, and central Australia. Much of the land signal in Figure 4.4a is dictated by the b values for convective rain (Figure 4.4b). Even the more oceanic Amazon has a less rapid pickup in convective rain than the oceans. Figure 4.4c shows that the stratiform rain everywhere picks up more rapidly than the convective rain.Further, both convective and stratiform rain production influences the geographical variation in the rapidity of precipitation pickup in Figure 4.4a.

Finally, the P-*r* curves over tropical land are separated into conditional rain and rain area in Figure 4.5. Figures 4.5a and 4.5b show that the total conditional rain has smaller r_t than rain area. This is true for both convective and stratiform categories. Figures 4.5c and 4.5d show that the convective conditional rain (r_t values between 0.32 and 0.42) picks up before convective area (r_t between 0.42 and 0.53). The same feature is also evident for the stratiform category (Figures 4.5e and 4.5f) where rain area picks up for r_t values between 0.52 and 0.65, higher than for corresponding values for stratiform conditional rain

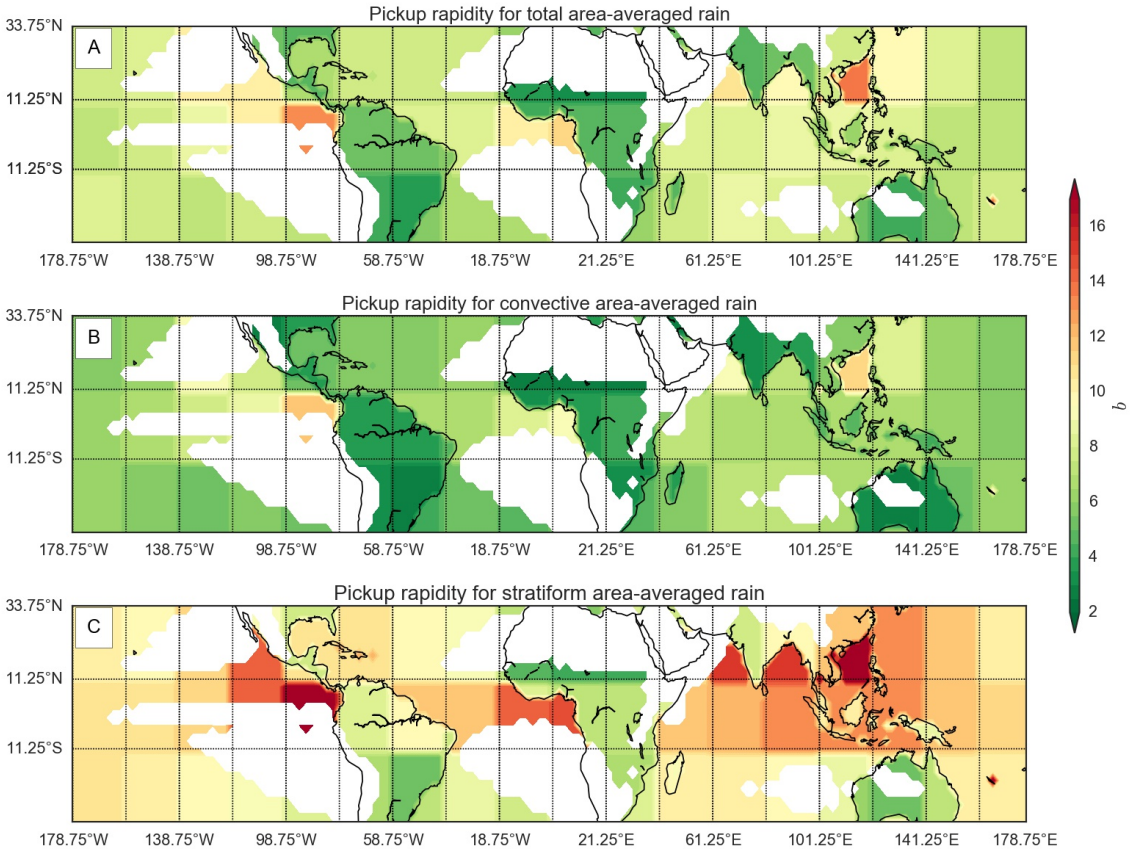

Figure 4.4: As in Figure 4.3 , but for the rapidity of pickup (*b*) in the P-*r* curves.

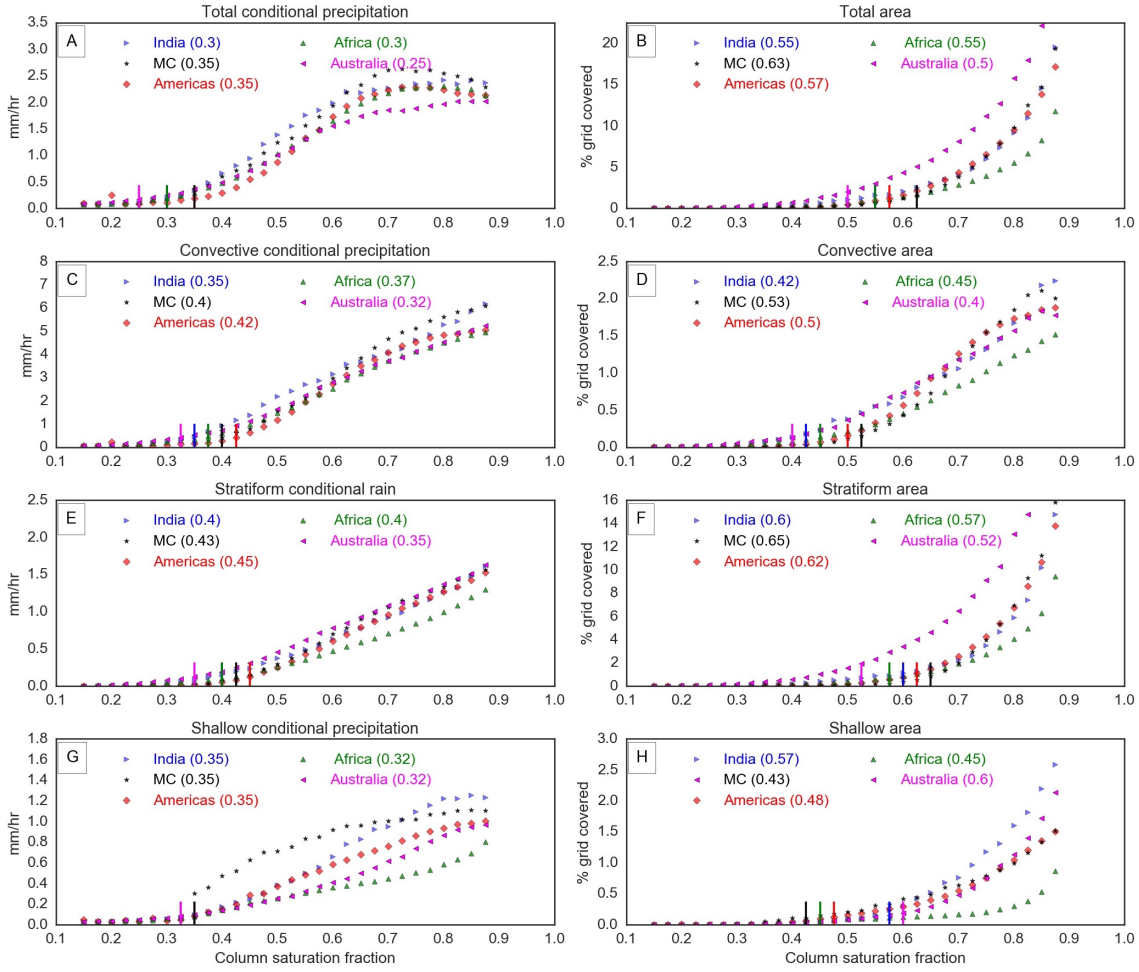

Figure 4.5: As in Figure 4.2,but for TRMM PR conditional rain rates and rain area coverage for a,b) total, c,d) convective, e,f) stratiform and g,h) shallow categories over tropical land.

(r_t between 0.35 and 0.45). The shallow conditional rain and shallow area curves (Figures 4.5g and 4.5h) fall somewhere between the convective and stratiform curves because most of the shallow rain over land is connected to deeper clouds (Figure 4.6). In addition, there is a slight separation between the r_t values for convective and stratiform area (Figures 4.5d and 4.5f), with the convective rain area picking up at lower r values. However, Figure 4.5 shows that the importance of the exponential pick up in stratiform rain area to the overall P-r curve shape over tropical oceans holds over tropical land as well. The conditional rain curves also appear quasi-linear with smaller b values between 2 and 4.

The relationship between shallow precipitation–which according to TRMM is precipitation with an echotop height less than 1.5 km below the melting level–and r is now discussed. In Figure 4.6, it is seen that the relationship between the different components of shallow rain–isolated and non-isolated (Funk et al., 2013)–and r varies over land and ocean. Shallow isolated rain–mostly present over tropical ocean–shows very low values over land (Figure 4.6 a) and no consistent relationship with r. Over the ocean, shallow isolated rain picks up rapidly around an r value of 0.3 and exhibits a pronounced peak near 0.45 (Figure 4.6 b), beyond which it actually decreases with increasing r, suggesting a demise in the non-organized form of shallow convection. Shallow non-isolated convection occurs in association with deep convection and has consequently has a higher pickup threshold and a more power-law like appearance (Figures 4.6 c & d). The shallow non-isolated rain appears to pickup for lower r values over the ocean than over land. Though the overall contribution of shallow systems to either total rain area or intensity is small, the

shallow convection–r relationship over the oceans highlights the long-recognized ubiquity of shallow convection over the tropical ocean as r values rarely fall below 0.3 in these regions.

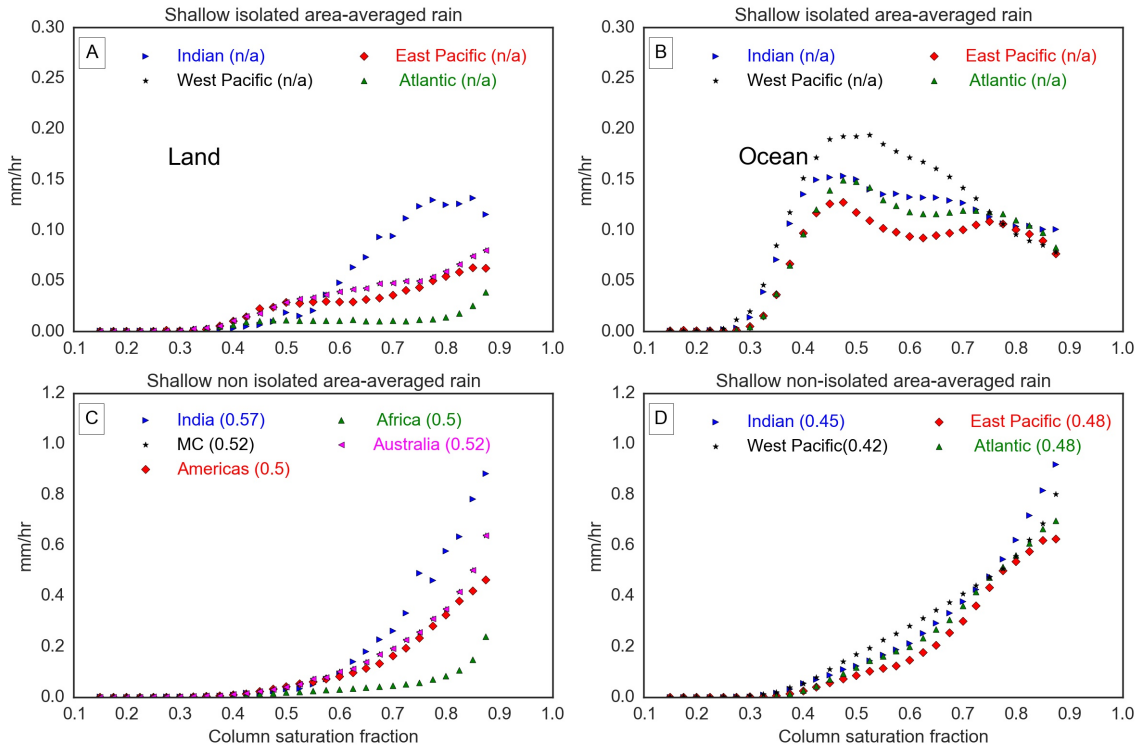

Figure 4.6: Shallow isolated area-averaged rain (a,b) and shallow non-isolated area-averaged rain (c,d) for tropical land (a,c) and tropical ocean (b,d).

The early pickup for conditional rainfall noted in Figure 4.5 also exists over the tropical ocean. Table 4.1 lists the r_t values for the four tropical ocean basins. The P-r curves for these regions are also shown in Figure 4.2. Table 4.1 shows that conditional rain picks up prior to rain area in all three categories (i.e., total, convective and stratiform) for all the tropical ocean basins. The total rain intensity picks up in very dry conditions (~0.3) compared to the total rain area (~0.68) because of the pickup in shallow isolated rain intensity

Table 4.1: The pickup thresholds (r_t) for the four tropical oceans separated by conditional rain and rain area. IO: Indian Ocean; WP: West Pacific; EP: East Pacific; AT: Atlantic

Rain Categories	Area averaged rain				Conditional rain				Rain area			
	IO	**WP**	**EP**	**AT**	**IO**	**WP**	**EP**	**AT**	**IO**	**WP**	**EP**	**AT**
Total	0.65	0.62	0.62	0.62	0.3	0.3	0.32	0.32	0.68	0.68	0.68	0.68
Convective	0.6	0.6	0.6	0.6	0.45	0.42	0.48	0.48	0.6	0.57	0.6	0.57
Stratiform	0.7	0.7	0.68	0.7	0.45	0.42	0.45	0.48	0.7	0.7	0.7	0.7

(Figure 4.5b). Convective and stratiform rain intensity over the oceans picks up around the same r value (0.45), which is lower than the pickup for their respective rain areas: ~0.6 for convective and ~0.7 for stratiform. The area-averaged precipitation picks up close to the r_t values for rain area, which implies greater contribution from the rain area than intensity to the domain-averaged precipitation values. These r_t values confirm that the trends seen over tropical land–a separate pickup for conditional rain and convective and stratiform rain area–are also observed for tropical oceanic regions.

IV.4 Discussion

IV.4.1 Land-ocean differences and geographical variability

The major differences in the characteristics of the P-*r* curve over land and ocean are the lower r_t values and a weaker pickup (lower *b* values). As explained in the Background section, the value of *b* is to some extent controlled by environmental instability but is also affected by the time and space scales of the analysis. Lower values of *b* over land could arise from mechanisms that help trigger convection at lower values of *r* over land than

over ocean–particularly the land surface warming that can overcome convective inhibition (CIN) (Fu et al., 1999; Qian, 2008) or topographic forcings (Smith et al., 2009; Kirshbaum and Smith, 2009) that are absent over the ocean. The tropical ocean also possesses a layer of enhanced stability near the melting level (Johnson et al., 1996; Posselt et al., 2008), which could inhibit deep convection and thus require additional moistening near the cloud tops of congestus clouds to facilitate a transition to deep convection. These factors may also contribute to the appearance of organized convective clouds and subsequent stratiform clouds at lower r values over land than over the ocean and therefore change the nature of the land P-r curve–making it pick up less rapidly. It is also likely that the coarse resolution of our analysis–2.5 degree grid and daily averaged–smooths over the presence of intense convection over land. Oceanic convection–particularly stratiform rain from deep convection–can be widespread and long-lived (Schumacher and Houze, 2003) and would be less affected by the resolution of the analysis. However, continental convection over the Amazon as seen from near-instantaneous time and point measurements exhibits a sharp pickup (Schiro et al., 2016) so a more definitive explanation for the cause of the land ocean differences in the P-r curve will require a survey of high-resolution measurements from across the tropical world and is presently beyond the scope of this satellite-based study. Aside from these broad differences, there are also interesting geographical variations in the P-r curve characteristics amongst different land and ocean regions. Most prominently, it is clear that the islands of the Maritime Continent and parts of the Amazon have r_t values that are close to oceanic values. Among the ocean basins, the eastern Pacific and Atlantic

Oceans–both located in the descending branch of the Walker circulation–have a steeper pickup for both convective and stratiform rain than the rest of the oceans–this reinforces the earlier speculation that the pickup values are considerably higher over regions with greater stability to rising motion. A higher r_t–and therefore a steeper pickup– is also observed over the northern part of the South China Sea, which is a region marked by weak instability (Johnson et al., 2005) and might therefore require higher values of large-scale saturation before rain area–both convective and stratiform–can pickup.

The extensive presence of shallow-isolated rain over the oceans is evident in the association of shallow rain with low r_t; the presence of non-isolated shallow rain over land, mostly found in conjunction with organized deep convection, explains the higher r_t values for shallow convection over land. The absence of a shallow pickup prior to deep convective pickup over land indicates that the shallow-to-deep transition happens much faster and does not organize independent of deep convection over land, unlike over the ocean.

IV.4.2 Why does rain intensity pickup at lower *r* than rain area?

Moist convection requires buoyant parcels, which are fueled by the moisture present in the environment and lifting mechanisms that can negate convective inhibition and allow parcels to reach the lifting condensation level. A moister environment will decrease the deleterious impact of entrainment of environmental air on convective updrafts and allow convection to attain greater rain rate intensity–a proxy for updraft speeds. The sensitiv-

ity of the P-r curve to entrainment has been previously recognized (Holloway and Neelin, 2009; Sahany et al., 2012). The pickup for convective intensity in this study represents the lowest grid-scale value of environmental moisture that can support deep convection; the subsequent near-linear relationship between intensity and r highlights the relationship between large-scale saturation and updraft speeds; this relationship also potentially includes the influence of the increasing areal extent of rainfall on the intensity through the reduction in entrainment. The concomitant increase in stratiform rain intensity with convective rain intensity can be explained by the origin of stratiform clouds from deep convective clouds. Convective cloud sizes are lognormal in nature (López, 1977) so the r_t for rain area, which is higher than for rain intensity, most likely represents the large saturation at which there occurs clustering and conglomeration of deep convective clouds. Thus, the convective area pickup can be thought of as the average environmental moisture value that allows the organizing influences of deep convective clouds to be effective, such as downdraft driven cold pools (Tompkins, 2001a; Del Genio, 2012; Feng et al., 2015). The stratiform rain area picks up more rapidly at higher r than the convective rain area, implying that widespread stratiform rain regions evolve from the proliferation of deep convective clouds. This is consistent with observations (Smull and Houze, 1987) and idealized studies (Pandya and Durran, 1996; Fovell, 2002) that contend that the heating from organized convective clouds, such as long-lived squall lines larger than the individual cumulonimbus, is a prerequisite to generate trailing stratiform regions of large areal extent.

IV.4.3 Implications

Cumulus parameterization schemes aiming to utilize the P-*r* curve to constrain precipitation must not only consider the different forms of precipitation (convective, stratiform and shallow), but also consider the utility of discriminating between the intensity and the rain area to capture the onset and organization of tropical rain. The differences in the P-*r* curve between land and ocean can be used as both a tool for diagnosing climate models–on daily time scales–as well as a route to improving the representation of the diurnal cycle of continental convection (Guichard et al., 2004; Grabowski et al., 2006). The near universal pickup threshold for both convective and stratiform rain area over the oceans suggests that a single threshold value can be used to capture the organization of convection over the tropical oceans. A complete understanding of the regional and resolution-based nuances in the P-*r* curve will prove worthwhile if changes to the precipitation-moisture relationship in a warmer world (Sahany et al., 2014) can be anticipated, providing utility in the prediction of precipitation extremes.

IV.5 Summary

The shape of the P-*r* curve for the global tropics was analyzed. A lower pickup threshold and less rapid pickup distinguish continental P-*r* curves from oceanic ones. Regions marked by stability, such as the descending branches of the Walker circulation and the northern part of South China Sea, are marked by more rapid pickups and higher nonlinearity in the P-*r* curve. The intensity of convection picks was found to pickup up at

lower *r* than its areal extent, over both land and ocean.

CHAPTER V

A COLUMN WATER VAPOR PERSPECTIVE OF TROPICAL MOISTURE VARIATIONS

V.1 Background

The MJO (Madden and Julian, 1971) is a many-pronged phenomenon that challenges our understanding of moist thermodynamics, tropical wave dynamics and their myriad multi-scale interactions in time and space that are comprehensively summarized in recent review papers (Zhang, 2005; Lau and Waliser, 2011). The MJO is marked by a variability in its cloud population that transcends scales; within the wavenumber-1 envelope of convection that marks the MJO, there exist modes of higher frequency at the synoptic and meso-scales (Nakazawa, 1988; Hendon and Liebmann, 1994; Chen et al., 1996; Takayabu et al., 1996), though the character of the multi scale organization is not consistent between events (Dias et al., 2013). The cloud population during the MJO thus oscillates on different time scales, modulating environmental conditions like moisture, temperature and winds. It is, however, not completely clear how the high-frequency, smaller-scale variability that comprises the MJO influences the planetary-scale envelope, though many theories involving the upscale transfer of energy and momentum (Biello and Majda, 2005; Kikuchi and Wang, 2010) have been proposed. The role of the local cloud population in modulating the environmental moisture has recently received renewed attention. The discharge-recharge theory (Bladé and Hartmann, 1993; Kemball-Cook and Weare, 2001; Benedict and Ran-

dall, 2007) proposed a slow buildup of moist static energy–on a time-scale of around 20 days–by the local cloud population that gradually destabilizes the environment and helps the transition from shallow to deep convective clouds. Studies have countered this view with the argument that evaporative or eddy moistening by shallow or even congestus clouds is not essential to the transition to deep convection (Hohenegger and Stevens, 2013; Kumar et al., 2014; Hagos et al., 2014b) and attribute the transition to deep convection to large-scale lifting, though it is not clear what the source of the large-scale disturbance is. Other observational studies using the DYNAMO field data have argued that moistening by congestus clouds is crucial on longer time-scales (7-8 days) (Powell and Houze, 2015; Ruppert and Johnson, 2015) than the time it takes for individual convective elements to transition from shallow to deep (2-4 hours) but shorter than the time scale proposed by the original discharge-recharge theory. Modeling studies (Chikira, 2014; Janiga and Zhang, 2016), have also shown that on longer time-scales, the diabatic heating in deep convection can help moisten the atmosphere with the convection serving as a positive feedback on the moisture.

These studies support a growing school of thought that views the MJO as an unstable mode in environmental moisture, destabilized by horizontal and vertical advection. This moisture-mode paradigm is supported by theoretical studies (Neelin and Yu, 1994; Sobel et al., 2001; Sobel and Maloney, 2012, 2013; Adames and Kim, 2016) that show the emergence of such an unstable mode, when an appropriate moisture budget equation is constructed with the weak temperature gradient approximation (Bretherton and Sobel,

2003). This view of the MJO also receives support from observational studies that have found a concurrent increase in column-integrated moisture values with the MJO active phase (Myers and Waliser, 2003; Roundy and Frank, 2004; Yasunaga and Mapes, 2012a). In other words, the histogram of the column integrated value of water vapor (CWV) values during an MJO active phase has a distribution (see Figure 5.1) that is different from the climatological distribution (Figure 6 in Del Genio et al. (2012)). The MJO has been traditionally studied through its precipitation and circulation signals. (Knutson and Weickmann, 1987; Salby and Hendon, 1994; Adames and Wallace, 2015), but for the reasons mentioned above, the CWV field is viewed with particular interest in this chapter.

This focus on moisture as a crucial aspect of the MJO is supported by the tight relationship between environmental moisture and precipitation, discussed in detail in the previous two chapters, where precipitation picks up rapidly beyond a threshold value of CWV (Bretherton et al., 2004; Peters and Neelin, 2006; Holloway and Neelin, 2009). As was shown, the rapid pickup in precipitation is due primarily to an increase in stratiform rain area, signifying an increase in organized convection over the tropical land and oceans. As the CWV increases from low to high values, different components of the local cloud population (shallow, deep convective and stratiform) begin to increase –or pickup–in areal coverage at different values of environmental moisture, with shallow convection picking up at low values of column moisture and stratiform component at higher values. CWV, therefore, can be viewed not merely as a measure of environmental moisture but also as a proxy for the strength and degree of organization of convection that the environment can

sustain, at least over the tropical oceans.

At high values of CWV, the incidence of stratiform clouds increases. The wind field around stratiform clouds (i.e., mid-level convergence leading to mesoscale downdrafts in the lower troposphere Zipser (1977); Houze (1997)) causes environmental drying. Thus, stratiform clouds are a negative feedback on the CWV (Hannah et al., 2016). How then, does the moisture-mode instability arise in the presence of this negative feedback? What processes are responsible for the transition from the CWV values below the threshold for deep convection to points above it? How do these processes vary on different time and space scales? In this study, an attempt to answer these questions is made using a suite of observational data. The moisture (and moist static energy) budget of the MJO has been extensively used in the recent past to probe the phenomenological aspects of the MJO (Kiranmayi and Maloney, 2011; Andersen and Kuang, 2012; Sobel et al., 2014) and will be employed here. Inoue and Back (2015) recently investigated the impact of the time scale on the moist static energy budget, showing that horizontal advection increases in importance as the time scale of interest becomes longer. This study follows on similar lines, as the focus is on how the moisture budget terms are affected by the area and time scales of analysis that adequately encompass the intraseasonal activity over the tropical Indian Ocean with respect to different CWV values of the environment. The primary, process oriented, focus of this chapter is on the contribution of the terms in the moisture budget to the net moistening/drying tendencies; I will, however, attempt to link the relevance of the findings of this chapter to the MJO *phenomenon*, given the central role of moisture

fluctuations in shaping the MJO.

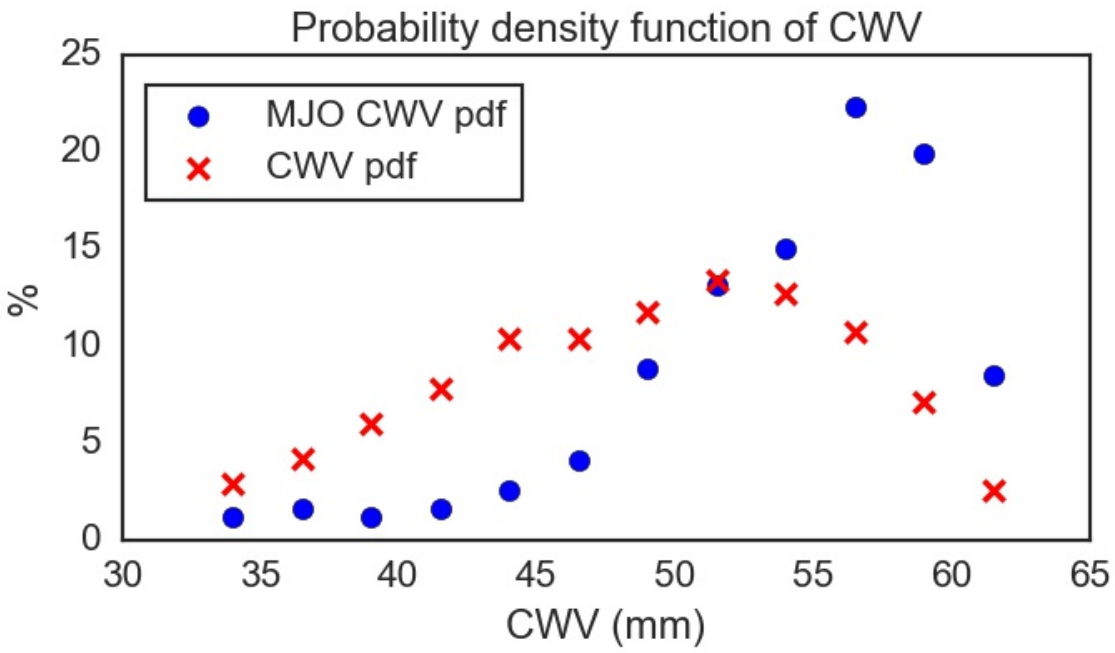

Figure 5.1: The probability distribution functions of CWV during periods of active MJO and all periods as constructed from three years (2011-2013) of 6-hourly ERA-Interim CWV values for a small radar-sized region in the central Indian Ocean. MJO active phases are extracted from filtered TRMM 3B42 rain values (defined as filtered precipitation anomaly greater than 0.1 mmh^{-1}). See section V.2 for more details on the dataset.

V.2 Data and methodology

The primary source for this study is the ERA-I data. Moisture, wind and evaporation terms were all obtained from ERA-I at a horizontal resolution of 0.25 degrees and a 6-hourly time scale for a period of eighteen years (1997-2014). The spatial scales of analysis includes a radar-sized domain (1.75°S - 0.75°N; 71.25°E - 74.25°E) roughly coincident with the range of the radars stationed on Gan Island during the DYNAMO field campaign

(Yoneyama et al., 2013), a domain taken to match the size of the northern sounding array during DYNAMO (1.75°S - 5.5°N; 71.25°E - 82.5°E) and a basin-sized domain (10°S - 10°N; 65°E- 95°E) to include the entirety of the MJO CWV anomaly during an active phase in the central Indian Ocean. These domains are shown in Figure 5.2.

Observations collected on Addu Atoll during DYNAMO are also utilized in this study. Measurements of moisture from Gan Island were obtained from the mergesonde ARM product from October 2 2011 to February 9 2012.

Hourly averaged precipitation and 10 dBz echo top heights were obtained from SMART-R over the eastern half of the 120-km radius radar domain for the same period. The radar reflectivity values were used to separate these quantities into convective and stratiform systems using the Steiner algorithm that was introduced in the previous chapters. Observations from the constrained variational objective analysis of large-scale forcing data (or simply variational analysis), are also used, which is the output from a single column model whose mass, momentum and moisture budgets are constrained using precipitation and sounding observations from Gan and 3-hourly ECMWF analyses. The domain size of the variational analysis dataset is roughly the size of the radar-sized domain described above. The methodology used to obtain this data is described more in detail in Zhang and Lin (1997) and Zhang et al. (2001). Tropical Rainfall Measuring Mission (TRMM) Multi-satellite Precipitation Analysis (TMPA) or the TRMM 3B42 product (Huffman et al., 2007) filtered for tropical intraseasonal waves (Wheeler and Kiladis, 1999) was obtained from Carl Schreck at CICS-NC. The product, originally on a 3-hourly, 0.25 degree grid

was interpolated onto a 6-hourly, 1 degree grid before the wave filters were applied. The rain anomaly time series was subject to temporal and spatial filtering corresponding to the frequencies and wavenumbers for the different equatorial waves: MJO, Kelvin wave, westward propagating inertio-gravity wave (WIG) and the Mixed Rossby-Gravity wave (MRG) (Wheeler and Kiladis, 1999). This was used to isolate the precipitation anomalies associated with the passage of these equatorial waves. More information on this dataset can be found in (Schreck III et al., 2011).

Three years (2011-2013) of this product was used to discern the influence on the moisture budget terms using regression analysis. An example is shown in Figure 5.2, where the background contours are daily-averaged CWV anomalies from ERA-I regressed with the daily-averaged MJO-filtered precipitation over the equatorial Indian Ocean (70°E - 75°E; 2°N - 2°S) for the three-year time period mentioned above. As expected, the column moisture anomalies associated with the MJO span a considerable part of the equatorial Indian Ocean basin.

V.3 Sensitivity of convection to CWV

The sensitivity of the 10-dBz convective echo-top heigh as observed by SMART-R to tropospheric moisture from Gan, is shown in Figure 5.3. Figure 5.3a shows how the 10-dBz convective echo top height is distributed as a function of the CWV, with the mode of the distribution showing the shallow (~3 km) to congestus (~6 km) transition around 40 mm and then the transition to deep convection (echo-top > 6 km) as the CWV increases

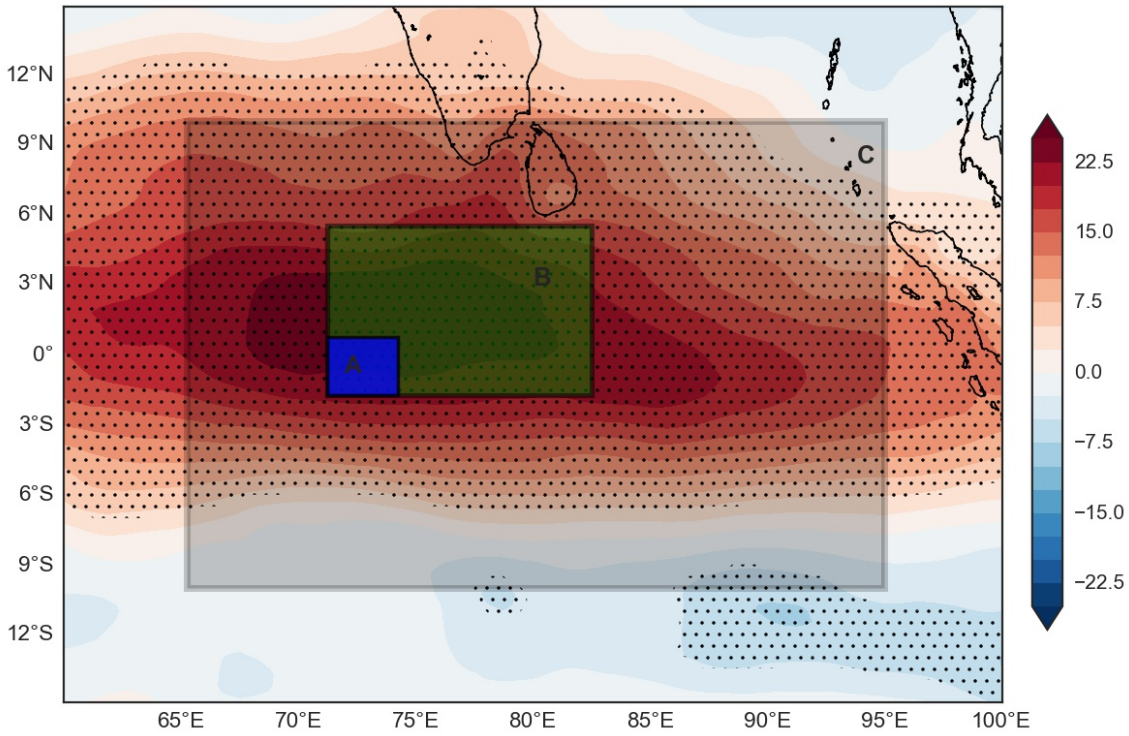

Figure 5.2: The three different domain sizes used in this study. A–radar-sized domain, B–array-sized domain and C–basin-sized domain. The contours are the regressed CWV values with MJO filtered precipitation anomalies in the equatorial Indian Ocean (70°E–75°E; 2°N–2°S); the contours are stippled to show the 95% significance level. The CWV values are from 6-hourly ERA-I data from 2011-2013; the MJO filtered anomalies are from the 6-hourly TRMM 3B42 dataset spanning the same time period.

beyond 50 mm. Figure 5.3b shows the distribution of convective echo top heights versus the moisture in the layer between 850 mb and 600 mb. This figure clearly shows that the mode of the cloud top distribution transitions from 3 km to 6 km for an increase of 2 mm of water vapor in this layer. This result is consistent with other observational studies showing relating cloud depth to tropospheric moisture (Del Genio et al., 2012; Jensen and Del Genio, 2006). The presence of different threshold values of moisture representing different components of the convective cloud population is also consistent with the view that en-

vironmental moistening during DYNAMO occurred in a step-wise fashion (Johnson and Ciesielski, 2013; Johnson et al., 2015). Given that the evolution of the cloud population, particularly the congestus cloud population, has been implicated in the moistening leading up to the MJO onset during DYNAMO (Ruppert and Johnson, 2015; Takemi, 2015), it is useful to know what CWV values support these populations. If cloud-top moistening from cumulus clouds is a dominant source of moisture to the column, then Figures 5.3a and 5.3b imply that processes that allow the tropical atmosphere to reach a CWV value of ~45 mm are sufficient to create a cloud population which can then act to further increase the CWV via moistening at the cloud tops.

Hereinafter, the column moisture threshold for the transition to strong convection (interpreted as widespread MCSs from the results in Chapters III and IV) will be abbreviated to SCT.

To discern how this sensitivity to CWV content affects the convective signatures of intraseasonal waves, four sources of quasi-periodic convective activity in the tropics –the MJO, Kelvin wave, WIGs and the MRGs–are studied with respect to the absolute CWV value. Figure 5.4 shows the TRMM 3B42 filtered precipitation anomalies at each wave frequency binned against the absolute CWV value for the different areas in Figure 5.2. The different domain sizes are used because the value of CWV that supports strong convection can vary based on the size of the areal average (Schiro et al., 2016). The filtered precipitation anomalies for the wavenumber-1 MJO is shown for all three scales, whereas only the radar and array domain averages are presented for the other modes of variability

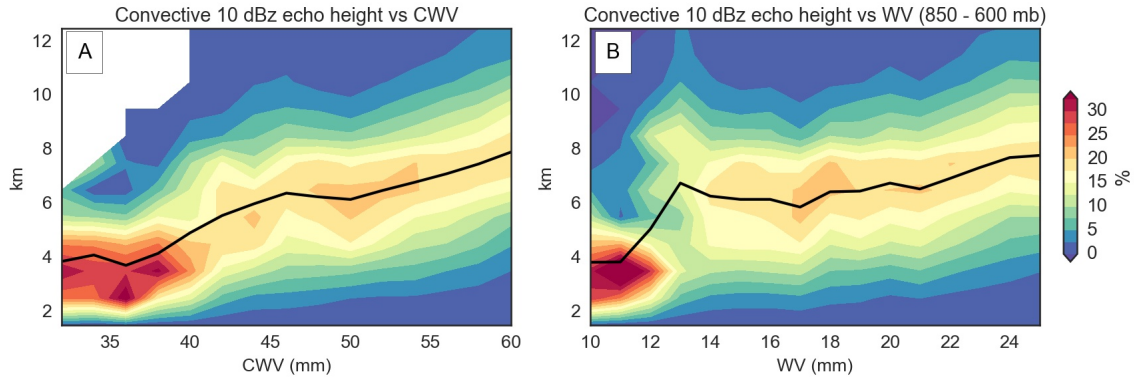

Figure 5.3: The relationship between convection and column moisture as seen from A) 10 dBz convective echo height distribution. Panel B) shows the 10 dBz convective echo top distribution as a function of lower tropospheric moisture content (600-850 mb). The black line in panels A and B is the mean of the distribution in each bin. The echo-top height histograms are computed at 3-hourly intervals from SMART-R data from October 2 2011 - February 9 2012. The CWV values are obtained from the ARM mergesonde product for the same time period.

that inhabit a higher wavenumber domain.

Figure 5.4 shows that the convective signatures of tropical waves are only apparent when the mean state is moist enough to allow the transition to strong convection. The active phase of all wave forms at the radar and array domain scales emerge when the CWV is between 50 - 55 mm. When the tropical P-*r* curve is plotted as a function of CWV at these scales, the SCT usually lies in this range. The basin sized anomalies for the MJO appear to pickup and transition to the active phase (the bin-averaged anomalies > 0 mm/hr) at a CWV value of around 50 mm, but this is clearly an artifact of areal averaging; since it incorporates localized regions of high CWV and associated strong convection within the domain (see Figure 5.5). It is particularly interesting that the WIG activity occupies a narrow range of ambient CWV values. The WIG is marked by the modulation of stratiform rain (Yasunaga

and Mapes, 2012b). The CWV fluctuations associated with the WIG just around the SCT– which is primarily a threshold for widespread stratiform rain– therefore offers a CWV perspective of why the WIG strongly modulates stratiform rain. This suggests that any synoptic activity that can modulate the CWV values to lie closer to the SCT will also enhance the WIG convective signatures in the atmosphere. This could partly explain why the MJO convective envelope–which is an envelope of high CWV values–is accompanied by increased WIG activity (Hendon and Liebmann, 1994; Takayabu et al., 1996).

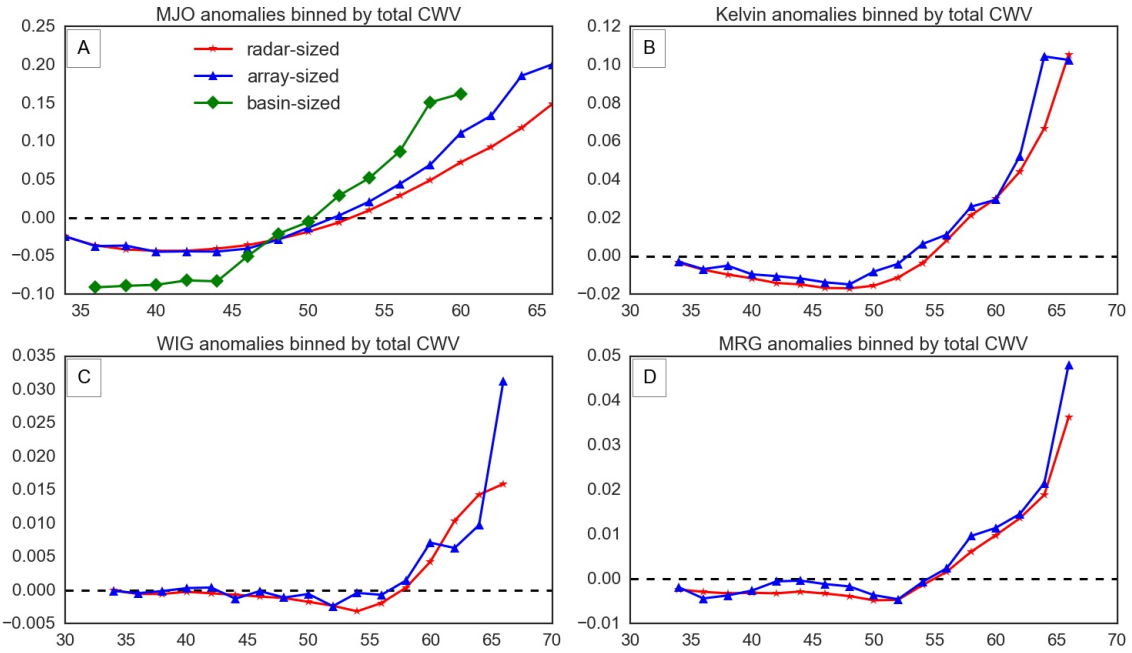

Figure 5.4: Filtered TRMM 3B42 precipitation anomalies binned against total CWV from ERA-I, averaged over different domain sizes for A) MJO B) Kelvin Wave C) WIGs and D) MRGs. The data has a 6-hourly time resolution and includes the 3-year period from 2011-2013. Note that the TRMM 3B42 and ERA-I values have horizontal resolutions of 1°and 0.25°respectively.

Given that most forms of organized convection and intraseasonal activity are highly

sensitive, or at least co-occur, with ambient values of CWV above the SCT and the strong role the associated cloud population plays in modulating the environmental moisture, it is of interest to know how the environment transitions between different values of CWV; particularly between regimes that do not support convection (<40 mm) to regimes that support middle-topped convective clouds (~45-55 mm) to regimes that allow strong, deep, organized convection with widespread stratiform rain to emerge (> 55 mm). What processes control these transitions at different time and space scales? To answer these questions, the terms of the vertically integrated moisture budget as a function of the CWV are now analyzed.

It is first important to point out that the value of the area-averaged CWV can hold different physical meaning as the domain of averaging changes. To study this domain averaging effect, the ERA-I data at 0.25°resolution and 6-hourly intervals is assumed to be represent the transition to strong convection. The percentage of pixels in any given area(radar-sized, array-sized and basin-sized) above a reference value of 55 mm is shown in Figure 5.5. An area-averaged CWV value of 40 mm represents an extremely dry atmosphere for the radar-sized domain, with almost no individual air columns > 50 mm. The same percentage increases to around 15% for array-sized domains and almost 40% for a basin-sized domain. This simply illustrates a property of sampling in the tropical ocean: a large area such as the basin-sized area possesses a minimum fraction of moist air columns (CWV > 50 mm), even when the area-averaged value CWV is low. However, once the area-averaged CWV reaches 50 mm, at least half of all pixels have values of at least 50

mm for all the domain sizes.

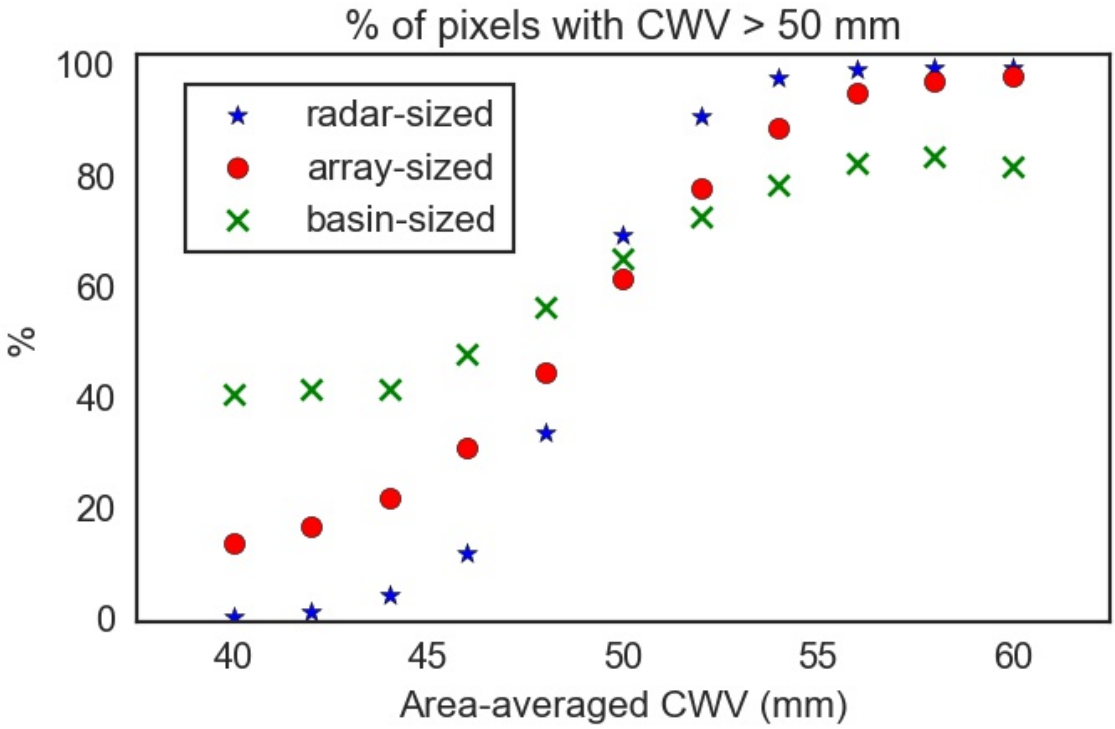

Figure 5.5: The percentage of ERA-I pixels with CWV > 50 mm for different values of area-averaged CWV show for three different domains: radar-sized, array-sized and the basin-sized regions. The ERA-I CWV values span an 18 year time period (1997-2014) and are gridded at 0.25°horizontal resolution and at 6-hourly time intervals.

V.4 Moisture budget analysis

V.4.1 The Lagrangian tendency of moisture

The energetics of a coupled moisture-convection phenomenon such as the MJO can be discerned using a column-integrated moist static energy budget (as in Kiranmayi and Maloney (2011); Andersen and Kuang (2012); Sobel et al. (2014)). CWV, however, is central to the theories of transition to strong convection (Peters and Neelin, 2006; Neelin

et al., 2009) as well some interpretations of the moisture mode (Sobel and Maloney, 2012; Adames and Kim, 2016) and is the variable of interest in this study. The moisture budget is partitioned using the framework proposed by Hannah et al. (2016) in which the tendency of CWV is controlled by the column-integrated horizontal advection (HADV), surface evaporation and the difference between the column-integrated vertical advection of moisture and precipitation called the Lagrangian tendency of column moisture (LCT):

$$\left\langle \frac{dq}{dt} \right\rangle = -\left\langle V_h.\nabla_h q \right\rangle - \underbrace{\left\langle \omega \frac{dq}{dp} \right\rangle - P}_{\text{LCT}} + E \tag{V.1}$$

where q is the specific humidity, < > represents vertical integral, V_h is the horizontal wind, ω is the vertical velocity, and P and E are the precipitation and evaporation, respectively. LCT can be calculated from the moisture budget, without knowledge of the vertical velocity or precipitation:

$$LCT = \left\langle \frac{dq}{dt} \right\rangle + \left\langle V_h.\nabla_h q \right\rangle - E \tag{V.2}$$

As explained in Hannah et al. (2016), the use of LCT to study the moisture budget mitigates the problem of bearing the uncertainties associated with vertical velocity and precipitation estimation and extracts a single variable that represents the moistening and drying processes in a single column. This is equivalent to the column-process term that is also central to moisture mode theories (Chikira, 2014; Wolding and Maloney, 2015; Janiga and Zhang, 2016). Note that the term Lagrangian follows from the form of equation V.2

because of the grouping of the first two terms on the right hand side. This term, however, is interpreted in the Eulerian sense, where the column-process is inferred from the moisture, wind and evaporation terms in the reanalysis dataset. LCT not only includes the effects of cloud-meditated moistening and drying processes via eddy transports and radiative warming, but also the influence of large-scale circulation changes such as low-level moisture convergence and subsidence. The effect of eddy transports in equation V.1 can be inferred by splitting ω into its time mean and deviation from time mean components, but is not done in this study. Another conceptual demarcation between HADV and LCT is that the former can be thought of as the moistening processes affected by mass advection, while the latter is affected by mass convergence. The primary aim of this chapter is to examine the influence of the different source terms in equation V.1 to the column integrated moistening tendency at different time and space scales relevant to the tropical intraseasonal convective activity. Since LCT is inferred from the other terms of moisture budget, any residual terms in the moisture budget from reanalysis calculations (e.g. in Kiranmayi and Maloney (2011)) are grouped with the LCT term.

V.4.2 Validating ERA-I

Figure 5.6 compares the moisture budget terms from ERA-I averaged over the radar-sized domain with the corresponding terms from the variational analysis dataset for a 3-month time period during the DYNAMO field campaign. All the terms are in units of mm/day and smoothed using a 3-day Lanczos filter; it should also be noted that ERA-I

values are 6-hourly snapshots and the variational analysis values are 3-hourly averages. The black line shows the CWV values and clearly depicts the three MJOs (shaded) that were observed on the island as noted by high periods of high CWV (> 55 mm) for a long consecutive period (~10 days). The budget terms from ERA-I and variational analysis show good correspondence in the moistening tendency (blue) and evaporation (green) terms. Some differences are apparent in the partitioning between HADV (yellow) and LCT (magenta) terms, particularly on December 25th, but the overall trends in moistening and drying tendencies of these two terms between the two datasets agree reasonably well. LCT and HADV have small autocorrelation times (not shown), which would explain some of the discrepancies between 6-hourly averages and 6-hourly snapshots. Overall, the trends observed in other moisture budget analyses from DYNAMO (Sobel et al., 2014; Ruppert and Johnson, 2015; Hannah et al., 2016) are confirmed here: the contribution from surface evaporation is always positive and both HADV and LCT contribute to the initiation of the local MJO event, its termination, however, is always ushered in by strong advective drying that is presumably associated with meridional transport of dry sub-tropical air by the off-equatorial cyclonic gyres (Kerns and Chen, 2014).

V.4.3 Contributions to moistening tendency

Figure 5.7 shows the correlation coefficient between two moistening sources (HADV and LCT) and the moistening tendency term as a function of CWV, averaged over different domain sizes. To compute the effective sample size, all samples within each CWV bin that

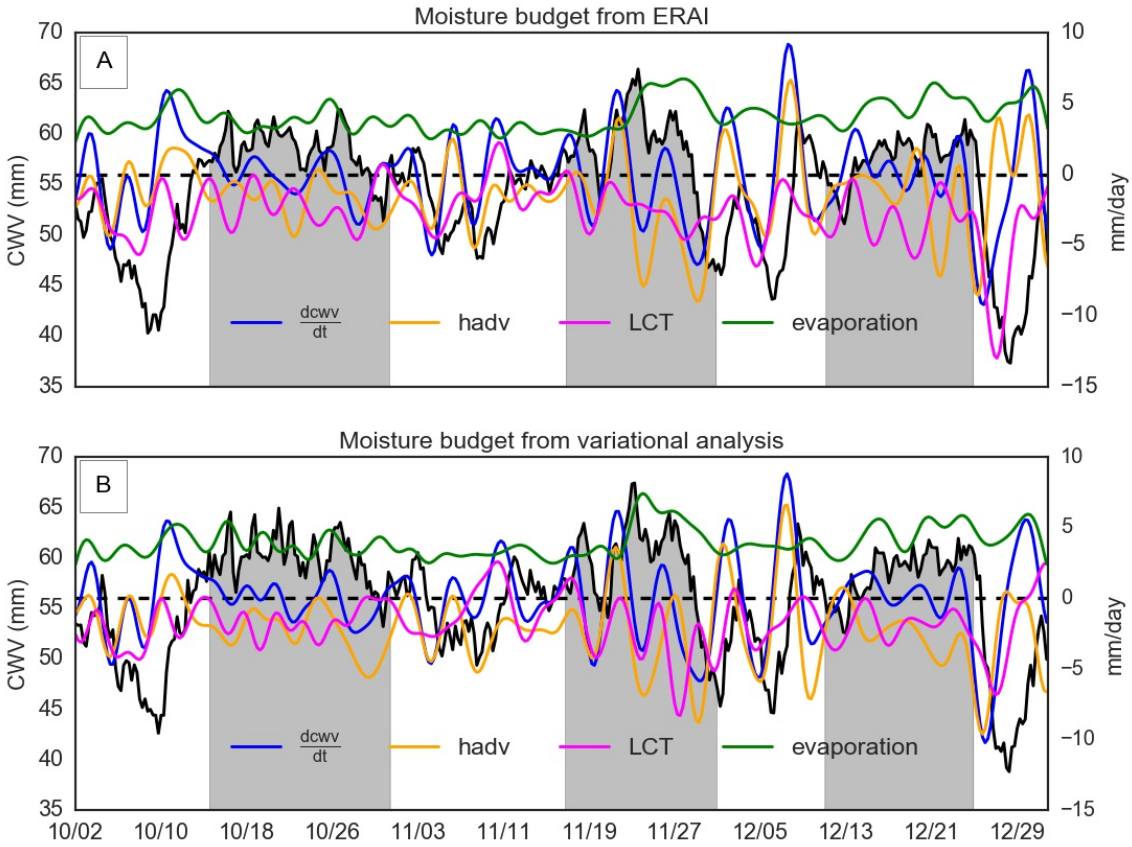

Figure 5.6: Comparison of the moisture budget terms from A) ERA-I radar-sized domain and B) Variational analysis dataset centered over Gan Island during the DYNAMO time period (October 2, 2011 - December 31, 2011). The black line is the CWV value and reads off the left-hand side axis, the other colored lines are the moisture budget terms and read off the right-hand side axis. The grey shading indicates the three MJO events. The ERA-I data are 6-hourly snapshots, while the Variational analysis data are 3-hourly averages; all terms are smoothed with a 3-day Lanczos filter.

lie within one autocorrelation time of each other are counted as one sample. This sample size is in turn used to estimate the 95 % significance level using a two-sided Student's t-test. Only correlation coefficients with statistical significance at the 95 % level are shown here. Evaporation did not show significant correlation with the moistening tendency term and is therefore not shown. Similar analysis can be found in the MJO moisture budget literature, where the contribution of the source terms to the moisture tendency is inferred via correlation coefficients (Tseng et al., 2015) or by the fractional contribution to the variation of the moistening tendency (Andersen and Kuang, 2012; Wolding et al., 2016). In these studies the emphasis was on the phenomenological aspects of the MJO, in contrast to the present emphasis on the moistening process in relation to the absolute CWV.

Figure 5.7a shows that the moistening tendency in drier environments with CWV < 50 mm is largely controlled by horizontal advection for radar-sized domains. The influence of LCT increases as the CWV increases; at very high values of CWV the linear correlation between moistening tendency and horizontal advection decreases. This suggests that as the air columns move towards the SCT, the column process becomes increasingly important in deciding the moistening tendencies.

A similar trend is seen for the larger array-sized domain in Figure 5.7b: the moistening tendencies in drier environments are enslaved to horizontal advection and in moist environments to LCT. Given the greater percentage of moist air columns represented in a larger area (Figure 5.5), the influence of LCT begins to increase at a lower area-averaged CWV value for the array-sized domain than for the radar-sized domain. The large basin-

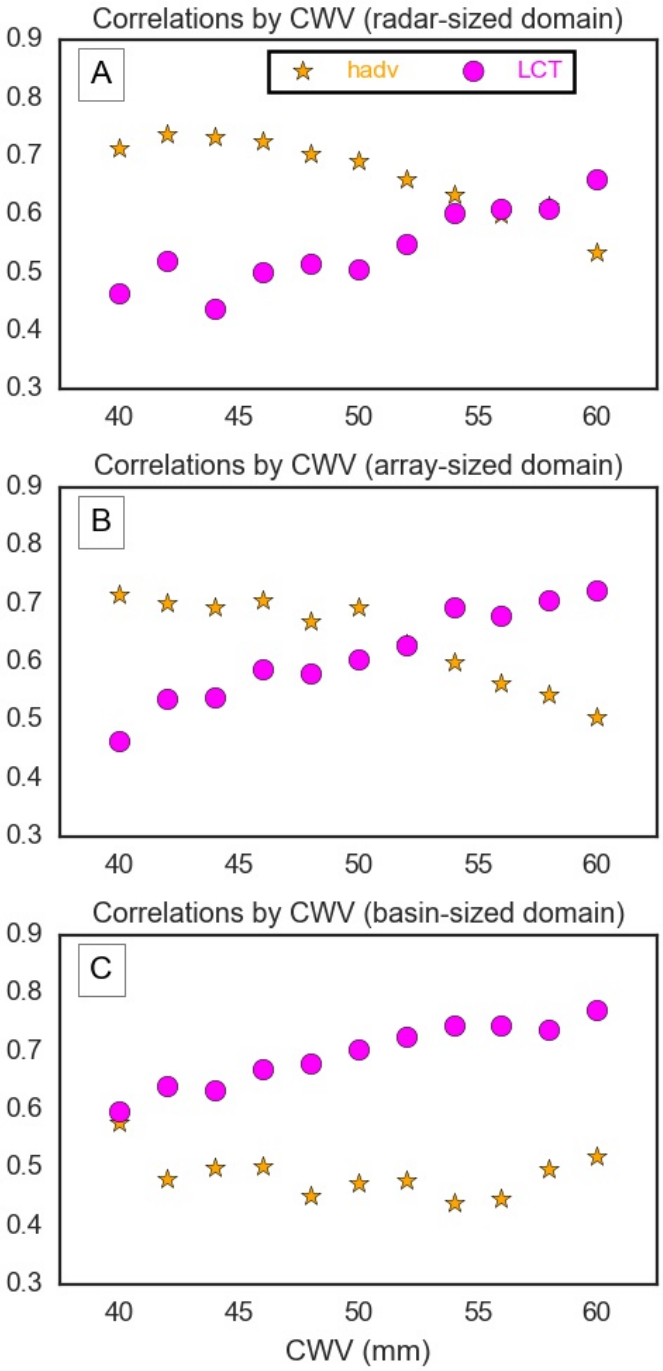

Figure 5.7: Correlation coefficient between the the moistening tendency term and two source terms: HADV and LCT from 18 years (1997-2014) of the ERA-I moisture budget equation. The relationships are depicted as a function of CWV for three domain sizes: a) radar-sized domain, b) array-sized domain and c) the basin-sized domain.

sized domain (Figure 5.7c) shows that the fluctuations in the moistening tendency are most strongly correlated with LCT at CWV values > 40 mm.

Figure 5.7 suggests that the column process more effectively accomplishes basin-wide moistening and drying in all environments, while the influence of horizontal advection on the moistening tendency appears to increase with decreasing spatial scale. To examine the variations in the moistening effects on different time scales, the correlation analysis from Figure 5.7 was repeated for three time scales:

1. 7-20 days: to study the effects of moistening on long time scales; representing the cloud-mediated moistening in the discharge-recharge theory of MJO initiation (Bladé and Hartmann, 1993)
2. 1-7 days: an intermediate time scale; representing the effects of cloud-mediated moistening prior to the MJO onset phase Powell and Houze (2013, 2015)
3. <1-day: a short time scale; to show the effects of the diurnal cycle

The three columns in Figure 5.8 represent the correlation coefficients of the source terms with the moistening tendency term at the different time-scales for each of the three domains. Moistening and drying processes on the 7-20 day time scale are clearly controlled by horizontal advection for all domain sizes (Figure 5.8a, d and g), with the influence of LCT being minimal. This result is in agreement with Inoue and Back (2015), who demonstrated for moist static energy budgets that horizontal advection increases in magnitude and is comparable to vertical advection of MSE as the time scales increase. It is further confirmed that all moistening processes on time scales longer than a few days are effec-

tively controlled by horizontal advection after accounting for the cancellation in vertical advection by precipitation.

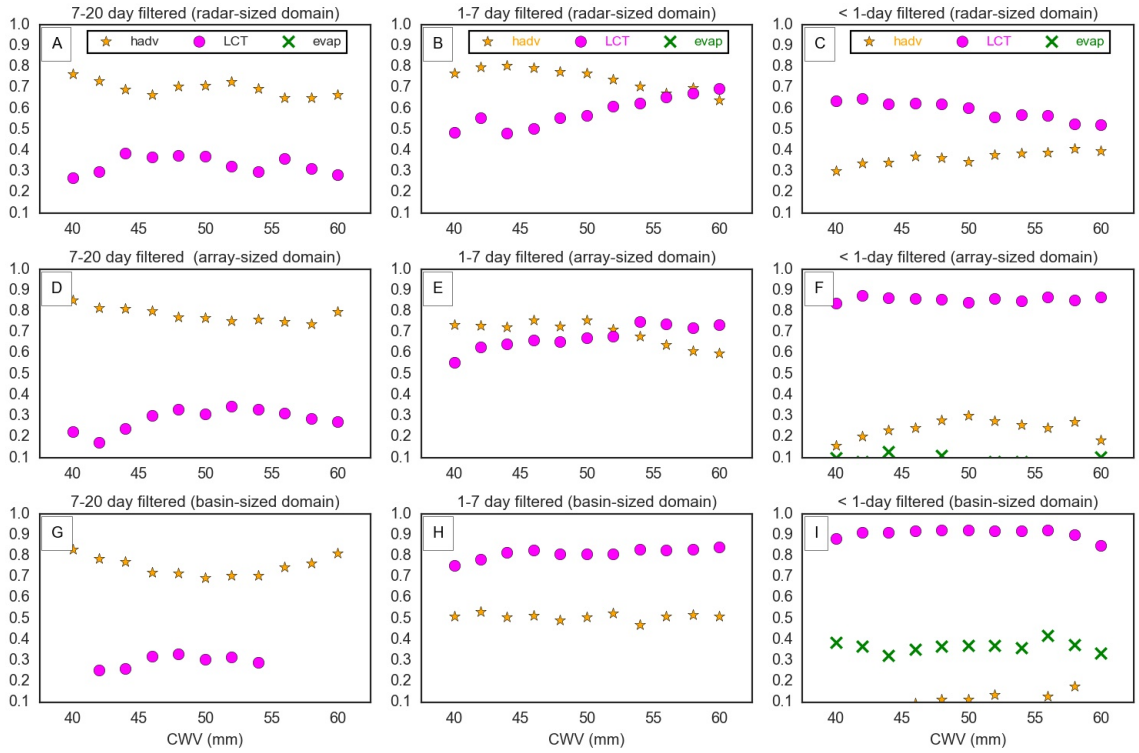

Figure 5.8: Correlation coefficient between the the moistening tendency term and two source terms: HADV and LCT from 18 years of the ERA-I moisture budget equation. The relationships are depicted as a function of CWV for three domain sizes: radar-sized domain (panels a, b & c), array-sized domain (panels d, e & f) and the basin-sized domain (panels g, h & i) and for three different time-scales : 7-20 days (panels a,d & g), 1-7 days (panels b,e & h) and <1-day (panels c,f & i). The time filtering of the data is performed using a Lanczos filter. Only data that are statistically significant at the 95% significance level are shown here.

For the 1-7 day time scale, which is relevant for cloud-mediated moistening processes in the advance of an MJO as mentioned above, LCT plays an increasingly influential role beyond the pickup threshold for the smaller radar- and array-sized domains (Figures 5.8b and e). Therefore, the column can be moistened by both the horizontal advection and the

column process on this timescale over moderate area. However, the basin-wide moistening and drying is effectively tied to the column process on this time-scale (Figure 5.8h) showing that horizontal advection is not an effective mechanism in changing the CWV on time scales shorter than a week for an entire basin. Figures 5.8c,f and i show that LCT is clearly the dominant source and sink term for all three domain sizes at time scales less than a day, presumably representing the diurnal influence of the cloud population on the local moistening tendency (Ruppert and Johnson, 2015).The influence of LCT is markedly greater for the array- and basin-sized domains, with correlation coefficients of 0.9. Evaporation, which is not statistically significant for any other case, is an appreciable factor in the diurnal time scale moistening tendency variations for large spatial scales. The varying influence of the different moistening sources at different time and space scales is a potential source of confusion in the causal attribution of a phenomenon like MJO initiation to a particular process, let alone a specific synoptic event. We can nevertheless attempt to construct a picture of the important processes involved from Figures 5.7 and 5.8. On time scales longer than about week, horizontal advection acts to moisten the columns within a domain, moving columns near and above the SCT. As CWV increases, shallow and congestus clouds increase in activity (Figure 5.3), which triggers the moistening tendencies of the cloud population on the shorter time scale (1- 7 days). As the CWV increases, the influence of LCT overwhelms that of horizontal advection until a large enough region is moistened–or a certain percentage of the domain is above the SCT–to develop the large-scale dynamical features that characterize the MJO. This type of straightforward correlation analysis be-

tween the moistening tendency and its sources only reveals the in-phase contributions of the different terms. To get a clearer picture of the lead and lag relationships between the terms on various time and space scales, spectral analyses of the different moisture budget terms are now presented.

V.4.4 Spectral analysis of the moisture budget

To perform spectral analysis with focus on the intraseasonal wave activity, the terms of the moisture budget from the 18-year time series, on three different domains, were subjected to the conventional pre-processing techniques (Wheeler and Kiladis, 1999; Hendon and Wheeler, 2008; Yasunaga and Mapes, 2012a). The 6-hourly data was first averaged to daily values and the annual mean and the first three harmonics of the annual cycle, estimated using multiple regression, were removed from the dataset. The time series was then divided into 96-day segments with 30 overlapping days. Each segment was tapered using a Hann window and then Fourier transformed to obtain the power spectrum. The power spectra of all segments are averaged to produce a representative spectrum for the entire time series on the intraseasonal time scale. The averaged power spectrum is then smoothed using a 1-2-1 filter to increase the degrees of freedom (dof), which can then be computed as: 2(amplitude and phase) * 18 (years) * 365 (days) * 3 (smoothing by 1-2-1 filter)/96 (days/segment) $\approx$ 410.

Figure 5.9 presents the power spectra for the column moistening tendency, HADV and LCT for the three different domain averages. The dashed and dot-dashed lines are the

99% and the 95% significance levels, computed using the F-test, for statistical significance of the spectral peak above an assumed red noise background with the same dof (thick black line).

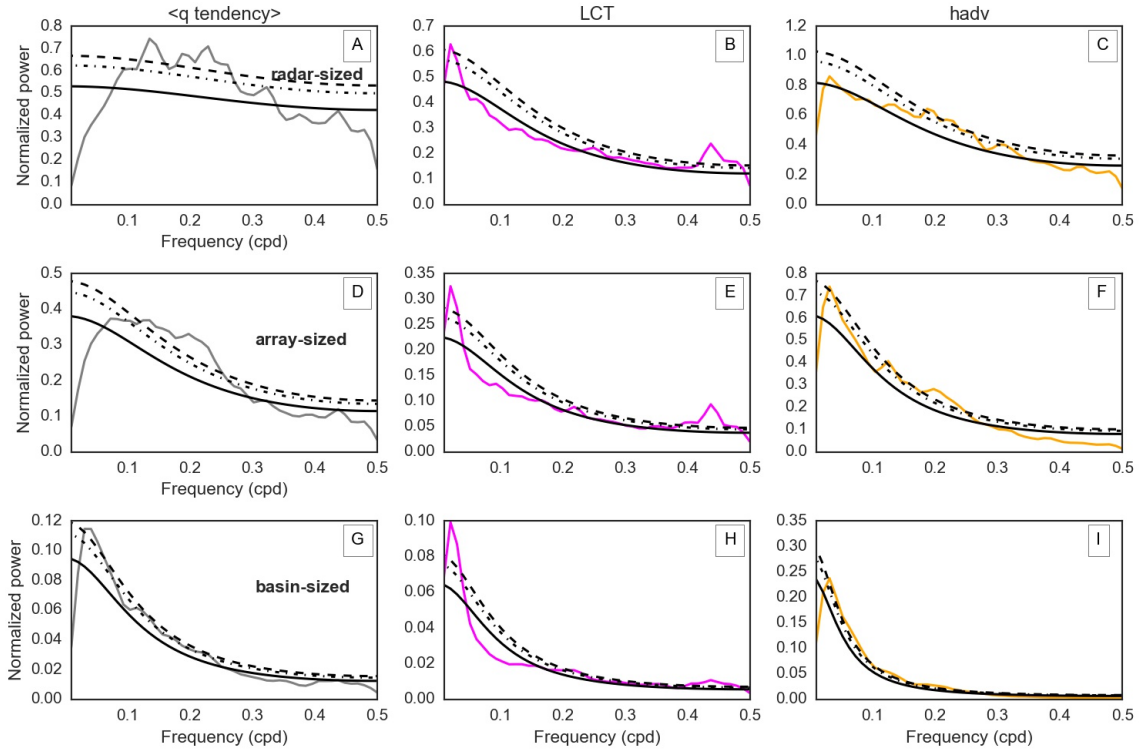

Figure 5.9: The power spectra for the different components of the vertically integrated moisture budget: moisture tendency (panels a,d & g), LCT (panels b, e & h) and HADV (panels c, f & i) for different domain sizes: radar-sized domain (panels a, b & c), array-sized domain (panels d, e & f) and the basin-sized domain (panels c, f & i). The data is from 18 years (1997-2014) of ERA-I. The solid black lines indicates the red-noise curve, computed from the auto-correlation time of the data. The dashed and dash-dot curves demarcate the 95% and 99% significance levels respectively, as computed from an F-test.

The moisture tendency term at the radar-sized domain 5.9a is noisy and exhibits a background spectrum that is nearly white, but increasingly resembles the spectrum of a first order Markov process (AR-1) with increasing area averaging (Figures 5.9d and g) implying

that that moistening tendency acquires memory as the area of averaging increases.

LCT, in contrast, displays AR-1-like background spectra for all domain sizes (Figure 5.9 b, e and h) implying that the moist column possesses memory even at the smaller radar-scale domain, which is presumably a statement about the radar-sized domain being large enough to capture the signal of the cumulus ensemble. LCT has two significant spectral peaks: a peak near the MJO time scale (< 0.1 cpd) at all areal averages and a peak near 0.4 cpd corresponding to the 2-4 day time scale, likely a signature of the 2-4 day westward propagating inertio-gravity wave. The low-frequency (high-frequency) peak increases (decreases) in power as the area of averaging increases confirming that the low and high frequency peaks are indicative of low and high wavenumber signals respectively.

Horizontal advection (Figures 5.9c, f and i) also exhibits an AR-1 background spectrum at all scales, but without any significant spectral peaks. The intraseasonal spectral peaks, at least corresponding to the MJO and the 2-4 day high-frequency waves, are prominent in the LCT term of the moisture budget and not in horizontal advection. This indicates that the intraseasonal variations in the cloud field do not greatly affect the HADV term, even though the latter can facilitate transitions in CWV that can affect the LCT term.

Figure 5.10 shows the coherence-squared statistic between the moistening tendency and its source terms of LCT, HADV and evaporation for the three domain sizes. Coherence squared in this case can be thought of as a measure of the correlation between two time-varying variables on different time scales; the dashed line represents the value of coherence squared that separates the statistically significant values from those that are not.

The necessity of using a continuous time series for spectral analysis precludes any binning by column moisture values. In addition, since the data is daily averages, the diurnal cycle is not visible in these panels.

LCT is weakly coherent with the column moistening tendency on all time scales for the radar-sized domain (Figure 5.10a), while the HADV is highly coherent (Figure 5.10b). This confirms what was seen in Figure 5.8, where HADV was found to be greatly influential in moistening/drying smaller radar-sized domains. As the size of the domain increases (Figures 5.10d and g), the influence of LCT on the moistening term increases along with the emergence of a spectral trend–the coherence increases as the frequency increases (Figures 5.10d & g), such that LCT and moistening tendency are highly coherent at high frequencies for the array and basin-sized domains.However, there also exists a low-frequency coherence peak corresponding to the MJO signal.

HADV (Figures 5.10 b, e and h) shows high spectral coherence at frequencies less than 0.4 for all domain sizes, confirming that low-frequency fluctuations in horizontal advection are efficient in affecting the CWV value. This influence drops-off near the high-frequency WIG peak for the array and basin-sized domains. Evaporation (Figures 5.10c, f and i) is incoherent with moistening tendency for all frequencies except for the low-frequency range in the radar and array-sized domains. The coherence analysis confirms what was found in the previous section: LCT is more coherent with column moistening tendencies at higher frequencies, HADV is more coherent at lower frequencies. The coherence-squared values between evaporation and the moistening tendency are generally

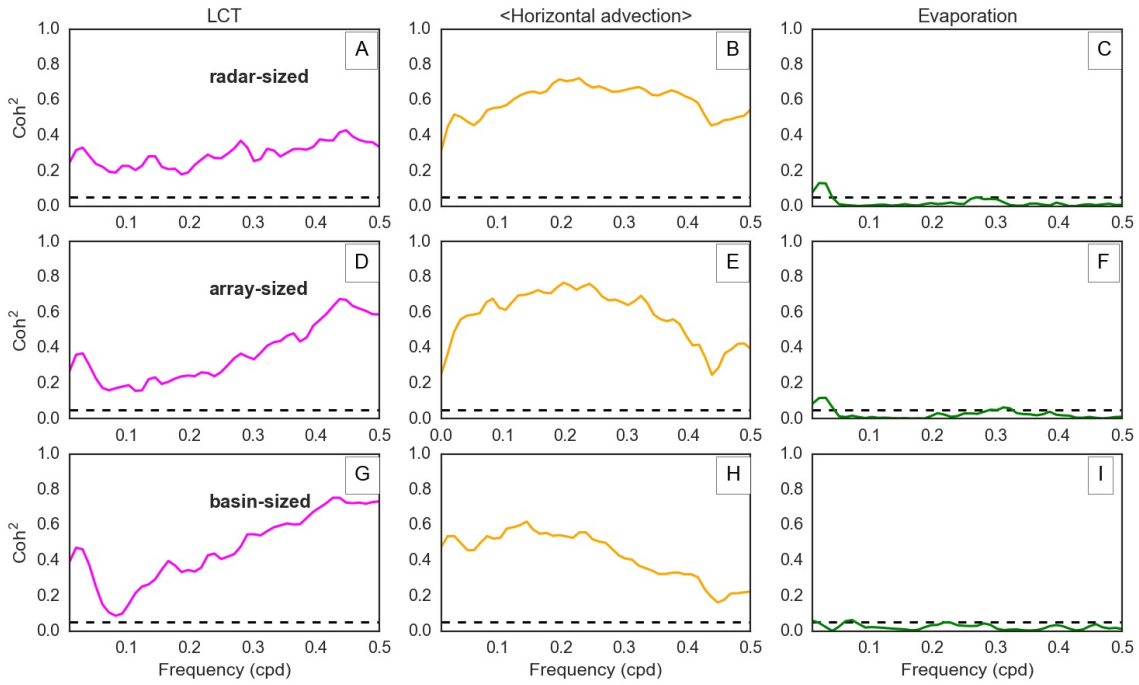

Figure 5.10: The coherence-squared between the column moistening tendency and the different components of the vertically integrated moisture budget: LCT (panels a,d & g), HADV (panels b, e & h) and Evaporation (panels c, f & i) for different domain sizes: radar-sized domain (panels a, b & c), array-sized domain (panels d, e & f) and the basin-sized domain (panels c, f & i). The moisture budget terms are from ERA-I for an 18 year time period (1997-2014) and the dashed line indicates a conservative estimate of the significance level for the coherences-squared values presented here.

weak.

Figure 5.11 shows the phase relationship as a function of frequency for the terms shown in Figure 5.10 for the three domain sizes. HADV (LCT) leads (lags) the moistening tendency term at lower frequencies, while the terms become more in phase as the time scale becomes smaller. This trend holds across all domain sizes. This suggests that the LCT does not increase prior to HADV on time scales greater than 10 days and that the LCT peak observed in Figures 5.9 and 5.10 are a result of the fluctuations in the moistening tendency, rather than a cause.

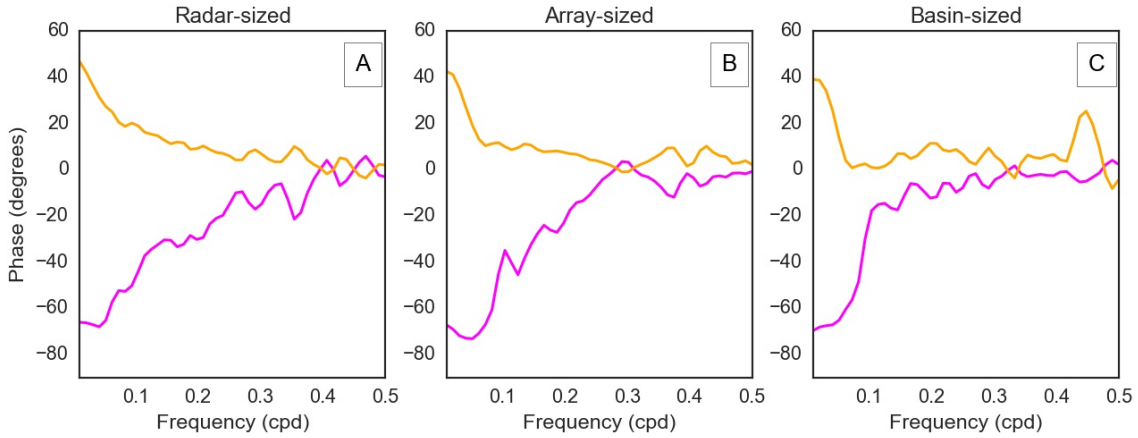

Figure 5.11: The phase in degrees between the column moistening tendency and the different components of the vertically integrated moisture budget: LCT (in magenta) and HADV (in orange) for different domain sizes: radar-sized domain (a), array-sized domain (b) and the basin-sized domain (c). Positive (negative) values indicate the variable leads (lags) the tendency term. All terms are obtained from an 18 year (1997-2014) ERA-I time series.

In an attempt to relate the coherence squared and phase relationships to tropical intraseasonal waves, the filtered TRMM 3B42 dataset is used over the Indian Ocean to extract precipitation anomalies associated with the MJO, Kelvin wave, WIG and the MRG.

The wave-filtered precipitation is then regressed against the different terms of the moisture budget for the basin-sized domain and the resulting lagged regression terms are presented in Figure 5.12. The corresponding signals in wave-regressed CWV are also shown.

As anticipated from features seen in Figures 5.10 and 5.11, the high-frequency WIG (Fig. 5.12a) has a moistening tendency that in phase with the LCT, while the projection of HADV on the moistening tendency associated with the WIG is small. This indicates that moistening associated with the passage of the WIG on this scale is greatly controlled by the fluctuations in the LCT, which is related to the fluctuations in the column-cloud population. This is consistent with the finding that the WIG is a class of wave that modulates the cloud population (Yasunaga and Mapes, 2012b).

For the more rotational MRG (Yasunaga and Mapes, 2012b), the increases in CWV are associated with variations in the HADV term, with a more muted signal in LCT (Figure 5.10b). It should be noted that the LCT signal for the MRG wave increases for smaller areal averages, but since the MRG is a low-wavenumber wave (wavenumbers ~0-3), the larger basin-sized domain most likely captures the strongest signals associated with it.

The Kelvin wave and the MJO (Figures 5.10c and 5.10d), both lower-frequency waves, possess larger phase differences between the moisture budget terms with horizontal advection slightly leading the column moistening tendency and LCT trailing it; the phase differences between horizontal advection and LCT are especially stark for the MJO. It is noteworthy that the column-process term becomes more in phase with the CWV for the low-frequency MJO, which can be construed as evidence for the positive feedback between

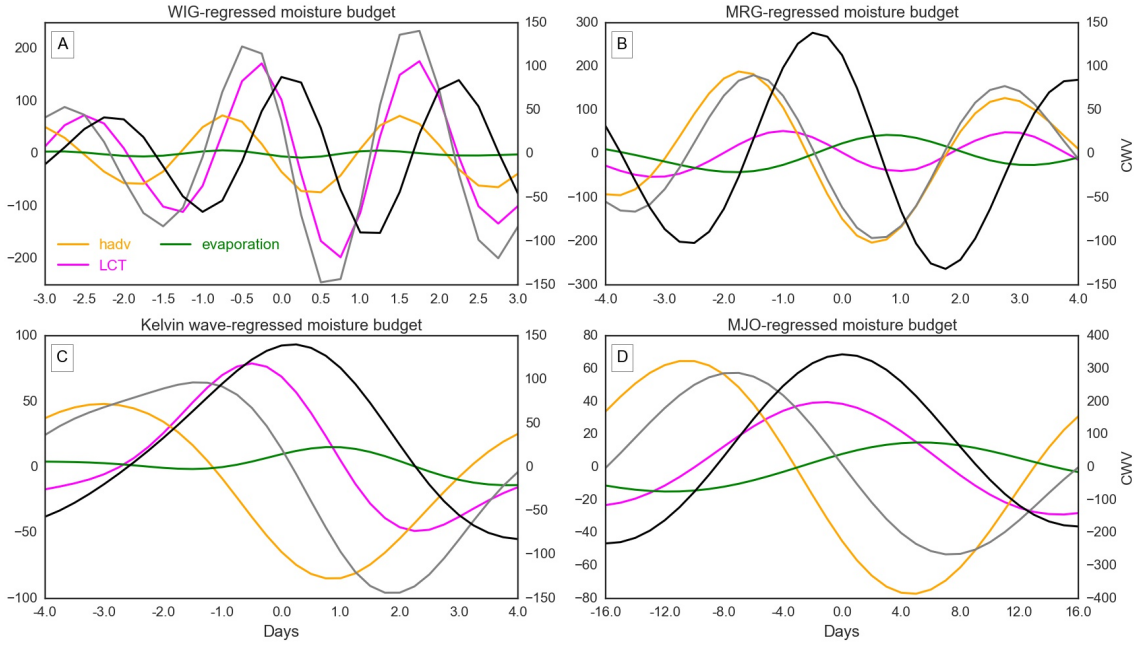

Figure 5.12: The lag-regressed 6-hourly ERA-I moisture budget terms and the TRMM 3B42 filtered-precipitation anomalies averaged over the basin-sized domain. The slopes are presented for four different tropical waves : a) WIG, b) MRG, c) Kelvin wave and the d) MJO. The grey curve is the lag-regressed column moistening tendency and the solid black curve is the CWV. All values are normalized by the standard deviation of the filtered precipitation values. Three years of overlapping data (2011-2013) between the ERA-I and TRMM 3B42 is used to produce this figure.

the cloud-mediated moistening and the column moisture terms, which is usually interpreted as the column process maintaining the instability. Such a positive feedback does not exist for higher frequency waves largely because the source terms are usually decreasing as the CWV nears its maxima. Surface evaporation has a negligible contribution to the moisture budget for the WIG (Figure 5.10a), with a larger signal that is largely out-of-phase with the moistening tendency for the MRG (Figure 5.10b), with the contribution to the MJO being much larger.

V.5 LCT and cloud population

The relationship between the cloud-mediated drying/moistening and the CWV is important because when these two quantities are in phase, the CWV can theoretically grow indefinitely, giving rise to a moisture instability. These quantities are, however, not in phase for higher frequency variability. LCT is influenced by the column cloud population, especially when CWV is above the SCT, which is true for all modes of wave-organized convection, as seen from Figure 5.4. The rest of the analysis in this study concerns the relationship between the cloud population and LCT.

Hannah et al. (2016) probed this relationship using radar and satellite data and concluded that congestus and deep convective clouds are associated with positive LCT_e (which is LCT + evaporation), while stratiform clouds are associated with negative LCT_e. We can draw a similar conclusion by simply binning the stratiform rain fraction from SMART-R with LCT from the variational analysis data, for the 3 months coinciding with the DYNAMO field campaign. Figure 5.13 shows a negative trend in the LCT with increasing stratiform rain fraction; the trend is not very strong (r value ~0.4) because stratiform clouds usually co-occur with deep convective clouds that have a strong positive LCT_e. Modeling studies have also implicated the presence of congestus and deep convective clouds with a positive column process (Chikira, 2014; Janiga and Zhang, 2016). This drying associated with stratiform clouds is anticipated (Raymond et al., 2009) because of its second-baroclinic mode vertical heating profile (Houze, 1982; Schumacher et al., 2004) and also from decades of tropical field observations which show that widespread stratiform rain ac-

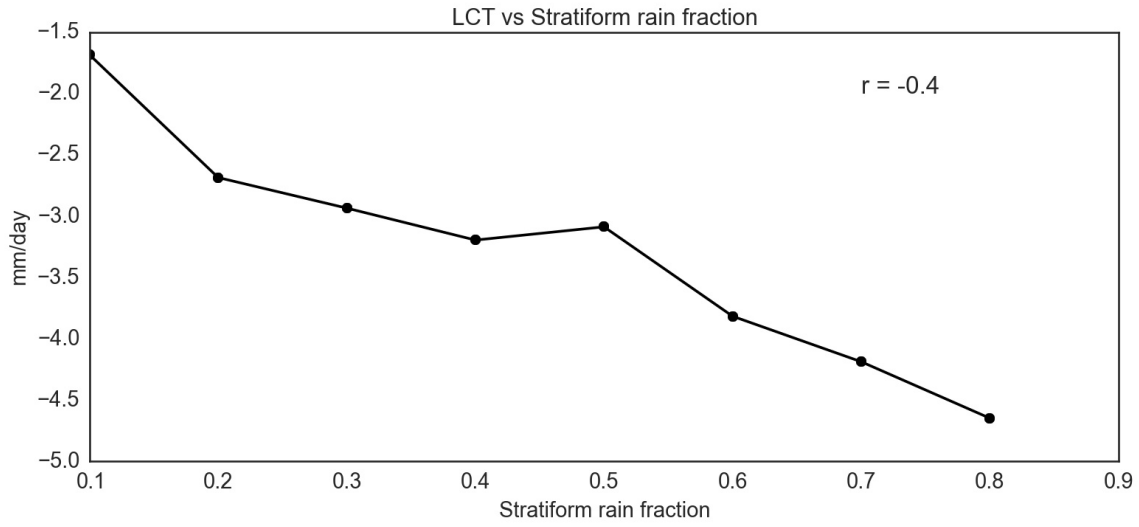

Figure 5.13: The relationship between the 3-hourly values of LCT from variational analysis dataset and stratiform rain fraction from SMART-R. The LCT values are binned by 10% intervals of stratiform rain fraction. The time span of the overlapping datasets is from October 2, 2011 - December 31, 2011.

companied by a mid-level import of dry air (Zipser, 1977) that dries the boundary layer and inhibits new convection. From a strong transition to convection point-of-view, we can view the drying associated with stratiform clouds as the mechanism that transports air columns above the SCT to below, resulting in reduced precipitation. This gives rise to an quadrature phase relationship between CWV and LCT, which is obvious in Figure 5.12a, where increases in CWV above a CWV threshold give rise to decreases in LCT. For the lower-frequency MJO, however, (Figure 5.12d), the LCT appears to actually increase with CWV. This suggests that stratiform drying could be less effective in moving air columns below the SCT, on longer time-scales.

More circumstantial evidence to support this argument is offered in the form of Figure 5.14 which shows the composites of the variational analysis moisture budget terms

and SMART-R convective and stratiform rain amounts and convective echo-top height frequency around 3-hourly and daily stratiform rain maxima. Before the stratiform rain peak (Figure 5.14a), the percentage of deep convective clouds (~8 km echo-top height) increases; the LCT also clearly increases with values close to zero or slightly negative. As stratiform rain peaks, the LCT decreases sharply, leading to a decrease in CWV. It should be noted that in this composite, HADV also contributes to decreasing CWV in the aftermath of the stratiform rain peak. The fact that LCT decreases as the stratiform rain peaks is construed as evidence for the correlation between largely negative LCT and increased stratiform rain.The same trend persists for daily averaged values (Figure 5.14b), which implies that this is not a diurnal trend in LCT. In Figure 5.14 LCT and HADV have largely negative values, but are the primarily modulators of the CWV values, because evaporation has a strong positive contribution to the moisture budget and does not vary on the short time scales (not shown).

In an attempt to further understand the influence of the cloud population on LCT–particularly as a function of frequency, vertical profiles of vertical velocity (omega) from ERA-I are analyzed for the same 18-year period as the moisture budget terms. Omega is used despite the uncertainties and influences from the parent model physics, primarily to diagnose the relationship between its vertical structures and LCT in the hope that some cloud population information can be gleaned. To understand what type of vertical motions–and therefore cloud types–are associated with LCT on different time scales, the coherence squared statistic between omega at each vertical level and the LCT is shown in Figure

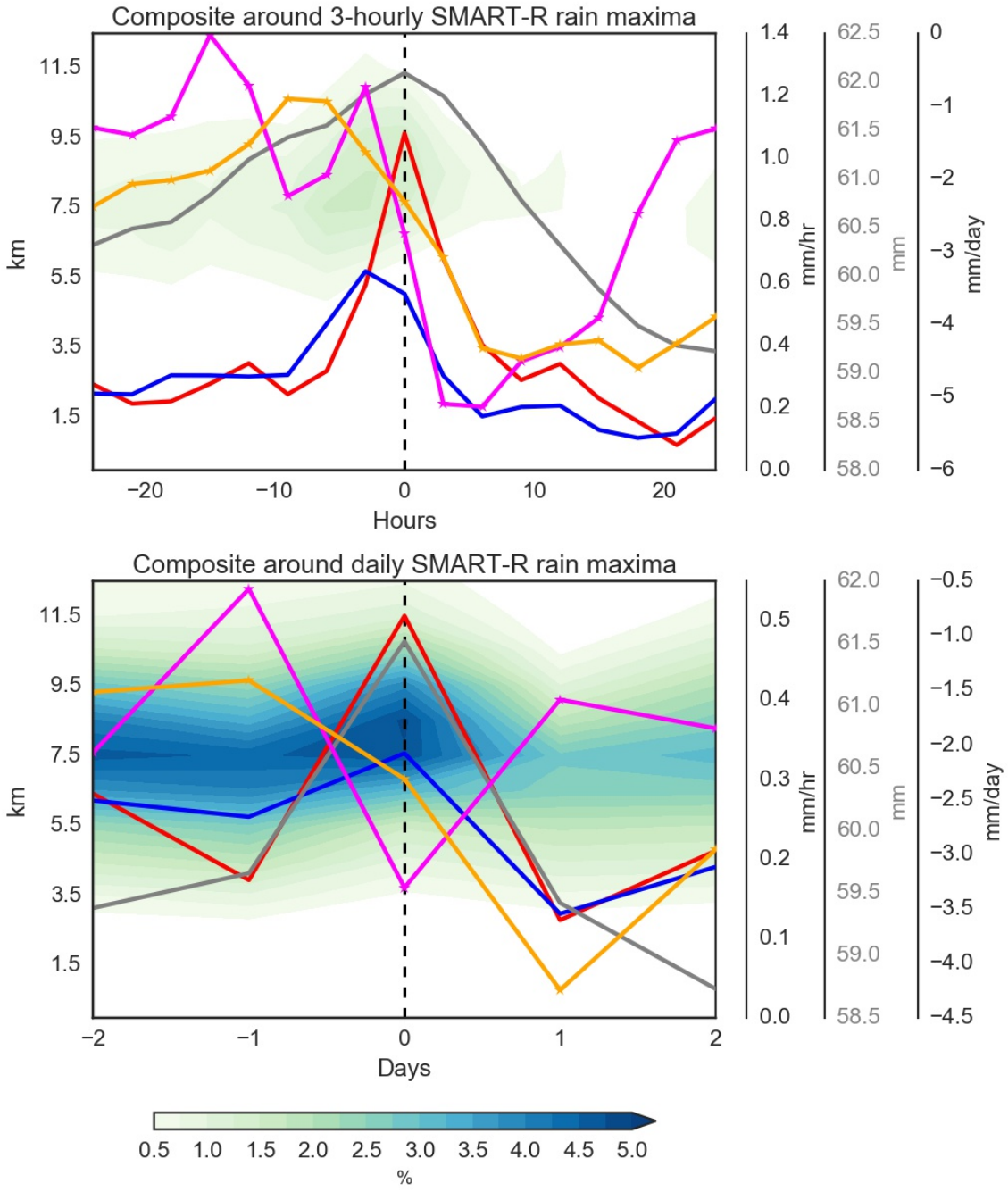

Figure 5.14: Composites around a) 3-hourly SMART-R rain maxima and b) daily SMART-R rain maxima. LCT (magenta), HADV (orange), CWV (grey) are the terms associated with the moisture budget. Convective and stratiform rainfall are shown in blue and red respectively. The colored contours indicate the frequency of the convective cloud-top height as observed by the radar. The time span of the data is from October 2, 2011 - December 31, 2011. The left axes correspond to the height levels for the echo-top height contours. The first axis on the right indicates precipitation, the second axis is CWV and the third axis shows the values for the moisture budget terms.

5.15. The analysis is presented for four different domains: the radar-, array- and the basin-sized domains and an additional domain whose area lies in between the array and basin-sized regions. The coherence squared is displayed on the left and the respective phase (in degrees) are shown on the right.

There are two main features of note in Figure 5.15. The first is that LCT is moderately coherent with low-level vertical motions for high frequency variability. The phase information suggests that increasing LCT is coherent with rising motions at the low-levels. There is also weak coherence between LCT and omega at the upper level (~400 mb) in the array-sized domain, but of opposite phase. The out-of-phase relationship suggests that increasing LCT in this domain is associated with shallow convective motions and/or decreasing LCT values with stratiform-type motions. In other words, LCT at higher frequencies are coherent with the second-baroclinic mode of vertical motion, even though the association with low-level motion is clearly stronger. The second main feature of note in Figure 5.15 is that at lower frequencies, close to the MJO frequency peak, the LCT is highly coherent with an increasingly deeper layer of omega for larger areal averages. The implication is that the column process is associated with the first baroclinic mode vertical structure at low frequencies and averaged over a large domain.

Therefore Figure 5.15 suggests that the cloud-mediated moistening on different time scales are associated with different cloud types. Since low-level omega is more coherent with LCT for higher frequencies, all three cloud types–shallow convective, deep convective and stratiform–can have an impact on the column process. A transition from shallow

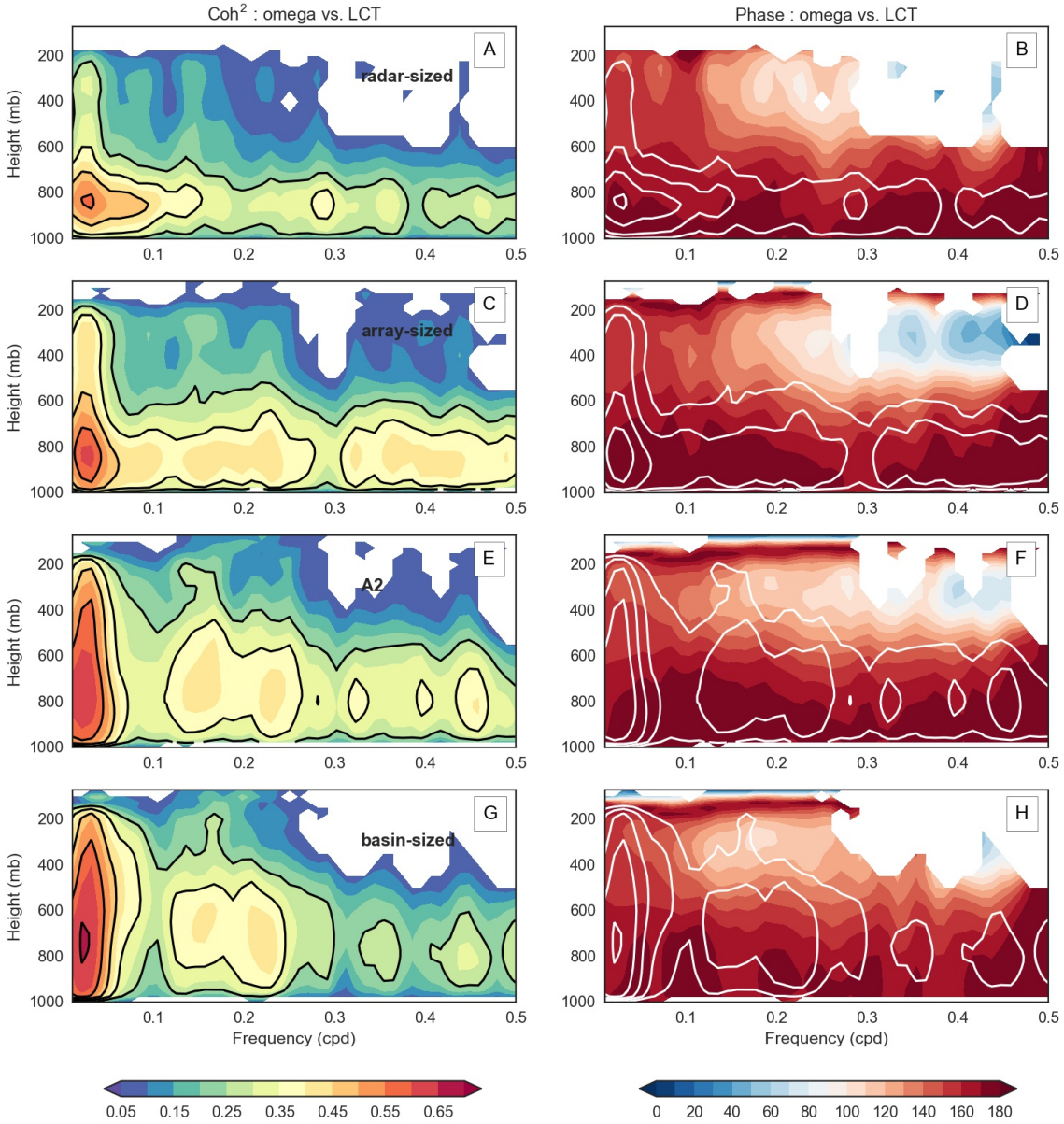

Figure 5.15: Coherences-squared and phase difference between LCT and omega for a,b) radar-sized domain c,d) array-sized domain, e,f) A2 and g,h) basin-sized domain. A2 is a domain whose area lies between the array and the basin sizes. The moisture budget terms are from an ERA-I dataset spanning 18 years (1997-2014).

to deep convective suggest that LCT will act as a positive feedback, while the subsequent transition to stratiform clouds indicates that LCT will begin to act as a negative feedback on the CWV (also seen in Figure 5.14), since high CWV is associated a greater incidence of stratiform clouds (Chapter II). At lower frequencies, LCT is associated with deep layer rising or subsiding motions. In other words the second baroclinic mode does not influence the LCT values on the MJO time scale. This is likely because of the decreased incidence of the second baroclinic mode on the longer time scale (Inoue and Back, 2015). Since the column process associated with the deep convective motion–the first baroclinic mode–tends to moisten the column via the effects of radiative heating and eddy moistening (Chikira, 2014; Janiga and Zhang, 2016; Wolding et al., 2016), it can be deduced that the column process on the MJO time scale acts as a positive feedback on the CWV, thereby bringing both those quantities in phase (Figure 5.12d).

V.6 Discussion

V.6.1 CWV as an active and passive tracer

The distribution of precipitating points as a function of CWV has a Gaussian core with an exponential tail (e.g. Figure 5a in Neelin et al. (2009)). Physical systems where a passive tracer is subject to forced advection-diffusion can reproduce this exponential long tail (Hu and Pierrehumbert, 2001), particularly in the presence of a mean scalar gradient (Shraiman and Siggia, 1994; Bourlioux and Majda, 2002) or additively forced with the scalar (Pierrehumbert, 2000).The tracer in this case–CWV–is not always passive, but the

relationships in Figures 5.8 and 5.9 suggest that CWV can be thought of as a passive tracer below the SCT and an active tracer–that can feedback on the flow–above the SCT. The strength and the direction of the feedbacks then ultimately decide the distribution of CWV.

V.6.2 The CWV view of the MJO

Observational evidence suggests that the MJO can be treated as a sub-sample of the atmosphere, where the CWV population has a long residence time above the SCT. This long residence time inferred from a longer than Gaussian tail of CWV distribution, requires the action of both horizontal and vertical transports of CWV (Lintner et al., 2011). The results of this study suggest that the lateral transport takes the form of slowly forced (> 7 days) horizontal advection and the vertical transport takes the form of intermittent additions and removal of CWV via LCT. Above the SCT, LCT can be an effective source of CWV even on the longer time-scale. Figure 5.15 suggests that this is probably because of the asymmetry in the cloud population: i.e. the column process that moistens the atmosphere as the cloud population evolves from congestus to deep convective clouds is greater than the stratiform-induced drying that follows. The former of these two terms increases in magnitude as the time-scale increases. In other words, at the MJO time scale, the fast dissipative forces–which presumably includes drying by mesoscale downdrafts and short bursts of precipitation–are not effective in restoring the environmental CWV to its climatological equilibrium value. This can also be viewed as a manifestation of the tendency of a dynamical system exhibiting self-organized criticality to evolve away from the critical

point (see section 6.3 in Yano and Plant (2012)).

Given the increased propensity for deep convection above the threshold for organized convection, triggers for convection in the form of higher frequency waves, like the Kelvin wave and the inertio-gravity waves, have prominent convective signatures. Therefore all forms of high frequency activity will possess convective signatures during an MJO. The mechanisms that can initiate the MJO can be viewed as mechanisms that force air columns in an array-sized area (roughly the size of the convective envelope in phase 1 of Figure 8 in Wheeler and Hendon (2004)) to cross the SCT, which is facilitated by horizontal advection on longer time-scales, while shorter time-scale moistening is aided by the column process.

A perusal of the MJO initiation literature suggest multiple phenomenological candidates for how MJO initiation takes place. These can be divided into processes that moisten via impacts in the vertical like cold surges (Wang et al., 2012), reduced upper-level subsidence (Powell and Houze, 2015), ascending motions associated with PV anomalies (Seo and Song, 2012; Li et al., 2015), circumnavigating Kelvin waves (Haertel et al., 2015) and local thermodynamic destabilization (Bladé and Hartmann, 1993; Kemball-Cook and Weare, 2001; Matthews, 2008) etc. and those that involve horizontal transport of moisture, for e.g., via the downstream Rossby wave response to suppressed convection (Zhao et al., 2013; Nasuno et al., 2015).Given the plethora of possible pathways to initiation, it might be tentatively concluded that any synoptic scale process that can moisten a moderately sized (array-sized) area of the tropical atmosphere beyond the SCT, which can then enforce the dynamical response involved in propagation, can excite the convective signature of the

MJO. In other words, there is no single initiation mechanism for the MJO. MJO termination can also be explained using the CWV view, i.e., as the lateral and vertical transport of dry air that takes the air columns in CWV space from above the SCT to below. Therefore both horizontal advection of sub-tropical dry air (Kerns and Chen, 2014) and subsiding motions (Stachnik et al., 2015) are candidates for termination. The question of MJO maintenance from the CWV perspective can be interpreted as concurrent increases of LCT with CWV as observed in Figure 5.12. The time-scale dependence of this positive feedback between LCT and CWV could also explain the preferred time periods for the MJO. In this view, the CWV would continue to grow on the long time scale, if the convection is not "switched off" by subsequent advective or large-scale subsidence drying. Therefore, the MJO phenomenon emerges from a combination of both the lateral transport of CWV by horizontal advection through a maintained gradient of CWV and the growth of moisture anomalies through by the positive feedback created by the cloud population.

V.7 Summary

The processes responsible for moistening and drying in environments of varying moisture content has been analyzed using the column-integrated moisture budget framework of Hannah et al. (2016) for three domains of varying area: from the smallest radar-sized to the largest basin-sized with an intermediate array-sized domain. It is found that very dry environments (< 40 mm) are largely moistened through the effects of horizontal advection for all three domains; as the moisture level increases, the contribution of the col-

umn process–which includes the influence of the columnar cloud population–to the moisture budget increases. The moisture fluctuations in very moist environments (> 55 mm) are strongly associated with the LCT. When separated by time scale, it was found that moisture variations on all three domains are largely controlled by the horizontal advection on time-scales greater than a week. The LCT increasingly controls shorter time-scale variations, and completely controls the diurnal time-scale variations. A spectral analysis of the terms of the moisture budget reveals a prominent low-frequency MJO signal and a high-frequency LCT signal. The low-frequency peak was found to be associated with a deep-layer of vertical velocity, reminiscent of the first baroclinic mode, while the high-frequency peak was largely associated with vertical velocity in the lower levels. This suggests that the action of the LCT via deep convective clouds on the low-frequency time scale is to largely moisten the atmosphere–acting as a positive feedback on the CWV. The LCT can both dry and moisten the atmosphere for variations associated with the high-frequency motions, suggesting that shallow and deep convective clouds can moisten, while stratiform clouds can dry the environment on the short time scale. This change in LCT with time scale is posited to be the reason why LCT and CWV are more in phase with decreasing frequency.

CHAPTER VI

CONCLUSIONS

A better understanding of tropical moist convection and its influence on the large-scale environment is a problem that has plagued the tropical community for decades. The root of the problem lies in the intractability of mathematically describing moist turbulent convection–which extends across scales–and its interactions with the large-scale flow(the environment). Cumulus parameterizations emerged as a workaround to this problem by aiming to describe the relationship between the statistical effects of convection and the environment, by invoking an equilibrium principle, i.e., that the large-scale flow was assumed to be in equilibrium with the cumulative effects of convection. This statistical approach was to some extent successful in improving the the representation of convection in models but has always borne the brunt of complaints for the origin of several biases in GCMs. As a result, the community has increasingly favored the adoption of a more brute-force approach to understanding convection/large-scale interactions, with computer simulations that now extend to ever-higher resolutions. This approach, however, introduces a host of other problems, primarily in the form of the microphysics parameterization. My view is that there exist merits to the statistical approach, particularly in the understanding the wholesale effects of convection/large scale interactions via moisture and heating which are the primary focus of this dissertation. Peculiar properties of this convection/large-scale interaction, such as critical behavior and convective organization, are highlighted.

The main contribution from moist convection to the environment is through the modulation of the heat and moisture budgets. The former involves the release of latent heat, changes to the long wave and shortwave radiative budgets and the eddy transport of sensible heat in the vertical. In the tropics, contributions to the released heat is primarily controlled by the latent heat. The quantification of latent heat in both observations, however, remains problematic, primarily because of uncertainties associated with cloud microphysics and vertical motion. Existing algorithms, particularly those that are a part of the TRMM retrievals, attempt to retrieve the heating from the convective-stratiform separation of precipitation amounts via the utilization of output from CRMs or idealized profiles derived from observational studies. While both classes of algorithms generally perform well in long-term averages, they are sensitive to the accuracy of the rain rate retrievals and pixel rain type classification. The first study of this dissertation was to develop a latent heating algorithm using output from a CRM that uses the organization of convection (defined as the size of the convecting system) in the heating retrieval, in contrast to the precipitation rate of an individual pixel.The constructed algorithm was validated using observations from that DYNAMO field campaign; one satisfactory aspect was the better representation of variability commensurate with the various synoptic activity encountered during DYNAMO. During the course of algorithm building, relationships between the organization of convection and latent heating were also studied and it was found that more organized forms of convection release more latent heating per unit area. This implies that a world with more organized convection will produce prominent circulation changes. There were,

however, aspects of the heating produced by the CRM that the author found troubling. The existence of a heating peak near the boundary layer, which was likely a result of a moisture bias, and an increase in the strength of the downdrafts with increasing resolution, which actually produced weaker convection, were two anomalous features encountered. These results caution against regarding high-resolution simulations as a panacea for the persistent biases plaguing GCMs.

In the recent years, attention has also been paid to the sensitivity of convection to tropospheric moisture. This is underscored by the slew of studies that have changed the entrainment parameter in GCMs to improve in the simulation of intraseasonal features such as the MJO, albeit with a degraded mean state and climatology. To improve the understanding and existing parameterization of convective-environmental interactions better quantification of the relationship between convection and its different components to atmospheric moisture is required, which is carried out in this dissertation. The study of convection-moisture interactions has been statistically quantified in the form of the precipitation-moisture relationship, with its canonical power-law like behavior (the P-*r* curve). The dissection of this curve, with respect to the different components of tropical precipitation–shallow convective, deep convective and stratiform rain–lead to the discovery that the rapid pickup in the precipitation moisture relationship derives largely from the rapid pickup in the stratiform rain. In other words a moist atmosphere will be less efficient at re-evaporation, leading to greater rain at the surface. It was also found that the rapid pickup in the P-*r* curve derives also from the rapid increase in the rain area, espe-

cially related to stratiform precipitation. This result has implications for the understanding of convective organization, which has featured in tropical literature in many forms, such the mesoscale convective system perspective that arose from the tropical field campaigns starting in the 1970s with the Global Atmospheric Research Programme Atlantic Tropical Experiment (GATE). More recently idealized studies have also investigated a phenomena that goes by the moniker of "self-aggregation" where columns of moist air in a CRM under radiative-convective equilibrium aggregate to form an area of highly localized convection surrounded by an area of dry air. The finding that the organization of mesoscale convection–exemplified by its relationship to columnar moisture–is intricately related to the precipitation-moisture relationship is therefore a useful way to attempt to parameterize, or at least validate, this relationship between convective organization and moisture in GCMs.

The global nature of the P-*r* curve was also explored to understand how the varying environments across the tropics, particularly differences in land and ocean, affect how convection originates, organizes and terminates. Given the problematic nature of the problem of parameterizing convection over land, particularly with the diurnal cycle, the finding that convection has a different sensitivity to column moisture over land than the ocean is a useful result. Another useful relationship that emerges from the dissection of the P-*r* curve is between shallow tropical convection and column moisture; the P-*r* curves over the ocean show that the shallow convection picks up in very dry atmospheres making shallow convection near-ubiquitous over the tropical ocean. Measurements from ground radar also

confirm that a linear increase in column moisture is accompanied by a linear increase in the convective echo-top heights, capturing the transition from shallow convective to deep convective precipitation in statistical terms. The shallow to deep to stratiform transition, which lies at the heart of producing organized tropical convection, therefore has a neat correlate with column moisture that could prove relevant in analytical models and cumulus parameterization schemes. The intensity of convection also has a linear relationship with column moisture, which is yet another relationship that can be used for diagnostics and mathematical modeling efforts. Therefore the dissection of the P-*r* curve yields a suite of relationships that can form the bedrock of a radar observationalist's convective parameterization scheme–replete with ubiquitous shallow convection, spatially confined deep convection and areally extensive stratiform rain.

Another interesting problem that is very relevant to the problem of moisture-convection interactions is the topic of the MJO, which has been dubbed the "holy grail" of tropical meteorology. The MJO is a complex phenomenon that does not have well-accepted theoretical explanations for even its most salient features, like its preferred spatial and temporal scales, eastward propagation and phase speed. A recent theory of the MJO claims that it is a form of moisture instability, much like the exponential growth of troughs and ridges associated with mid-latitude baroclininc instability. The moisture instability, or the "moisture-mode", is sustained by the growth of column moisture anomalies aided by the action of convection. This view of convection aiding the growth of moisture is at odds with the traditional view of convection as an effective consumer of column moisture, but

the moisture that is supplied by the convergence associated with convection must also be taken into account.

An effort is made in the last chapter of this dissertation towards unifying the view of tropical convection that emerges from the P-*r* relationship with the idea of a moisture instability associated with the MJO. To accomplish this, long-term data representing the different terms of the vertically integrated moisture budget are utilized. The primary objective was to effectively understand the processes responsible for the moistening and drying of the tropical atmosphere at different values of CWV. It was found that dry atmospheres moisten primarily by the action of horizontal advection, but the horizontal advection can be supplemented by the action of convection, as the environment moistens, such that in very moist environments the column can continue to moisten even in the presence of drying by advection. However, this is not true for all areas and time-scales. It was found that smaller areas are more greatly influenced by horizontal advection, while larger areas are more influenced by the column process. Intermediate areas, which are approximately the size of an initiating MJO envelope, are controlled by the action of both advection and the column process at different values of CWV. This finding highlights the fact that the size of the domain being studied and the time scale are important factors when studying the moisture budget with respect to the MJO. A spectral analysis of the moisture budget terms revealed a spectral peak associated with the MJO and a higher-frequency westward propagating inertio-gravity wave associated with the column process, indicating that the cloud population is modulated by both these forms of intraseasonal variations with one impor-

tant difference: the column process lags increases in the column moistening tendency at low frequencies, while the horizontal advection leads. All the terms of the moisture budget were more in-phase as the time-scale of interest became shorter. Analysis with filtered precipitation anomalies corresponding to the different wave forms revealed that the column moisture and the column process were more in-phase during the longer-frequency MJO hinting at the potential for moisture instability. To understand how the cloud population affects this in-phase behavior at different frequencies, profiles of vertical velocity–a proxy for the cloud population–was used to discern how the column process changes as a function of frequency. At high frequencies, the column process was found to be coherent with fluctuations in the low-level vertical velocity implying that the shallow and stratiform clouds in addition to the deep convective clouds can play a role in the increases and decreases in CWV. Since stratiform clouds primarily dry the column, the speculation is that the column process acts as a negative feedback on shorter time-scales. As the time scale gets longer, however, the LCT is increasingly controlled by vertical velocity throughout a deep layer in the troposphere, implying that the LCT tends to act as a positive feedback on the CWV on longer time-scales. These results lead to the hypothesis that it is the changing character of the cloud population with at different time-scales that leads to a moisture instability in the MJO.

REFERENCES

Adames, Á. F., and D. Kim, 2016: The MJO as a dispersive, convectively coupled moisture wave: Theory and observations. *Journal of the Atmospheric Sciences*, **73 (3)**, 913–941.

Adames, Á. F., and J. M. Wallace, 2015: Three-dimensional structure and evolution of the moisture field in the MJO. *Journal of the Atmospheric Sciences*, **72 (10)**, 3733–3754.

Ahmed, F., and C. Schumacher, 2015: Convective and stratiform components of the precipitation-moisture relationship. *Geophysical Research Letters*, **42 (23)**, 10,453–10,462.

Andersen, J. A., and Z. Kuang, 2012: Moist static energy budget of MJO-like disturbances in the atmosphere of a zonally symmetric aquaplanet. *Journal of Climate*, **25 (8)**, 2782–2804.

Arakawa, A., 2004: The cumulus parameterization problem: Past, present, and future. *Journal of Climate*, **17 (13)**, 2493–2525.

Arakawa, A., and W. H. Schubert, 1974: Interaction of a cumulus cloud ensemble with the large-scale environment, part I. *Journal of the Atmospheric Sciences*, **31 (3)**, 674–701.

Austin, P. M., 1987: Relation between measured radar reflectivity and surface rainfall. *Monthly Weather Review*, **115 (5)**, 1053–1070, doi:10.1175/1520-0493(1987)115<1053:RBMRRA>2.0.CO;2.

Awaka, J., T. Iguchi, H. Kumagai, and K. Okamoto, 1997: Rain type classification algorithm for TRMM precipitation radar. *Remote Sensing - A scientific vision for sustainable development., 1997 IEEE International*, IEEE, Vol. 4, 1633–1635.

Awaka, J., T. Iguchi, and K. Okamoto, 2007: Rain type classification algorithm. *Measuring precipitation from space*, Springer, 213–224.

Benedict, J. J., and D. A. Randall, 2007: Observed characteristics of the MJO relative to maximum rainfall. *Journal of the Atmospheric Sciences*, **64 (7)**, 2332–2354.

Bergemann, M., and C. Jakob, 2016: How important is tropospheric humidity for coastal rainfall in the tropics? *Geophysical Research Letters*, **43**, 5860–5868.

Biello, J. A., and A. J. Majda, 2005: A new multiscale model for the Madden-Julian oscillation. *Journal of the Atmospheric Sciences*, **62 (6)**, 1694–1721.

Bladé, I., and D. L. Hartmann, 1993: Tropical intraseasonal oscillations in a simple nonlinear model. *Journal of the Atmospheric Sciences*, **50 (17)**, 2922–2939.

Bourlioux, A., and A. Majda, 2002: Elementary models with probability distribution function intermittency for passive scalars with a mean gradient. *Physics of Fluids (1994-present)*, **14 (2)**, 881–897.

Bretherton, C. S., M. E. Peters, and L. E. Back, 2004: Relationships between water vapor path and precipitation over the tropical oceans. *Journal of Climate*, **17 (7)**, 1517–1528.

Bretherton, C. S., and P. K. Smolarkiewicz, 1989: Gravity waves, compensating subsidence and detrainment around cumulus clouds. *Journal of the Atmospheric Sciences*, **46 (6)**, 740–759.

Bretherton, C. S., and A. H. Sobel, 2003: The Gill model and the weak temperature gradient approximation. *Journal of the Atmospheric Sciences*, **60 (2)**, 451–460.

Brown, J. M., 1979: Mesoscale unsaturated downdrafts driven by rainfall evaporation: A numerical study. *Journal of the Atmospheric Sciences*, **36 (2)**, 313–338.

Bryan, G. H., and H. Morrison, 2012: Sensitivity of a simulated squall line to horizontal resolution and parameterization of microphysics. *Monthly Weather Review*, **140 (1)**, 202–225.

Chan, S. C., and S. Nigam, 2009: Residual diagnosis of diabatic heating from ERA-40 and NCEP reanalyses: Intercomparisons with TRMM. *Journal of Climate*, **22 (2)**, 414–428.

Charney, J. G., 1963: A note on large-scale motions in the tropics. *Journal of the Atmospheric Sciences*, **20 (6)**, 607–609, doi:10.1175/1520-0469(1963)020<0607:ANOLSM>2.0.CO;2.

Chen, B., and C. Liu, 2016: Warm organized rain systems over the tropical eastern pacific. *Journal of Climate*, **29 (9)**, 3403–3422.

Chen, S. S., R. A. Houze, and B. E. Mapes, 1996: Multiscale variability of deep convec-

tion in relation to large-scale circulation in TOGA COARE. *Journal of the Atmospheric Sciences*, **53 (10)**, 1380–1409.

Chen, T.-C., and M.-C. Yen, 1991: A study of the diabiatic heating associated with the Madden-Julian oscillation. *Journal of Geophysical Research: Atmospheres*, **96 (D7)**, 13 163–13 177, doi:10.1029/91JD01356.

Chikira, M., 2014: Eastward-propagating intraseasonal oscillation represented by Chikira–Sugiyama cumulus parameterization. Part II: Understanding moisture variation under weak temperature gradient balance. *Journal of the Atmospheric Sciences*, **71 (2)**, 615–639.

Cifelli, R., W. A. Petersen, L. D. Carey, S. A. Rutledge, and M. A. da Silva Dias, 2002: Radar observations of the kinematic, microphysical, and precipitation characteristics of two MCSs in TRMM LBA. *Journal of Geophysical Research: Atmospheres*, **107 (D20)**.

Cifelli, R., and S. A. Rutledge, 1998: Vertical motion, diabatic heating, and rainfall characteristics in north Australia convective systems. *Quarterly Journal of the Royal Meteorological Society*, **124 (548)**, 1133–1162.

Dee, D., and Coauthors, 2011: The ERA-interim reanalysis: configuration and performance of the data assimilation system. *Quarterly Journal of the Royal Meteorological Society*, **137 (656)**, 553–597.

Del Genio, A. D., 2012: Representing the sensitivity of convective cloud systems to tropo-

spheric humidity in general circulation models. *Surveys in Geophysics*, **33 (3-4)**, 637–656.

Del Genio, A. D., Y. Chen, D. Kim, and M.-S. Yao, 2012: The mjo transition from shallow to deep convection in CloudSat/CALIPSO data and GISS GCM simulations. *Journal of Climate*, **25 (11)**, 3755–3770.

DePasquale, A., C. Schumacher, and A. Rapp, 2014: Radar observations of MJO and Kelvin wave interactions during DYNAMO/CINDY2011/AMIE. *Journal of Geophysical Research: Atmospheres*, **119 (11)**, 6347–6367.

Dias, J., S. Leroux, S. Tulich, and G. Kiladis, 2013: How systematic is organized tropical convection within the MJO? *Geophysical Research Letters*, **40 (7)**, 1420–1425.

Dudhia, J., 1989: Numerical study of convection observed during the winter monsoon experiment using a mesoscale two-dimensional model. *Journal of the Atmospheric Sciences*, **46 (20)**, 3077–3107.

Emanuel, K., 1997: *Overview of atmospheric convection*, 1–28. Springer.

Emanuel, K. A., J. David Neelin, and C. S. Bretherton, 1994: On large-scale circulations in convecting atmospheres. *Quarterly Journal of the Royal Meteorological Society*, **120 (519)**, 1111–1143.

Feng, Z., S. Hagos, A. K. Rowe, C. D. Burleyson, M. N. Martini, and S. P. Szoeke, 2015: Mechanisms of convective cloud organization by cold pools over tropical warm ocean

during the AMIE/DYNAMO field campaign. *Journal of Advances in Modeling Earth Systems*, **7 (2)**, 357–381.

Fovell, R. G., 2002: Upstream influence of numerically simulated squall-line storms. *Quarterly Journal of the Royal Meteorological Society*, **128 (581)**, 893–912.

Frederick, K., and C. Schumacher, 2008: Anvil characteristics as seen by C-POL during the tropical warm pool international cloud experiment (TWP-ICE). *Monthly Weather Review*, **136**, 206.

Fu, R., B. Zhu, and R. E. Dickinson, 1999: How do atmosphere and land surface influence seasonal changes of convection in the tropical amazon? *Journal of Climate*, **12 (5)**, 1306–1321.

Funk, A., C. Schumacher, and J. Awaka, 2013: Analysis of rain classifications over the tropics by version 7 of the TRMM PR 2A23 algorithm. *Journal of the Meteorological Society of Japan*, **91 (3)**, 257–272.

Gill, A., 1980: Some simple solutions for heat-induced tropical circulation. *Quarterly Journal of the Royal Meteorological Society*, **106 (449)**, 447–462.

Gilmore, J. B., 2015: Understanding the influence of measurement uncertainty on the atmospheric transition in rainfall and column water vapor. *Journal of the Atmospheric Sciences*, **72 (5)**, 2041–2054.

Grabowski, W., and Coauthors, 2006: Daytime convective development over land: A

model intercomparison based on LBA observations. *Quarterly Journal of the Royal Meteorological Society*, **132 (615)**, 317–344.

Grabowski, W. W., 2003: MJO-like coherent structures: Sensitivity simulations using the cloud-resolving convection parameterization (CRCP). *Journal of the Atmospheric Sciences*, **60 (6)**, 847–864.

Grecu, M., and W. S. Olson, 2006: Bayesian estimation of precipitation from satellite passive microwave observations using combined radar-radiometer retrievals. *Journal of Applied Meteorology and Climatology*, **45 (3)**, 416–433, doi:10.1175/JAM2360.1.

Guichard, F., and Coauthors, 2004: Modelling the diurnal cycle of deep precipitating convection over land with cloud-resolving models and single-column models. *Quarterly Journal of the Royal Meteorological Society*, **130 (604)**, 3139–3172.

Haertel, P., K. Straub, and A. Budsock, 2015: Transforming circumnavigating Kelvin waves that initiate and dissipate the Madden-Julian Oscillation. *Quarterly Journal of the Royal Meteorological Society*, **141 (690)**, 1586–1602.

Hagos, S., 2010: Building blocks of tropical diabatic heating. *Journal of the Atmospheric Sciences*, **67 (7)**, 2341–2354, doi:10.1175/2010JAS3252.1.

Hagos, S., Z. Feng, C. D. Burleyson, K.-S. S. Lim, C. N. Long, D. Wu, and G. Thompson, 2014a: Evaluation of convection-permitting model simulations of cloud populations associated with the Madden-Julian Oscillation using data collected during the AMIE/-

DYNAMO field campaign. *Journal of Geophysical Research: Atmospheres*, **119 (21)**, 12,052–12,068, doi:10.1002/2014JD022143, 2014JD022143.

Hagos, S., Z. Feng, K. Landu, and C. N. Long, 2014b: Advection, moistening, and shallow-to-deep convection transitions during the initiation and propagation of Madden-Julian Oscillation. *Journal of Advances in Modeling Earth Systems*, **6 (3)**, 938–949.

Hagos, S., and L. R. Leung, 2011: Moist thermodynamics of the Madden-Julian oscillation in a cloud-resolving simulation. *Journal of Climate*, **24 (21)**, 5571–5583, doi:10.1175/2011JCLI4212.1.

Hagos, S., and C. Zhang, 2010: Diabatic heating, divergent circulation and moisture transport in the African monsoon system. *Quarterly Journal of the Royal Meteorological Society*, **136 (S1)**, 411–425, doi:10.1002/qj.538.

Hannah, W. M., B. E. Mapes, and G. S. Elsaesser, 2016: A Lagrangian view of moisture dynamics during DYNAMO. *Journal of the Atmospheric Sciences*, **73 (5)**, 1967–1985.

Hartmann, D. L., H. H. Hendon, and R. A. Houze, 1984: Some implications of the mesoscale circulations in tropical cloud clusters for large-scale dynamics and climate. *Journal of the Atmospheric Sciences*, **41 (1)**, 113–121.

Hearty, T. J., and Coauthors, 2014: Estimating sampling biases and measurement uncertainties of AIRS/AMSU-A temperature and water vapor observations using MERRA reanalysis. *Journal of Geophysical Research: Atmospheres*, **119 (6)**, 2725–2741.

Hendon, H. H., and B. Liebmann, 1994: Organization of convection within the Madden-Julian Oscillation. *Journal of Geophysical Research: Atmospheres*, **99 (D4)**, 8073–8083.

Hendon, H. H., and M. C. Wheeler, 2008: Some space-time spectral analyses of tropical convection and planetary-scale waves. *Journal of the Atmospheric Sciences*, **65 (9)**, 2936–2948.

Hohenegger, C., and B. Stevens, 2013: Preconditioning deep convection with cumulus congestus. *Journal of the Atmospheric Sciences*, **70 (2)**, 448–464.

Holloway, C. E., and J. D. Neelin, 2009: Moisture vertical structure, column water vapor, and tropical deep convection. *Journal of the Atmospheric Sciences*, **66 (6)**, 1665–1683.

Holloway, C. E., and J. D. Neelin, 2010: Temporal relations of column water vapor and tropical precipitation. *Journal of the Atmospheric Sciences*, **67 (4)**, 1091–1105.

Hopper, L. J., and C. Schumacher, 2012: Modeled and observed variations in storm divergence and stratiform rain production in southeastern Texas. *Journal of the Atmospheric Sciences*, **69 (4)**, 1159–1181.

Hottovy, S., and S. N. Stechmann, 2015: Threshold models for rainfall and convection: Deterministic versus stochastic triggers. *SIAM Journal on Applied Mathematics*, **75 (2)**, 861–884.

Houghton, H. G., 1968: On precipitation mechanisms and their artificial modifica-

tion. *Journal of Applied Meteorology*, **7 (5)**, 851–859, doi:10.1175/1520-0450(1968)007<0851:OPMATA>2.0.CO;2.

Houze, R. A., 1982: Cloud clusters and large-scale vertical motions in the tropics. *Journal of the Meteorological Society of Japan*, **60 (1)**, 396–410.

Houze, R. A., 1989: Observed structure of mesoscale convective systems and implications for large-scale heating. *Quarterly Journal of the Royal Meteorological Society*, **115 (487)**, 425–461.

Houze, R. A., 1997: Stratiform precipitation in regions of convection: A meteorological paradox? *Bulletin of the American Meteorological Society*, **78 (10)**, 2179–2196.

Houze, R. A., 2004: Mesoscale convective systems. *Reviews of Geophysics*, **42 (4)**.

Houze, R. A., and A. K. Betts, 1981: Convection in GATE. *Reviews of Geophysics*, **19 (4)**, 541–576.

Houze, R. A., S. Brodzik, C. Schumacher, S. E. Yuter, and C. R. Williams, 2004: Uncertainties in oceanic radar rain maps at Kwajalein and implications for satellite validation. *Journal of Applied Meteorology*, **43 (8)**, 1114–1132, doi:10.1175/1520-0450(2004)043<1114:UIORRM>2.0.CO;2.

Hu, Y., and R. T. Pierrehumbert, 2001: The advection-diffusion problem for stratospheric flow. Part I: Concentration probability distribution function. *Journal of the Atmospheric Sciences*, **58 (12)**, 1493–1510.

Huffman, G. J., and Coauthors, 2007: The TRMM multisatellite precipitation analysis (TMPA): Quasi-global, multiyear, combined-sensor precipitation estimates at fine scales. *Journal of Hydrometeorology*, **8 (1)**, 38–55.

Hung, M.-P., J.-L. Lin, W. Wang, D. Kim, T. Shinoda, and S. J. Weaver, 2013: MJO and convectively coupled equatorial waves simulated by CMIP5 climate models. *Journal of Climate*, **26 (17)**, 6185–6214.

Iacono, M. J., E. J. Mlawer, S. A. Clough, and J.-J. Morcrette, 2000: Impact of an improved longwave radiation model, RRTM, on the energy budget and thermodynamic properties of the ncar community climate model, CCM3. *Journal of Geophysical Research*, **105 (D11)**, 14 873–14 890.

Iguchi, T., T. Kozu, J. Kwiatkowski, R. Meneghini, J. Awaka, and K. Okamoto, 2009: Uncertainties in the rain profiling algorithm for the TRMM precipitation radar. *Journal of the Meteorological Society of Japan*, **87**, 1–30.

Inoue, K., and L. Back, 2015: Column-integrated moist static energy budget analysis on various time scales during TOGA COARE. *Journal of the Atmospheric Sciences*, **72 (5)**, 1856–1871.

Janiga, M. A., and C. Zhang, 2016: MJO moisture budget during DYNAMO in a cloud-resolving model. *Journal of the Atmospheric Sciences*, **73 (6)**, 2257–2278.

Janjić, Z. I., 2002: Nonsingular implementation of the mellor–yamada level 2.5 scheme in the NCEP meso model. *NCEP Office Note*, **437**, 61.

Jensen, M. P., and A. D. Del Genio, 2006: Factors limiting convective cloud-top height at the ARM Nauru Island climate research facility. *Journal of Climate*, **19 (10)**, 2105–2117.

Jiang, X., and Coauthors, 2011: Vertical diabatic heating structure of the MJO: Intercomparison between recent reanalyses and TRMM estimates. *Monthly Weather Review*, **139 (10)**, 3208–3223, doi:10.1175/2011MWR3636.1.

Jiang, X., and Coauthors, 2015: Vertical structure and physical processes of the madden-julian oscillation: Exploring key model physics in climate simulations. *Journal of Geophysical Research: Atmospheres*, **120 (10)**, 4718–4748.

Jin, Q., X.-Q. Yang, X.-G. Sun, and J.-B. Fang, 2013: East Asian summer monsoon circulation structure controlled by feedback of condensational heating. *Climate Dynamics*, **41 (7)**, 1885–1897.

Johnson, R. H., S. L. Aves, P. E. Ciesielski, and T. D. Keenan, 2005: Organization of oceanic convection during the onset of the 1998 East Asian summer monsoon. *Monthly Weather Review*, **133 (1)**, 131–148.

Johnson, R. H., and P. E. Ciesielski, 2013: Structure and properties of Madden-Julian Oscillations deduced from dynamo sounding arrays. *Journal of the Atmospheric Sciences*, **70 (10)**, 3157–3179.

Johnson, R. H., P. E. Ciesielski, and K. A. Hart, 1996: Tropical inversions near the 0 c level. *Journal of the Atmospheric Sciences*, **53 (13)**, 1838–1855.

Johnson, R. H., P. E. Ciesielski, J. H. Ruppert, and M. Katsumata, 2015: Sounding-based thermodynamic budgets for DYNAMO. *Journal of the Atmospheric Sciences*, **72 (2)**, 598–622.

Johnson, R. H., and G. S. Young, 1983: Heat and moisture budgets of tropical mesoscale anvil clouds. *Journal of the Atmospheric Sciences*, **40 (9)**, 2138–2147.

Jung, J.-H., and A. Arakawa, 2004: The resolution dependence of model physics: Illustrations from nonhydrostatic model experiments. *Journal of the Atmospheric Sciences*, **61 (1)**, 88–102.

Kemball-Cook, S. R., and B. C. Weare, 2001: The onset of convection in the Madden-Julian Oscillation. *Journal of Climate*, **14 (5)**, 780–793.

Kerns, B. W., and S. S. Chen, 2014: Equatorial dry air intrusion and related synoptic variability in MJO initiation during DYNAMO. *Monthly Weather Review*, **142 (3)**, 1326–1343.

Khairoutdinov, M., and D. Randall, 2006: High-resolution simulation of shallow-to-deep convection transition over land. *Journal of the Atmospheric Sciences*, **63 (12)**, 3421–3436.

Khouider, B., J. Biello, A. J. Majda, and Coauthors, 2010: A stochastic multicloud model for tropical convection. *Communications in Mathematical Sciences*, **8 (1)**, 187–216.

Khouider, B., and A. J. Majda, 2006: Multicloud convective parametrizations with crude vertical structure. *Theoretical and Computational Fluid Dynamics*, **20 (5-6)**, 351–375.

Kikuchi, K., and B. Wang, 2010: Spatiotemporal wavelet transform and the multiscale behavior of the Madden-Julian Oscillation. *Journal of Climate*, **23 (14)**, 3814–3834.

Kiladis, G. N., K. H. Straub, and P. T. Haertel, 2005: Zonal and vertical structure of the Madden-Julian Oscillation. *Journal of the Atmospheric Sciences*, **62 (8)**, 2790–2809.

Kiranmayi, L., and E. D. Maloney, 2011: Intraseasonal moist static energy budget in reanalysis data. *Journal of Geophysical Research: Atmospheres*, **116 (D21)**.

Kirshbaum, D. J., and R. B. Smith, 2009: Orographic precipitation in the tropics: Large-eddy simulations and theory. *Journal of the Atmospheric Sciences*, **66 (9)**, 2559–2578.

Knutson, T. R., and K. M. Weickmann, 1987: 30-60 day atmospheric oscillations: Composite life cycles of convection and circulation anomalies. *Monthly Weather Review*, **115 (7)**, 1407–1436.

Kumar, V. V., A. Protat, C. Jakob, and P. T. May, 2014: On the atmospheric regulation of the growth of moderate to deep cumulonimbus in a tropical environment. *Journal of the Atmospheric Sciences*, **71 (3)**, 1105–1120.

Lac, C., J.-P. Lafore, and J.-L. Redelsperger, 2002: Role of gravity waves in triggering deep convection during TOGA COARE. *Journal of the Atmospheric Sciences*, **59 (8)**, 1293–1316, doi:10.1175/1520-0469(2002)059<1293:ROGWIT>2.0.CO;2.

Lappen, C.-L., and C. Schumacher, 2012: Heating in the tropical atmosphere: what level of detail is critical for accurate MJO simulations in GCMs? *Climate Dynamics*, **39 (9)**, 2547–2568.

Lau, W. K.-M., and D. E. Waliser, 2011: *Intraseasonal variability in the atmosphere-ocean climate system*. Springer Science & Business Media.

Leary, C. A., and R. A. Houze, 1979a: Melting and evaporation of hydrometeors in precipitation from the anvil clouds of deep tropical convection. *Journal of the Atmospheric Sciences*, **36 (4)**, 669–679.

Leary, C. A., and R. A. Houze, 1979b: The structure and evolution of convection in a tropical cloud cluster. *Journal of the Atmospheric Sciences*, **36 (3)**, 437–457.

Li, C., X. Jia, J. Ling, W. Zhou, and C. Zhang, 2009: Sensitivity of MJO simulations to diabatic heating profiles. *Climate Dynamics*, **32 (2)**, 167–187.

Li, T., C. Zhao, P.-c. Hsu, and T. Nasuno, 2015: Mjo initiation processes over the tropical Indian Ocean during DYNAMO/CINDY2011. *Journal of Climate*, **28 (6)**, 2121–2135.

Lin, J., B. Mapes, M. Zhang, and M. Newman, 2004: Stratiform precipitation, vertical heating profiles, and the Madden-Julian Oscillation. *Journal of the Atmospheric Sciences*, **61 (3)**, 296–309.

Ling, J., and C. Zhang, 2011: Structural evolution in heating profiles of the MJO in global

reanalyses and TRMM retrievals. *Journal of Climate*, **24 (3)**, 825–842, doi:10.1175/2010JCLI3826.1.

Lintner, B. R., C. E. Holloway, and J. D. Neelin, 2011: Column water vapor statistics and their relationship to deep convection, vertical and horizontal circulation, and moisture structure at Nauru. *Journal of Climate*, **24 (20)**, 5454–5466.

Liu, C., and M. W. Moncrieff, 2004: Effects of convectively generated gravity waves and rotation on the organization of convection. *Journal of the Atmospheric Sciences*, **61 (17)**, 2218–2227.

López, R. E., 1977: The lognormal distribution and cumulus cloud populations. *Monthly Weather Review*, **105 (7)**, 865–872.

Lucas, C., E. J. Zipser, and B. S. Ferrier, 2000: Sensitivity of tropical west Pacific oceanic squall lines to tropospheric wind and moisture profiles. *Journal of the Atmospheric Sciences*, **57 (15)**, 2351–2373.

Madden, R. A., and P. R. Julian, 1971: Detection of a 40–50 day oscillation in the zonal wind in the tropical Pacific. *Journal of the Atmospheric Sciences*, **28 (5)**, 702–708.

Maddox, R. A., 1983: Large-scale meteorological conditions associated with midlatitude, mesoscale convective complexes. *Monthly Weather Review*, **111 (7)**, 1475–1493.

Mapes, B., and R. A. Houze, 1992: An integrated view of the 1987 Australian monsoon

and its mesoscale convective systems. i: Horizontal structure. *Quarterly Journal of the Royal Meteorological Society*, **118 (507)**, 927–963.

Mapes, B. E., 1993: Gregarious tropical convection. *Journal of the Atmospheric Sciences*, **50 (13)**, 2026–2037.

Mapes, B. E., 2000: Convective inhibition, subgrid-scale triggering energy, and stratiform instability in a toy tropical wave model. *Journal of the Atmospheric Sciences*, **57 (10)**, 1515–1535.

Mapes, B. E., P. E. Ciesielski, and R. H. Johnson, 2003: Sampling errors in rawinsonde-array budgets. *Journal of the Atmospheric Sciences*, **60 (21)**, 2697–2714, doi:10.1175/1520-0469(2003)060<2697:SEIRB>2.0.CO;2.

Mapes, B. E., and R. A. Houze, 1995: Diabatic divergence profiles in western Pacific mesoscale convective systems. *Journal of the Atmospheric Sciences*, **52 (10)**, 1807–1828.

Masunaga, H., 2012: Short-term versus climatological relationship between precipitation and tropospheric humidity. *Journal of Climate*, **25 (22)**, 7983–7990.

Matthews, A. J., 2008: Primary and successive events in the Madden-Julian oscillation. *Quarterly Journal of the Royal Meteorological Society*, **134 (631)**, 439–453.

May, P. T., and T. P. Lane, 2009: A method for using weather radar data to test cloud resolving models. *Meteorological Applications*, **16 (3)**, 425–432.

Moncrieff, M. W., 1992: Organized convective systems: Archetypal dynamical models, mass and momentum flux theory, and parametrization. *Quarterly Journal of the Royal Meteorological Society*, **118 (507)**, 819–850.

Muller, C. J., and I. M. Held, 2012: Detailed investigation of the self-aggregation of convection in cloud-resolving simulations. *Journal of the Atmospheric Sciences*, **69 (8)**, 2551–2565, doi:10.1175/JAS-D-11-0257.1.

Myers, D. S., and D. E. Waliser, 2003: Three-dimensional water vapor and cloud variations associated with the Madden-Julian Oscillation during Northern Hemisphere winter. *Journal of Climate*, **16 (6)**, 929–950.

Nakazawa, T., 1988: Tropical super clusters within intraseasonal variations over the western Pacific. *Journal of the Meteorological Society of Japan*, **66 (6)**, 823–839.

Nasuno, T., T. Li, and K. Kikuchi, 2015: Moistening processes before the convective initiation of Madden-Julian Oscillation events during the CINDY2011/DYNAMO period. *Monthly Weather Review*, **143 (2)**, 622–643.

Neelin, J. D., O. Peters, and K. Hales, 2009: The transition to strong convection. *Journal of the Atmospheric Sciences*, **66 (8)**, 2367–2384.

Neelin, J. D., O. Peters, J. W.-B. Lin, K. Hales, and C. E. Holloway, 2008: Rethinking convective quasi-equilibrium: Observational constraints for stochastic convective schemes in climate models. *Philosophical Transactions of the Royal Society of London A: Mathematical, Physical and Engineering Sciences*, **366 (1875)**, 2579–2602.

Neelin, J. D., and J.-Y. Yu, 1994: Modes of tropical variability under convective adjustment and the Madden-Julian oscillation. part I: Analytical theory. *Journal of the Atmospheric Sciences*, **51 (13)**, 1876–1894.

Olson, W. S., C. D. Kummerow, Y. Hong, and W.-K. Tao, 1999: Atmospheric latent heating distributions in the tropics derived from satellite passive microwave radiometer measurements. *Journal of Applied Meteorology*, **38 (6)**, 633–664, doi:10.1175/1520-0450(1999)038<0633:ALHDIT>2.0.CO;2.

Olson, W. S., and Coauthors, 2006: Precipitation and latent heating distributions from satellite passive microwave radiometry. Part I: Improved method and uncertainties. *Journal of Applied Meteorology and Climatology*, **45 (5)**, 702–720, doi:10.1175/JAM2369.1.

Pandya, R. E., and D. R. Durran, 1996: The influence of convectively generated thermal forcing on the mesoscale circulation around squall lines. *Journal of Atmospheric Sciences*, **53**, 2924–2951.

Parker, M. D., and R. H. Johnson, 2000: Organizational modes of midlatitude mesoscale convective systems. *Monthly Weather Review*, **128 (10)**, 3413–3436.

Peters, O., and J. D. Neelin, 2006: Critical phenomena in atmospheric precipitation. *Nature Physics*, **2 (6)**, 393–396.

Peters, O., J. D. Neelin, and S. W. Nesbitt, 2009: Mesoscale convective systems and critical clusters. *Journal of the Atmospheric Sciences*, **66 (9)**, 2913–2924.

Petersen, W. A., and S. A. Rutledge, 2001: Regional variability in tropical convection: Observations from TRMM. *Journal of Climate*, **14 (17)**, 3566–3586.

Pierrehumbert, R. T., 2000: Lattice models of advection-diffusion. *Chaos: An Interdisciplinary Journal of Nonlinear Science*, **10 (1)**, 61–74.

Posselt, D., S. Van Den Heever, and G. Stephens, 2008: Trimodal cloudiness and tropical stable layers in simulations of radiative convective equilibrium. *Geophysical Research Letters*, **35 (8)**, L08 802.

Powell, S. W., and R. A. Houze, 2013: The cloud population and onset of the Madden-Julian Oscillation over the Indian Ocean during DYNAMO-AMIE. *Journal of Geophysical Research: Atmospheres*, **118 (21)**.

Powell, S. W., and R. A. Houze, 2015: Effect of dry large-scale vertical motions on initial MJO convective onset. *Journal of Geophysical Research: Atmospheres*, **120 (10)**, 4783–4805.

Qian, J.-H., 2008: Why precipitation is mostly concentrated over islands in the Maritime Continent. *Journal of the Atmospheric Sciences*, **65 (4)**, 1428–1441.

Ramanathan, V., R. D. CESS, E. F. Harrison, P. Minnis, B. R. Barkstrom, E. Ahmad, and D. Hartmann, 1989: Cloud-radiative forcing and climate: results from the earth radiation budget experiment. *Science*, **243 (4887)**, 57–63.

Randall, D., M. Khairoutdinov, A. Arakawa, and W. Grabowski, 2003: Breaking the cloud

parameterization deadlock. *Bulletin of the American Meteorological Society*, **84 (11)**, 1547.

Raymond, D., and A. Blyth, 1992: Extension of the stochastic mixing model to cumulonimbus clouds. *Journal of the Atmospheric Sciences*, **49 (21)**, 1968–1983.

Raymond, D. J., 2000: Thermodynamic control of tropical rainfall. *Quarterly Journal of the Royal Meteorological Society*, **126 (564)**, 889–898.

Raymond, D. J., and A. M. Blyth, 1986: A stochastic mixing model for nonprecipitating cumulus clouds. *Journal of the Atmospheric Sciences*, **43 (22)**, 2708–2718.

Raymond, D. J., S. L. Sessions, and Ž. Fuchs, 2007: A theory for the spinup of tropical depressions. *Quarterly Journal of the Royal Meteorological Society*, **133 (628)**, 1743–1754.

Raymond, D. J., S. L. Sessions, A. H. Sobel, and Ž. Fuchs, 2009: The mechanics of gross moist stability. *Journal of Advances in Modeling Earth Systems*, **1 (3)**.

Richter, I., and Coauthors, 2015: An overview of coupled GCM biases in the tropics. *Indo-Pacific Climate Variability and Predictability*, **7**, 213.

Rickenbach, T. M., and S. A. Rutledge, 1998: Convection in TOGA COARE: Horizontal scale, morphology, and rainfall production. *Journal of the Atmospheric Sciences*, **55 (17)**, 2715–2729.

Rienecker, M. M., and Coauthors, 2011: MERRA: NASA's modern-era retrospective analysis for research and applications. *Journal of Climate*, **24 (14)**, 3624–3648.

Romatschke, U., and R. A. Houze, 2010: Extreme summer convection in south america. *Journal of Climate*, **23 (14)**, 3761–3791.

Rossow, W. B., and A. A. Lacis, 1990: Global, seasonal cloud variations from satellite radiance measurements. part II. cloud properties and radiative effects. *Journal of Climate*, **3 (11)**, 1204–1253, doi:10.1175/1520-0442(1990)003<1204:GSCVFS>2.0.CO;2.

Roundy, P. E., and W. M. Frank, 2004: A climatology of waves in the equatorial region. *Journal of the Atmospheric Sciences*, **61 (17)**, 2105–2132.

Ruppert, J. H., and R. H. Johnson, 2015: Diurnally modulated cumulus moistening in the preonset stage of the Madden-Julian oscillation during DYNAMO. *Journal of the Atmospheric Sciences*, **72 (4)**, 1622–1647.

Sahany, S., J. D. Neelin, K. Hales, and R. B. Neale, 2012: Temperature-moisture dependence of the deep convective transition as a constraint on entrainment in climate models. *Journal of the Atmospheric Sciences*, **69 (4)**, 1340–1358.

Sahany, S., J. D. Neelin, K. Hales, and R. B. Neale, 2014: Deep convective transition characteristics in the community climate system model and changes under global warming. *Journal of Climate*, **27 (24)**, 9214–9232.

Salby, M. L., and H. H. Hendon, 1994: Intraseasonal behavior of clouds, temperature, and motion in the tropics. *Journal of the Atmospheric Sciences*, **51 (15)**, 2207–2224.

Schiro, K. A., J. D. Neelin, D. K. Adams, and B. R. Lintner, 2016: Deep convection and column water vapor over tropical land vs. tropical ocean: A comparison between the amazon and the tropical western pacific. *Journal of the Atmospheric Sciences*, **73 (10)**, 4043–4063.

Schlesinger, R. E., 1994: Heat, moisture, and momentum budgets of isolated deep midlatitude and tropical convective clouds as diagnosed from three-dimensional model output. Part I: control experiments. *Journal of the Atmospheric Sciences*, **51 (24)**, 3649–3673, doi:10.1175/1520-0469(1994)051<3649:HMAMBO>2.0.CO;2.

Schreck III, C. J., J. Molinari, and K. I. Mohr, 2011: Attributing tropical cyclogenesis to equatorial waves in the western North Pacific. *Journal of the Atmospheric Sciences*, **68 (2)**, 195–209.

Schumacher, C., P. E. Ciesielski, and M. H. Zhang, 2008: Tropical cloud heating profiles: Analysis from KWAJEX. *Monthly Weather Review*, **136 (11)**, 4289–4300.

Schumacher, C., and R. A. Houze, 2003: The TRMM precipitation radar's view of shallow, isolated rain. *Journal of Applied Meteorology*, **42 (10)**, 1519–1524.

Schumacher, C., R. A. Houze, and I. Kraucunas, 2004: The tropical dynamical response to latent heating estimates derived from the TRMM precipitation radar. *Journal of the*

Atmospheric Sciences, **61 (12)**, 1341–1358, doi:10.1175/1520-0469(2004)061<1341:TTDRTL>2.0.CO;2.

Schumacher, C., M. H. Zhang, and P. E. Ciesielski, 2007: Heating structures of the trmm field campaigns. *Journal of the Atmospheric Sciences*, **64 (7)**, 2593–2610, doi:10.1175/JAS3938.1.

Seo, K.-H., and E.-J. Song, 2012: Initiation of boreal summer intraseasonal oscillation: Dynamic contribution by potential vorticity. *Monthly Weather Review*, **140 (6)**, 1748–1760.

Shige, S., Y. N. Takayabu, W.-K. Tao, and D. E. Johnson, 2004: Spectral retrieval of latent heating profiles from TRMM PR data. Part I: Development of a model-based algorithm. *Journal of Applied Meteorology*, **43 (8)**, 1095–1113, doi:10.1175/1520-0450(2004)043<1095:SROLHP>2.0.CO;2.

Shraiman, B. I., and E. D. Siggia, 1994: Lagrangian path integrals and fluctuations in random flow. *Physical Review E*, **49 (4)**, 2912.

Skyllingstad, E. D., and S. P. de Szoeke, 2015: Cloud-resolving large-eddy simulation of tropical convective development and surface fluxes. *Monthly Weather Review*, **143 (7)**, 2441–2458.

Smith, P. L., 1984: Equivalent radar reflectivity factors for snow and ice particles. *Journal of Climate and Applied Meteorology*, **23 (8)**, 1258–1260, doi:10.1175/1520-0450(1984)023<1258:ERRFFS>2.0.CO;2.

Smith, R. B., P. Schafer, D. J. Kirshbaum, and E. Regina, 2009: Orographic precipitation in the tropics: Experiments in Dominica. *Journal of the Atmospheric Sciences*, **66 (6)**, 1698–1716.

Smull, B. F., and R. A. Houze, 1987: Dual-doppler radar analysis of a midlatitude squall line with a trailing region of stratiform rain. *Journal of the Atmospheric Sciences*, **44 (15)**, 2128–2149.

Sobel, A., and E. Maloney, 2012: An idealized semi-empirical framework for modeling the Madden-Julian oscillation. *Journal of the Atmospheric Sciences*, **69 (5)**, 1691–1705.

Sobel, A., and E. Maloney, 2013: Moisture modes and the eastward propagation of the MJO. *Journal of the Atmospheric Sciences*, **70 (1)**, 187–192.

Sobel, A., S. Wang, and D. Kim, 2014: Moist static energy budget of the MJO during DYNAMO. *Journal of the Atmospheric Sciences*, **71 (11)**, 4276–4291.

Sobel, A. H., J. Nilsson, and L. M. Polvani, 2001: The weak temperature gradient approximation and balanced tropical moisture waves. *Journal of the Atmospheric Sciences*, **58 (23)**, 3650–3665.

Stachnik, J. P., C. Schumacher, and P. E. Ciesielski, 2013: Total heating characteristics of the ISCCP tropical and subtropical cloud regimes. *Journal of Climate*, **26 (18)**, 7097–7116.

Stachnik, J. P., D. E. Waliser, and A. J. Majda, 2015: Precursor environmental conditions

associated with the termination of Madden–Julian Oscillation events. *Journal of the Atmospheric Sciences*, **72 (5)**, 1908–1931.

Stechmann, S. N., and J. D. Neelin, 2011: A stochastic model for the transition to strong convection. *Journal of the Atmospheric Sciences*, **68 (12)**, 2955–2970.

Stechmann, S. N., and J. D. Neelin, 2014: First-passage-time prototypes for precipitation statistics. *Journal of the Atmospheric Sciences*, **71 (9)**, 3269–3291.

Steiner, M., R. A. Houze, and S. E. Yuter, 1995: Climatological characterization of three-dimensional storm structure from operational radar and rain gauge data. *Journal of Applied Meteorology*, **34 (9)**, 1978–2007.

Stoelinga, M. T., 1996: A potential vorticity-based study of the role of diabatic heating and friction in a numerically simulated baroclinic cyclone. *Monthly Weather Review*, **124 (5)**, 849–874, doi:10.1175/1520-0493(1996)124<0849:APVBSO>2.0.CO;2.

Suhas, E., and G. J. Zhang, 2014: Evaluation of trigger functions for convective parameterization schemes using observations. *Journal of Climate*, **27 (20)**, 7647–7666.

Takayabu, Y. N., K. Lau, and C. Sui, 1996: Observation of a quasi-2-day wave during TOGA COARE. *Monthly Weather Review*, **124 (9)**, 1892–1913.

Takemi, T., 2015: Relationship between cumulus activity and environmental moisture during the CINDY2011/DYNAMO field experiment as revealed from convection-resolving simulations. *Journal of the Meteorological Society of Japan*, **93 (0)**, 41–58.

Tan, J., C. Jakob, and T. P. Lane, 2013: On the identification of the large-scale properties of tropical convection using cloud regimes. *Journal of Climate*, **26 (17)**, 6618–6632.

Tao, W.-K., S. Lang, J. Simpson, and R. Adler, 1993a: Retrieval algorithms for estimating the vertical profiles of latent heat release. *Journal of the Meteorological Society of Japan. Ser. II*, **71 (6)**, 685–700.

Tao, W.-K., S. Lang, X. Zeng, S. Shige, and Y. Takayabu, 2010: Relating convective and stratiform rain to latent heating. *Journal of Climate*, **23 (7)**, 1874–1893, doi:10.1175/2009JCLI3278.1.

Tao, W.-K., and J. Simpson, 1989: Modeling study of a tropical squall-type convective line. *Journal of the Atmospheric Sciences*, **46 (2)**, 177–202, doi:10.1175/1520-0469(1989)046<0177:MSOATS>2.0.CO;2.

Tao, W. K., J. Simpson, C. H. Sui, B. Ferrier, S. Lang, J. Scala, M. D. Chou, and K. Pickering, 1993b: Heating, moisture, and water budgets of tropical and midlatitude squall lines: Comparisons and sensitivity to longwave radiation. *Journal of the Atmospheric Sciences*, **50 (5)**, 673–690, doi:10.1175/1520-0469(1993)050<0673:HMAWBO>2.0.CO;2.

Tao, W.-K., and Coauthors, 2006: Retrieval of latent heating from TRMM measurements. *Bulletin of the American Meteorological Society*, **87 (11)**, 1555–1572, doi:10.1175/BAMS-87-11-1555.

Thompson, G., P. R. Field, R. M. Rasmussen, and W. D. Hall, 2008: Explicit forecasts of winter precipitation using an improved bulk microphysics scheme. part II: Implementation of a new snow parameterization. *Monthly Weather Review*, **136 (12)**, 5095–5115, doi:10.1175/2008MWR2387.1.

Tian, B., E. J. Fetzer, B. H. Kahn, J. Teixeira, E. Manning, and T. Hearty, 2013: Evaluating CMIP5 models using AIRS tropospheric air temperature and specific humidity climatology. *Journal of Geophysical Research: Atmospheres*, **118 (1)**, 114–134.

Tompkins, A. M., 2001a: Organization of tropical convection in low vertical wind shears: The role of cold pools. *Journal of the Atmospheric Sciences*, **58 (13)**, 1650–1672.

Tompkins, A. M., 2001b: Organization of tropical convection in low vertical wind shears: The role of water vapor. *Journal of the Atmospheric Sciences*, **58 (6)**, 529–545.

Tseng, K.-C., C.-H. Sui, and T. Li, 2015: Moistening processes for Madden-Julian oscillations during DYNAMO/CINDY. *Journal of Climate*, **28 (8)**, 3041–3057.

Varble, A., and Coauthors, 2011: Evaluation of cloud-resolving model intercomparison simulations using TWP-ICE observations: Precipitation and cloud structure. *Journal of Geophysical Research: Atmospheres*, **116 (D12)**.

Varble, A., and Coauthors, 2014: Evaluation of cloud-resolving and limited area model intercomparison simulations using TWP-ICE observations: 2. Precipitation microphysics. *Journal of Geophysical Research: Atmospheres*, **119 (24)**.

Wang, L., K. Kodera, and W. Chen, 2012: Observed triggering of tropical convection by a cold surge: Implications for MJO initiation. *Quarterly Journal of the Royal Meteorological Society*, **138 (668)**, 1740–1750.

Wheeler, M., and G. N. Kiladis, 1999: Convectively coupled equatorial waves: Analysis of clouds and temperature in the wavenumber-frequency domain. *Journal of the Atmospheric Sciences*, **56 (3)**, 374–399.

Wheeler, M. C., and H. H. Hendon, 2004: An all-season real-time multivariate MJO index: Development of an index for monitoring and prediction. *Monthly Weather Review*, **132 (8)**, 1917–1932.

Williams, E., and Coauthors, 2002: Contrasting convective regimes over the amazon: implications for cloud electrification. *Journal of Geophysical Research*, **107 (D20)**, 50–1.

Wolding, B. O., and E. D. Maloney, 2015: Objective diagnostics and the Madden-Julian Oscillation. Part II: Application to moist static energy and moisture budgets. *Journal of Climate*, **28 (19)**, 7786–7808.

Wolding, B. O., E. D. Maloney, and M. Branson, 2016: Vertically resolved weak temperature gradient analysis of the Madden-Julian Oscillation in SP-CESM. *Journal of Advances in Modeling Earth Systems*.

Wolff, D. B., and B. L. Fisher, 2008: Comparisons of instantaneous TRMM ground validation and satellite rain-rate estimates at different spatial scales. *Journal of Applied Meteorology and Climatology*, **47 (8)**, 2215–2237.

Xu, W., and S. A. Rutledge, 2015: Morphology, intensity, and rainfall production of MJO convection: Observations from DYNAMO shipborne radar and TRMM. *Journal of the Atmospheric Sciences*, **72 (2)**, 623–640.

Xu, W., and E. J. Zipser, 2012: Properties of deep convection in tropical continental, monsoon, and oceanic rainfall regimes. *Geophysical Research Letters*, **39 (7)**, L07 802.

Yanai, M., S. Esbensen, and J. H. Chu, 1973: Determination of bulk properties of tropical cloud clusters from large-scale heat and moisture budgets. *Journal of the Atmospheric Sciences*, **30 (4)**, 611–627.

Yanai, M., and R. H. Johnson, 1993: Impacts of cumulus convection on thermodynamic fields. *The representation of cumulus convection in numerical models*, K. A. Emanuel, and D. J. Raymond, Eds., American Meteorological Society, Boston, MA, 39–62.

Yang, S., and E. A. Smith, 1999: Four-dimensional structure of monthly latent heating derived from SSM/I satellite measurements. *Journal of Climate*, **12 (4)**, 1016–1037, doi:10.1175/1520-0442(1999)012<1016:FDSOML>2.0.CO;2.

Yano, J.-I., and R. Plant, 2012: Convective quasi-equilibrium. *Reviews of Geophysics*, **50 (4)**.

Yasunaga, K., and B. Mapes, 2012a: Differences between more divergent and more rotational types of convectively coupled equatorial waves. part i: Space-time spectral analyses. *Journal of the Atmospheric Sciences*, **69 (1)**, 3–16.

Yasunaga, K., and B. Mapes, 2012b: Differences between more divergent and more rotational types of convectively coupled equatorial waves. Part II: Composite analysis based on space-time filtering. *Journal of the Atmospheric Sciences*, **69 (1)**, 17–34.

Yoneyama, K., C. Zhang, and C. N. Long, 2013: Tracking pulses of the Madden-Julian oscillation. *Bulletin of the American Meteorological Society*, **94 (12)**, 1871–1891.

Zhang, C., 2005: Madden-Julian oscillation. *Reviews of Geophysics*, **43 (2)**.

Zhang, C., and S. M. Hagos, 2009: Bi-modal structure and variability of large-scale diabatic heating in the tropics. *Journal of the Atmospheric Sciences*, **66 (12)**, 3621–3640, doi:10.1175/2009JAS3089.1.

Zhang, M. H., and J. L. Lin, 1997: Constrained variational analysis of sounding data based on column-integrated budgets of mass, heat, moisture, and momentum: Approach and application to ARM measurements. *Journal of the Atmospheric Sciences*, **54 (11)**, 1503–1524, doi:10.1175/1520-0469(1997)054<1503:CVAOSD>2.0.CO;2.

Zhang, M. H., J. L. Lin, R. T. Cederwall, J. J. Yio, and S. C. Xie, 2001: Objective analysis of ARM IO data: Method and sensitivity. *Monthly Weather Review*, **129 (2)**, 295–311, doi:10.1175/1520-0493(2001)129<0295:OAOAID>2.0.CO;2.

Zhao, C., T. Li, and T. Zhou, 2013: Precursor signals and processes associated with MJO initiation over the tropical Indian Ocean. *Journal of Climate*, **26 (1)**, 291–307.

Zipser, E., 1977: Mesoscale and convective-scale downdrafts as distinct components of squall-line structure. *Monthly Weather Review*, **105 (12)**, 1568–1589.